# EXPERIMENTAL STUDY OF SEISMIC SCATTERING BY A PENNY-SHAPED CRACK

by

James Francis Scheimer

B.S., Stanford University (1973)

M.S., Stanford University (1973)

SUBMITTED IN PARTIAL FULFILLMENT

OF THE REQUIREMENTS FOR THE

DEGREE OF DOCTOR OF PHILOSOPHY

at the



August, 1978

(i.e. February 1979)

Signature of Author.....

Department of Earth and Planetary Sciences

August, 1978

Certified by.....

Thesis Supervisor

Accepted by.....

Chairman, Departmental Committee on Graduate Students

# EXPERIMENTAL STUDY OF SEISMIC SCATTERING BY A PENNY-SHAPED CRACK

by

James Francis Scheimer

Submitted to the Department of Earth and Planetary Sciences

on August 11, 1978 in partial fulfillment of the requirements

for the Degree of Doctor of Philosophy

## ABSTRACT

Ultrasonic model seismology was applied to a study of scattering of P-waves by a dry and a fluid-filled crack. Three experiments were conducted. The first provided background information on the model medium and served to develop experimental techniques. The data from the other two experiments were used to test the applicability of a number of seismic techniques to the determination of the crack's size, orientation, and location by studying the scattered signal.

The technique of wavefront reconstruction was used to analyse a data set consisting of first arrival times and amplitudes of the combined incident and scattered wavefields. The amplitude distribution of the reconstructed wavefronts at various depths in the model showed that the signal scattered by the dry crack resembles that radiated by the sudden opening of a tensile crack, though the sense of the motion is reversed.

Differential seismograms were made between signals recorded for the case of the empty crack and the case of the crack filled with water. Since it can be shown for the elastic parameters of the model studied that the model containing a water-filled crack is equivalent to the homogeneous solid, this technique isolated the signal due to the crack. These differential seismograms showed that the waveform of the scattered signal was indistinguishable from that of incident wave, but inverted. A kinematic model of scattering by a penny-shaped crack was developed based on elastic solutions for the opening and closing of a tensile crack, using the stress field of the incident P-wave as the loading function on the crack face. The tensile crack was replaced with a Haskell-type model, where the rise time of the displacement discontinuity was given by the rise-time of the first cycle of the incident wave, and the final displacement was derived in terms of the maximum amplitude of the incident wave. Using this model a scale factor relating the ratio of the amplitudes of the scattered and incident signals to

the size of the crack and the wavelength of the insonifying radiation was calculated to be:

$$\left|\frac{U^P(\omega)}{W_{z_1}(\omega)}\right| = 0.125 \frac{a}{R}\sqrt{\frac{a}{\lambda}}\ C$$

where the quantity on the left is the ratio of the amplitude of the scattered wave, $U^P(\omega)$, to that of the incident wave, $W_{z_1}(\omega)$, at the frequency $(\omega)$, a = 1.27 cm is the radius of the crack, $\lambda \doteq 0.5$ cm is the wavelength of the insonifying radiation, R is the distance to the observation point from the center of the crack, and C is the scale factor calculated from the observed data. We found that for our model the scale factor was 7.3. From this we estimate, for this model, the opening of the crack caused by the P waves propagating along the crack to be ~ 1.5 times the peak to peak displacement of the incident P waves.

We conclude that these techniques can be of value in inferring the parameters of cracks in the earth made by artificial hydraulic fracturing for geothermal and other purposes as well as those in volcanic areas made naturally by excess pressure in magma. Further, we conclude that the method would benefit from additional study. Specifically, different model geometries and crack size to wavelength ratios could be studied. We believe our success demonstrates that scattering problems which are intractable analytically or numerically can be profitably studied using model seismology. We believe our success in using model seismology demonstrates its viability as a research tool, and that the technique is worthy of serious reconsideration.

ACKNOWLEDGEMENTS

In the course of my long tenure as a graduate student at M.I.T. I feel I have been the recipient of more than my share of help, support, forbearance, and love. The number of people to whom I am indebted for making my stay here an experience that has completely changed my life, is almost endless. The list starts, not with a person, but with a place, New England, and Boston in particular, opened my eyes to a way of life and a intensity in day to day life that was completely new to me. After an initial period of acute discomfort, I found I could actually enjoy living in an Eastern City. I am indebted to pushy Haymarket vegetable sellers, potato-faced Guinness drinkers in the South End, dark, meanacing street-corner leaners in the North End, the derelicts of Central Square, crafts fairs in New Bedford, the White Mountains, even Quincy Market. But most of all I am indebted to my friends who have helped me in so many ways to come to the end of my long road in academe.

There wouldn't have been a thesis to write, or anything to write about without the gentle but insistent prodding of my advisor, Keiiti Aki. I wouldn't call our association stormy, nor would I be able to call it completely tranquil, but it was always challenging. I didn't realise how much help and good advice he gave me until I was forced to finish this work in his absence. No matter how much I had gnashed my teeth over things he asked me to do while he was here, it was nothing compared to the great gnashing of teeth that took place after he went on sabbatical to Japan. You never miss the water till the well of advice runs dry.

Of course, I would never have been able to continue my studies without some sort of financial support, the work reported in this thesis was funded by U.S.G.S. grant 14-08-0001-G-339, and D.O.E. contract EY-76-S-02-2534.

I wouldn't have had a place to do the writing of this thesis or to do much of the computation without the ample support of the entire Applied Seismology Group of Lincoln Laboratory. I extend my thanks to Mike Chinnery and Dick LaCoss for their personal support and the use of the Group's facilities. Tom Landers was a great help as co-advisor when I first arrived here, and since then as a friend and arch-foe on the Fussball table. Tom Fitch was gracious enough, or gullible enough, to critique this work for me, an unenviable task for which I thank him deeply. I could name every person in the group and cite a dozen reasons I feel I need to thank them. But, the main reason I need to thank each one , is for their friendship, and support, which is, to me, more valuable than any material possession.

During my second year at M.I.T., I had the opportunity to work with Dr. A. V. Nikolaev, who reciprocated our New England hospitality by inviting me to visit the Institute of Physics of the Earth in Moscow, and their field base in Garm. I learned a great deal about seismology and seismic scattering during my stay there, and as a result of studies with Dr. Nikolaev and one of his students, Peter Troitskii, received much of the inspiration that led to the work in this thesis. I thank Alyosha and Peter for all of their help and friendship, and for showing me that Russian vodka is stronger than I am.

Thank you Sara, for a healthy dose of humility, for railing at ridiculous idiocies, and for introducing me to Amos.

Ah, and the library, without the keen-eyed assistant librarian of Lindgren, would I ever have found the Sevens ? Thank you Shelley for lunch breaks that usually broke me.

And my fellow-travelers, I could never have survived M.I.T. without the help of my fellow graduate students. At Group 22, the late-night commiseration of Tony Shakal, Howard Patton, and Ken Anderson provided me with countenances equally as haggard as my own to inspire me. Bernard Chouet and Michel Bouchon learned to survive in the same office with me and often provided much needed assistance. Dave Johnston provided considerable help in the laboratory, measuring elastic properties of my plastic rocks, and considerable entertainment at the computer, trying to decipher his digitizer tapes. Bill Brace provided not only the laboratory space, but inspiration and enjoyable conversation about woodworking and running. Bill Ellsworth, before he abandoned us for Menlo Park, kept my science honest, nearly killed me cross-country skiing, and proved to me that one could successfully complete a thesis and remain sane. Randy Richardson reinforced this by surviving with style, too.

Then of course, there's the Hobby Shop, George Pishenin, Ray Blessing, Hockey, the MITRFC, the Cambridge Center for Adult Education, Beth and Russell Marena, Stuart Homer, Mark Grosenbaugh, in short, some of the people and things that have conspired to distract me from science, but filled my life with learning and enjoyment that served a satisfying counterpoint to geophysics. I learned of the things that could compete

with my work for my attention, and were neccessary to keep me sane while I did it.

Last, but most assuredly not least I must thank Lorraine Lee, dulcimers, and mountain music in general for themselves, and for bringing me together with Kathleen, who seems to have survived this thesis along with me, not doggedly, but with flair and loving support, and has inspired me to do things I might have once considered impossible.

TABLE OF CONTENTS

## TABLES

## FIGURES

# 1. INTRODUCTION

Hydrofracturing of rock has a variety of applications in both exploration geophysics and in the development and exploitation of energy resources. One well known application is the measurement of in-situ tectonic stress.(Zoback and others, 1977) Two additional applications of hydrofracturing that are of particular interest in an increasingly energy conscious world are the stimulation of oil and gas reservoirs, and the development of geothermal energy sources (Aamodt,1977). Accurately determining the size, location, and orientation of cracks produced in any of the above applications are problems that have yet to be adequately solved. In this thesis we will report on model experiments which illustrate how seismic methods might be applied to making these determinations.

Cracks produced by hydrofracturing are often modeled as poker chip shaped, or penny-shaped cracks. To apply seismic methods to determining the parameters of such cracks, we will need to develop a model for the interaction of elastic waves with penny-shaped cracks. This interaction has been formulated as a diffraction problem by a number of researchers. Diffraction occurs whenever a travelling wave encounters an obstacle or geometrical discontinuity. A crack is a very severe form of discontinuity and can give rise to both scattered P-waves and scattered S-waves of considerable amplitude. The usual treatment of the problem is to define boundary conditions at the crack (of stress and displacement) and find solutions to the wave equation that match these boundary conditions for the sum of the incident wave field and the

scattered wave field. The field observed at the surface is a superposition of the incident and scattered wave fields. Various approximations are needed in these solutions which limit their ranges of validity to the near-field or the far-field. In the first section of Chapter 2 we will review some of these near- and far- field solutions which have appeared in the literature.

Mathematical expressions which describe the forward diffraction problem for a number of cases are certainly useful, but, most of these formulations are in a form that makes physical interpretation difficult. What we really need is a good kinematic model that will allow us to invert our observations at the surface and infer the source, which in this problem is a secondary scattering source. Another way to think of this scattering problem is to consider the incident elastic wave as a source of dynamic loading on the crack. This allows us to separate the problem into two parts. The first part of the problem is to estimate the displacement discontinuity across the crack due to the incident wave. In the second section of Chapter 2 we will refer to work on dynamic crack propagation and fracture mechanics for information on how to do this. The second part of the problem is to calculate the wave-field in the far-field or the near-field for a source which is a discontinuity in displacement. This corresponds to the familiar and well-documented problem of kinematic modeling of an earthquake in source mechanism studies. The second section of Chapter 2 closes with the combination of the two parts of this formulation of the scattering problem into a simple model of scattering by re-radiation. If this model is a good representation of the real world it should offer a

simple, convenient technique to determine the parameters of the crack, namely, the size, location, and orientation.

Of course, having formulated a model we need to try it out on some data set to determine both its validity and its usefulness. The methodology employed in testing this model was originally developed by P. Troitskii and J. Scheimer during a joint U.S.A.-U.S.S.R. experiment to test the application of acoustical holography techniques to seismic array data. (Vinogradov, and others, 1976) Seismic holography is of use in the near-field and in other applications could provide increased resolution of lateral structure over ray tracing. The problem with implementing a technique such as holography is the lack of seismic records from a high density array. This lack, coupled with the prediliction of Soviet seismologists to using model seismology, led to a series of model experiments which were undertaken both at the Institute of Physics of the Earth, in Moscow, and at M.I.T.

The experiments consisted of trying to reconstruct the ultrasonic wavefield inside a block of epoxy just above an obstruction made of thin sheet aluminum. The experimental set-up and one of the reconstructions are shown in fig. 1.1 and fig. 1.2. These results were sufficiently gratifying, that the researchers involved in the original experiment decided to continue independent experiments at their respective institutes. The process of modeling in seismolgy is one of judicious simplification and idealisation. Rather than continue with very simple (actually overly simple) geometric models, we decided to examine an idealised form of an

actual earth structure that had immediate interest, but to continue using the techniques already developed.

During the course of both the earlier experiments and the work reported in this thesis, we learned a great deal about the inherent advantages and problems of using physical models. Very little has been published on the engineering difficulties involved in this work, so much of our initial laboratory work involved considerable trial and error. The final solutions may not be the final answers, but they represent the best compromises we could find. The third chapter of this thesis outlines the history, advantages, and problems of model seismology and reviews our solutions to some of the inherent problems.

In addition, since we used models constructed from a Soviet-made epoxy, we conducted a number of experiments to determine the elastic properties of the medium. The experiments which used traditional seismic methods are reported in the latter half of the third chapter. After the experiments were completed, the blocks of epoxy were "destructively tested". We machined some small samples from the larger blocks and measured values for Q, density, and other parameters using techniques developed in rock mechanics studies. Since these studies are not directly related to the seismic experiments, they are reported in the appendix rather than in Chapter 3. Two more series of experiments were conducted to collect the data for the penny-shaped crack problem. The methods employed to collect this data and the preliminary results are also reported in Chapter 3.

The analyses of the data, using both traditional seismic methods, and the techniques based on the mathematics developed in Chapter 2., are reviewed in Chapter 4. Two distinct data sets were collected in the experimental runs which followed the determination of the model properties. The first data set consisted of travel-times and amplitudes of just the first cycle of the signal recorded on the top of an epoxy block with a penny-shaped crack near its center and the source attached to the bottom. The measurements were make over a rectangular grid to model first arrival data from a dense seismic array. This data set was collected with the wave-front reconstruction technique in mind, and the first secton of Chapter 4 recounts the results of using this technique on these data.

In the final experiments, most of the measureable waveform was recorded for the case where the crack was dry and the case where it was filled with water. Three experimental runs were conducted. In the first and second runs, 80 to 120 microseconds of the signal was recorded at each observation point for both the dry and fluid-filled cases. These records were then digitised and examined in both the time and frequency domains to see what the salient differences were between the two cases. Referring to fig. 1.3, we can see how very much alike the records for the dry and wet cases are at each point. The differences were so slight that another experiment was devised to extract just the differences between the records.

The two prior experiments made clear to us that significant differences between the wet and dry cases occurred mainly in the first 10 microseconds of the signal. so, only the first 10 to 15 microseconds of the signal were recorded in the last experiment. Even so, this resulted in over 280 records which had to be digitised and analysed. As will be explained in Chapter 3, differenced records were derived from the wet and dry records to isolate the scattering effect of the crack. These differenced records comprise the final data set. The latter portion of Chapter 4 explains how this data set was used, along with the kinematic scattering model of Chapter 2, to infer some of the crack parameters.

In the final, and concluding chapter, we bring together the results and analyses to see what we have learned about applying seismic methods to determining parameters of penny-shaped cracks. Another major question, that of the viability of model seismology as an investigative tool, can be addressed immediately, however. The experiments mentioned above, provided data sets in the same form as field data which were exactly tailored to our needs and could not have been nearly as easily collected in the field. Some reasons for the recent disuse of model seismology are discussed in Chapter 2, but for now, we can say the laboratory technology has arrived at a point where model seismology is once again a useful and valuable tool.

CAPTIONS FOR CHAPTER I

1.1. This figure shows the geometry of the original experiment. The block of epoxy is shown with measurements in wavelengths of the insonifying radiation. This experiment used a continuous source and a highly idealised geometrical model with a very high velocity contrast. The aluminum cross had a velocity twice the velocity of the block.

1.2. The data from the continuous experiment were used to reconstruct the wavefront 1 wavelength above the cross. This figure shows the intensity (squared amplitude) of the reconstructed wavefront. The position of the cross is superimposed by the shading. This figure and fig. 2.1 are reproduced from Nikolaev and others (1975)

1.3. This figure shows the first 80 microseconds of records at a number of points for both cases of the crack dry, and the crack filled with water. It is apparent that any differences between the respective wet and dry records are very slight. For this reason, it was necessary to subtract the wet record from the dry record to extract just the differenced record. Differenced records will be discussed in Chapter 3.

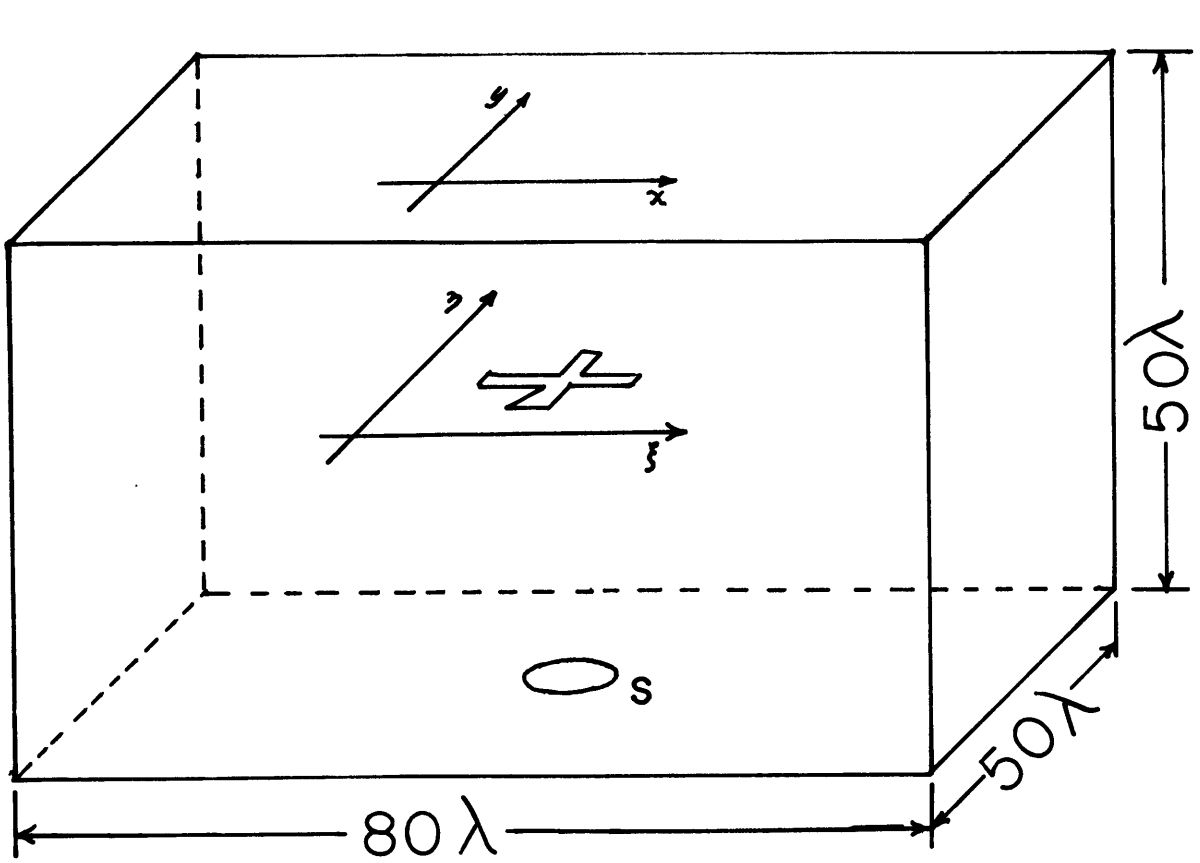


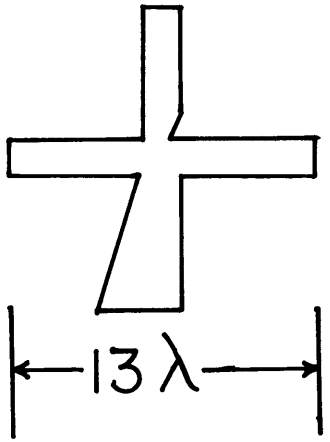


Figure 1.1

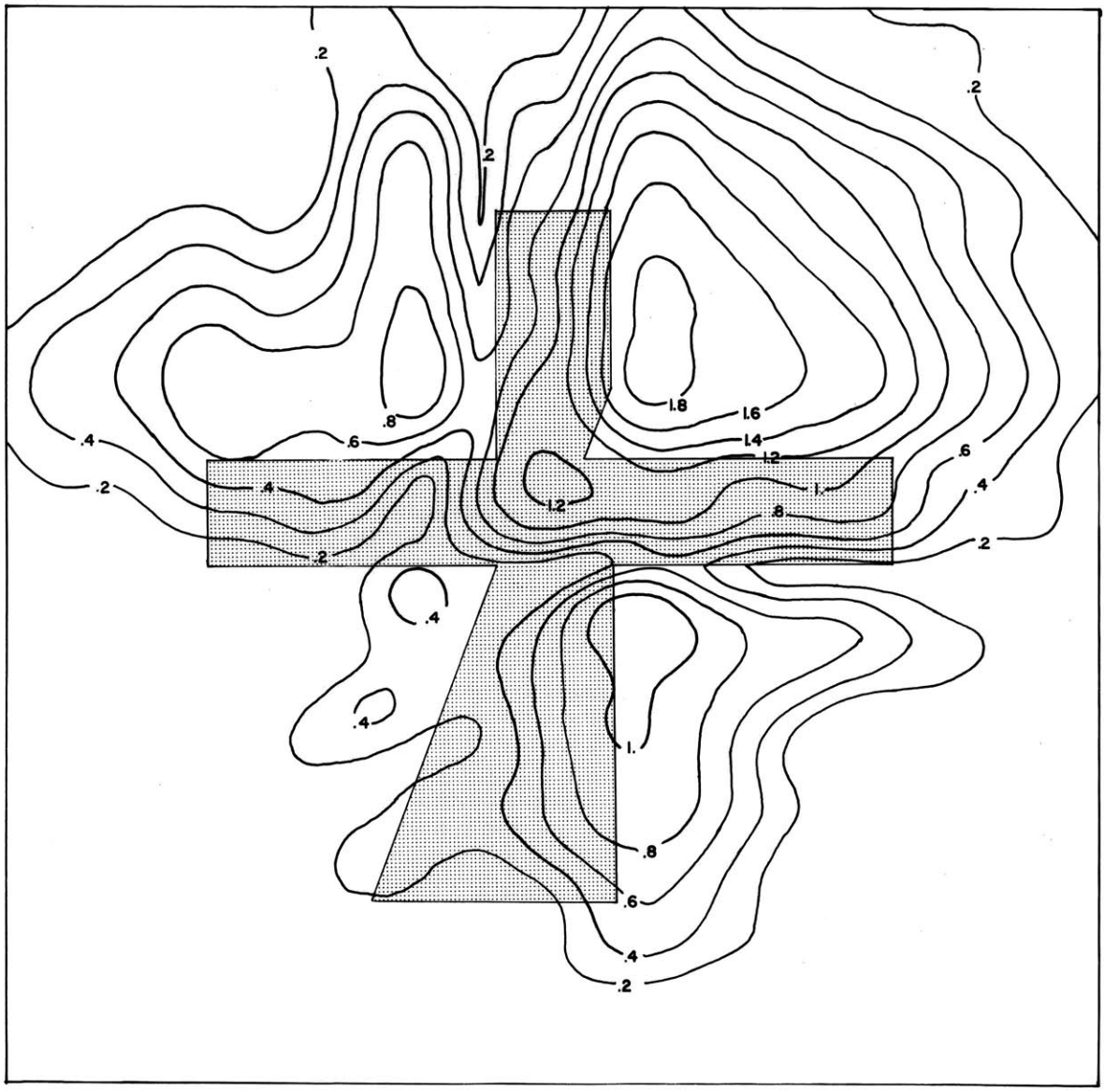


Figure 1.2

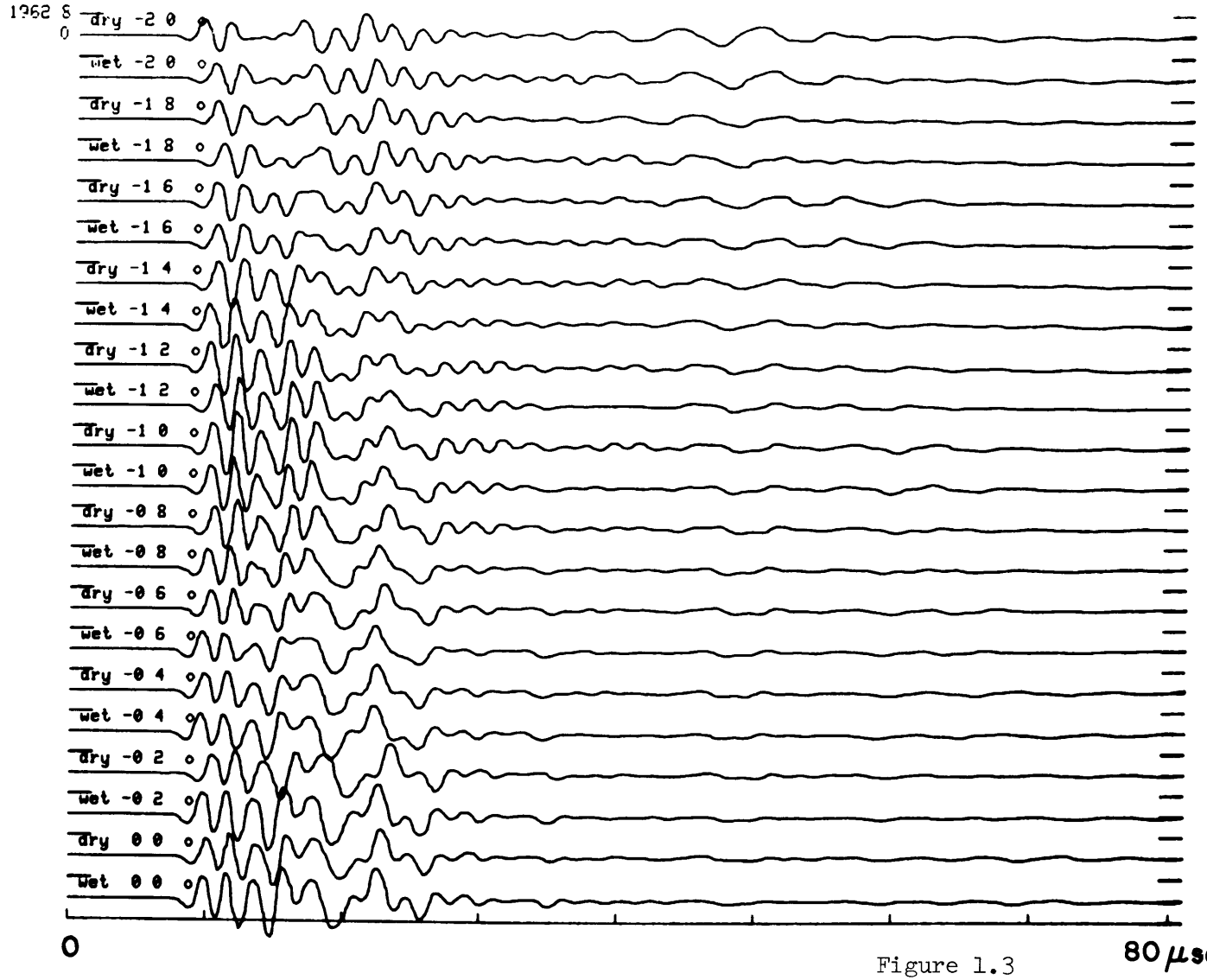
1962 8
0
dry -2 0
wet -2 0
dry -1 8
wet -1 8
dry -1 6
wet -1 6
dry -1 4
wet -1 4
dry -1 2
wet -1 2
dry -1 0
wet -1 0
dry -0 8
wet -0 8
dry -0 6
wet -0 6
dry -0 4
wet -0 4
dry -0 2
wet -0 2
dry 0 0
wet 0 0
0
80 μsec.

Figure 1.3

## 2. MATHEMATICAL BACKGROUND

This chapter establishes some of the mathematical background that will be needed to understand and interpret the results reported in later sections. In the first section we divide the discussion of scattering by a penny-shaped crack into a review of diffraction by cracks and the development of a kinematic model of scattering by re-radiation. The phenomenon of diffraction is well known in all fields involving wave propagation and has prompted considerable work. We will review only a small portion of this vast body of information which bears directly on our problem. The kinematic model of scattering by a penny-shaped crack is developed in terms of re-radiation of energy imparted to the crack by dynamic loading due to a plane wave impinging on the crack edge. Though re-radiation by a crack ,per se, is not a problem that has been widely treated in the literature, we can turn to studies of response of cracks to impact and to studies of seismic source mechanisms for background. As a corollary to this the representation of radiation produced by the opening of tensile cracks will be discussed. By combining some of these results, we present an equivalent-source model for scattering by re-radiation by a penny-shaped crack. These mathematical tools will aid in the interpretation of the experimental data and in formulating some simple kinematic models. In the second section we describe the technique of wavefront reconstruction which can be used, along with more traditional seismic methods, to examine the scattered wavefield from such cracks. The mathematics which explain this technique, while well-established in optics, are not widely used in

seismology and will require some development.

## 2.1. DIFFRACTION BY A PENNY-SHAPED CRACK

Work done on diffraction of elastic waves by two- and three-dimensional cracks of various configurations can be divided into far-field and near-field studies. Among studies of far-field diffraction problems is the work of Ang and Knopoff (1964 a,b) who produced far-field solutions for wavelengths $\lambda >> (a)$, where (a) is the principal dimension of the diffractor. In addition, Sih (1968) studied the problem of stress waves of arbitrary wavelength ($\lambda$) impinging on three dimensional finite cracks. This work involved the solution of a pair of dual integral equations involving a function of normalised wavenumber ka, where a is half-dimension of the crack's principle dimension, and k is the wavenumber of the incident wave . Results from this work show that the deviation of the dynamical stress-intensity factor from the static-loading case is only on the order of 27.5% higher when crack dimension and $\lambda$ are nearly exactly equal. Otherwise, the difference between static and dynamic loading is not significant. Time-domain solutions for the same problem were developed using the Wiener-Hopf technique by Thau and Lu (1970,1971), but these solutions rapidly become intractable when multiple reflections are considered. Jain and Kanwal (1972) decomposed the incident wave field into P and S components and studied the diffraction of each of these components by a pair of coplanar Griffith cracks. By taking the limit as the distance between the inner edges of the cracks tended to zero, they were able to solve the problem of diffraction

by a single Griffith crack. Though the computational methods differed, these results agree with those derived by Mal (1973). In these studies, the far-field approximations which were made make the results inappropriate for near-field problems.

The near-field problem has been most recently treated by Fehler and Aki (1978). The success of a number of researchers in using numerical techniques (i.e. Burridge (1969), Madariaga (1976), Das and Aki (1977)), inspired Fehler and Aki to use the finite difference technique of Madariaga (1976) in the analysis of near-field diffraction. In this work, the crack is modelled as an infinite strip in a homgeneous elastic medium, occupying $|x| < a$ and $y=0$; the faces of the crack are assumed to be stress-free surfaces. The solution to the problem comes from solving two mixed boundary value problems relating the incident wave and the diffracted wave by the boundary conditions on the crack surfaces. For a fluid-filled crack it is shown that one of the boundary condition (for normal stress over the crack face) is given by:

$$\tau_{yy}^{diff}(x,0,t) = -\tau_{yy}^{inc}(x,0,t) + Cv^{diff}(x,0,t) \qquad \text{EQ 1}$$

for the region $|x| < a$. Where the quantity C is called the crack stiffness factor and is given by:

$$C = \frac{B}{\mu}\frac{2a}{d} \qquad \text{EQ 2}$$

where

d is the thickness of the crack ($d << \lambda$)

B is the bulk modulus of the liquid

$\mu$ is the rigidity of the solid

a is the radius of the crack

And where;

$t_{yy}$ is the normal stress

and, v is the displacement normal to the crack face.

As the dimensionless quantity C increases, the effect of the crack on the incident wave will decrease, Fehler and Aki report that for a crack stiffness factor of 10 there is no longer a shadow zone due to the crack with a negligible disturbance on particle motion. When the crack stiffness factor falls to 0 (which corresponds to an empty crack) the second term in the boundary condition vanishes, and the condition becomes exact for a free surface. These results will be used to estimate the effect of introducing fluid into our physical models .

## 2.2. KINEMATIC MODEL OF SCATTERING BY RE-RADIATION

Among the elastodynamic crack problems discussed by Sih (1968) is the class of problems concerned with the effect of time-dependent loading of a stationary crack. Sih reports that when the applied loads fluctuate periodically, the resulting stresses and displacements will propagate through the medium as waves. Citing the work of Maue (1954), Ang (1955), and Baker (1962) on the sudden appearance of a semi-infinite crack in a pre-stressed medium, Sih points out that the the mathematical formulation of these problems is equivalent to the specification of a uniform impact loading on

the crack surfaces. This loading can be described by stress wave with a Heaviside unit step function time dependence. Chen and Sih (1976) show, further, that the time dependence of the fluctuations in the stress intensity factor will have the same form as the time dependence of the incident wave. Thus, by the principle of superposition, we can postulate that the wavefield resulting from an elastic wave interacting with a crack will consist of a wave generated by the fluctuations of the crack faces superposed on the incident wave. The amplitude of the fluctuations of the crack faces, further, can be modeled by the same equations that describe the sudden opening of a crack in a stressed medium.

### 2.2.1. FORMULATION OF SOURCE MODEL

The opening of a tensile crack can be expressed in terms of a set of body forces consisting of the superpositon of an isotropic dilatation and a dipole source applied normal to the faces of the crack. (See fig. 2.1) Using the coordinate system shown in the figure, the components of the equivalent body force are given by:

$$f_1(x,t) = -\lambda\, \delta(x_2)\, \frac{\partial \Delta U(x_1,x_2,t)}{\partial x_1}$$

$$f_2(x,t) = -(\lambda + 2\mu)\, \delta(x_2)\, \frac{\partial \Delta U(x_1,x_3,t)}{\partial x_2}$$

$$f_3(x,t) = -\lambda\, \delta(x_2)\, \frac{\partial \Delta U(x_1,x_3,t)}{\partial x_3}$$

EQ 3

Where $\lambda$ and $\mu$ are the Lame's constants and U is the the slip or displacement. The seismic moment tensor for this source is:

$$M = S \begin{vmatrix} \lambda\bar{U} & 0 & 0 \\ 0 & (\lambda + 2\mu)\bar{U} & 0 \\ 0 & 0 & \lambda\bar{U} \end{vmatrix}$$

EQ 4

Where S is the area of a crack face and $\bar{U}$ is the slip averaged over the crack surface ( or fault plane ( $\Sigma$ )). The representation theorem can be used to derive the far-field SH, SV, and radial displacements ( $u^r, u^\phi, u^\theta$ ) from the slip function. ( Burridge and Knopoff, 1964) In the far-field the P-waves generated by the crack will contain only the radial component, and the SH and SV waves will be purely transverse. We will see in Chapter 3 that our records contain only P-waves, so we can limit our discussion to the radial component. The radial component of P-waves at a point x in an infinite homogeneous medium is given by:

$$U^P(x,t) = (4\pi\rho\alpha^3 R)^{-1}(c_{jkpq} n_j \gamma_k \gamma_p \gamma_q) \int_{\Sigma} \Delta\dot{u}(\xi, t - \frac{r}{\alpha}) d\Sigma_\xi$$

EQ 5

Where $\Delta\dot{u}(\xi,t)$ is the dislocation source velocity function, $\Sigma$ is the area over which the dislocation source acts, $\rho$ is the density, r is the distance from a point on the source to the observation point, $\gamma_i = \frac{x_i - \xi_i}{r}$, the direction cosines normal to $\Sigma$ are given by $\nu_i$, the direction cosines of the dislocation vector are $n_i$, and R is the distance from a fixed point of $\Sigma$ to the observation point.

The term involving the direction cosines and the elastic constants can be written in our case as:

$$\lambda + 2\mu \sin^2\theta \sin^2\phi$$

Where $\theta$ and $\phi$ are angles measured from the vertical ( $x_3$ ) axis and the axis parallel to the crack faces ( $x_1$ ), respectively. (See,

for example, Chouet, 1978) The integrand in eq.5 represents the displacement waveform for any time dependence or source geometry. For simplicity's sake we will model our source by a rectangular fault of length L and width W. The rupture begins on $\Sigma$ and $\xi = 0$ and propagates along L with a uniform velocity ($\alpha$). (cf. Haskell, 1964, Haskell, 1966, Haskell and Thomson (1972), and Thomson and Doherty, 1977) While more elegant and complex models are possible, the approximations necessary in the next section to derive the source parameters will obviate the need for a more sophisticated source geometry. The paramters which characterise waveforms generated by this model are the fault dimensions, the rupture velocity, the final displacement, and the rise time of the displacement function. In the next section we will see how we derive these parameters from a heuristic model of a P-wave loading a penny-shaped crack. At a given recording location we will record a superposition of this waveform and the incident signal. If we can separate the two signals, it will be possible to do the inverse problem and infer the source parameters of the scattering source from the scattered signal.

### 2.2.2. DETERMINATION OF DISPLACEMENT DISCONTINUITY

Some of the earliest work on opening of cracks under static loading was done by Sneddon (1944,1945). Sneddon examined the distribution of stress in the neighborhood of a circular ,or penny-shaped, crack in a homogeneous elastic solid under normal tension. The mathematical theory of elasticity which he employed gives a good representation of the components of stress in the

vicinity of the crack for all points not near the edge of the crack. The crack is assumed to be in the interior of an infinite elastic medium and is located within the circle defined by: $r^2 = x^2+y^2 = a^2$ in the plane z = 0. The boundary conditions on the plane z = 0, are :

$$t_{rz} = 0 \text{ for all values of } r,$$

$$\sigma_z = -p(r) \ (r<c), \ u_z = 0 \ (r>c),$$

where p(r) is the pressure applied to the crack faces as a function of r. Now, if we let $\rho = \frac{r}{a}$ , we get the normal component of displacement of the crack surface for ( $\rho < 1$):

$$|U_z|_{z=0} = \frac{4(1-\sigma^2)a}{\pi E} \int_{\rho}^{1} \frac{\mu d\mu}{\sqrt{\mu^2-\rho^2}} \int_{0}^{1} \frac{xp(x\mu a)}{\sqrt{1-x^2}} dx \qquad \text{EQ 6}$$

Where $\mu$ is the radial variable.

If p(r) is a constant over the crack face and we call this constant pressure (p), eq. 6 becomes:

$$|U_z|_{z=0} = \frac{(4(1-\sigma^2)a}{\pi E} \ a \sqrt{1-\rho^2} \ p \qquad \text{EQ 7}$$

This expression gives us an estimate of the displacement discontinuity due to static loading of the crack. We know from the work of Chen and Sih (1976) that the difference in crack response to dynamic and static loading is very slight, so we propose a quasi-static model wherein we will use the static response result of eq.7 to estimate the dynamic displacement. This approximation will limit the range of valid wavelength to crack size ratios. As

the wavelength of the incident wave becomes shorter and shorter compared to the crack size, the rise-time of the first arrival, and , therefore, the onset of loading, will become more and more impulsive. In the limit as the first arrival approaches a delta function, the loading will approach non-linear shock loading, which cannot be treated with classical elasticity. On the other hand, as the wavelength becomes longer and longer, the loading rapidly approaches the static case. Chen and Sih (1976) have done a number of numerical calculations which indicate that the dynamic stress intensity factor equals the static stress intensity factor when the normalised wavenumber (ka) is slightly less than 1, and will remain at or very near the static value for all ka > 1. From their results we can put a tentative lower bound on ka of .1. So, if the wavelength of the incident wave is of the order of the radius of the crack, we can use the static solution to estimate the discontinuity in displacement without incurring too much error.

To estimate the magnitude of the applied stress we need to evaluate the magnitude of the component of stress normal to the crack face due to an incident plane wave. In our experiment the k-vector of the incident P-wave is parallel to the faces of the crack. (See fig. 2.2a) The component of stress normal to the crack face is $t_{yy}$. Assuming that the incident wave can be locally described as a plane wave:

$$W(z_o) = W_o \exp\left[i\omega\left(t - \frac{z_o}{\alpha}\right)\right] e^{-\frac{\pi z_o}{Q\alpha T}}$$

EQ 8

The normal stress is given by:

$$t_{yy} = \lambda\Delta + 2\mu \frac{\partial v}{\partial y} \qquad \text{EQ 9}$$

Where $\lambda$ and $\mu$ are the Lame's constants. Since W is a plane wave, $\frac{\partial v}{\partial y}$ vanishes, giving:

$$t_{yy} = \lambda\Delta \qquad \text{EQ 10}$$

$\Delta$ is given by :

$$\Delta = \frac{\partial u}{\partial x} + \frac{\partial u}{\partial y} + \frac{\partial w}{\partial z} \qquad \text{EQ 11}$$

But only $\frac{\partial w}{\partial z}$ is non-zero, so we get:

$$t_{yy} \sim \lambda \frac{\omega}{\alpha} W_{z_o} \qquad \text{EQ 12}$$

Where $W_{z_o}$ is the amplitude of the incident wave at the depth $z_o$. This analysis gives only the functional dependence of the normal stress on the elastic paramaters and does not purport to give the exact value. However, replacing (p) in eq.4 with this expression for ($t_{yy}$), and rewriting $\lambda$ in terms of Poisson's ratio ($\sigma$) and Young's modulus (E), we get:

$$U \sim \frac{4}{\pi} a \sqrt{1-\rho^2}\, \frac{(1-\sigma^2)}{E} \frac{E\sigma}{(1+\sigma)(1-2\sigma)} \frac{\omega}{\alpha} W_{z_o}$$

or,

$$U \sim \frac{4}{\pi} a \sqrt{1-\rho^2}\, \frac{\sigma(1-\sigma^2)}{(1+\sigma)(1-2\sigma)} \frac{\omega}{\alpha} W_{z_o} \qquad \text{EQ 13}$$

This equation can be further simplified by noting that

$$\sqrt{1-\rho^2} \sim \sqrt{\frac{l_p}{a}}, \quad \text{and} \quad \frac{\omega}{\alpha} = \frac{2\pi}{l_p},$$

which gives:

$$U \sim \sqrt{\frac{a}{l_p}} \frac{\sigma(1-\sigma)}{1-2\sigma} W_{z_o}$$

EQ 14

where $l_p$ is the wavelength of P-waves. This expression, again, is not intended to give the exact value of the displacement discontinuity, but to indicate the functional dependence of the displacement discontinuity on the crack parameters and the incident wave parameters.

Before we can proceed with formulating the second part of the source model, calculating the wavefield produced by this displacment discontinuity, we need to finish defining the source parameters. What remains is to determine the area over which this displacement is applied. To do this we need to decide just how we expect the incident wave to interact with the crack. In order to simplify the problem we will consider only first arrivals from the crack. We postulate that the maximum amplitude of the first arrival will occur when the incident wave has traveled one-half wavelength into the crack. (For $l_p < a$ ) This is a reasonable assumption since at this point the crack surface will be experiencing its greatest deflection, since, as the wave propagates further into the crack region, we must sum up contributions from the negative portion of the cycle. This means that the segment of the crack that will actually be deflected will be defined by the projection of $\frac{l_p}{2}$ onto the crack surface. (See fig. 2.2b) The area of this segment is given by :

$$K = a^2 \cos^{-1} \frac{a-\frac{l_p}{2}}{a} - (a-\frac{l_p}{2}) \sqrt{2a\frac{l_p}{2}-(\frac{l_p}{2})^2}$$

EQ 15

From these derivations we can now define the parameters of the source model. The source dimensions are determined by the area K, we will let the length of the source L be $\frac{1}{2}p$. This means that the width W remains to be determined. The slip velocity function we can determine directly from the incident waveform. The final displacement we will take to be the quantity U given in eq. 13, and the rise time of the source is just the rise time of the first positive peak of the incident wave. Thus, the amplitude of the scattered signal will be proportional to the product of L x W x U x the displacement waveform x a constant of proportionality. Since we will know, for our model, the exact dimensions of the source, we can determine experimentally the value of the proportionality constant. With this constant in hand, we can determine the dimensions of other sources for similar geometries. In Chapter 4 we will use our experimental parameters to make the final formulation of this source model, and solve for the constant.

## 2.3. WAVEFRONT RECONSTRUCTION

Wavefront reconstruction , or downward continuation, is known under a number of different names and can be derived in many variant fashions. All of these derivations stem from the work of Huygens, Fresnel, and Kirchoff. These early researchers represented a wave in space as a summation of spherical wavelets radiating from every point on a prior wavefront. Most solutions of wave propagation problems which make use of Huygen's principle rely on the Fresnel-Kirchoff or Rayleigh-Sommerfeld diffraction integrals. Most of the work done in this area has involved calcu-

lating the diffraction pattern due to some obstacle in a wave's path ( as in the work cited in section 2.1). We are interested in formulating the inverse diffraction problem, that is, given the diffraction pattern of an object, we wish to recover an image of that object. We will recover this image by directly computing the wavefront amplitude and phase at a given depth from the amplitude and phase recorded at the surface. First we will present a straight-forward space-domain representation based on Huygen's principle and then will show the derivation of the angular spectrum representation and show that these formulations are essentially equivalent.

### 2.3.1. SPACE-DOMAIN WAVEFRONT RECONSTRUCTION

The forward problem consists of expressing the propagation of a complex wave-field defined in the (x,y) plane at a depth of $z_0$ to a new (x,y) plane at a depth of $z_1 > z_0 > 0$. We start with a monochromatic scalar wave-field in the half-space $z > 0$ :

$$c(x,y,z,t) = C(x,y,z)e^{-i\omega t} \qquad \text{EQ 16}$$

where it is assumed that $C(x,y,z)$ obeys the Helmholtz equation throughout the half space:

$$(\nabla^2 + k^2) = 0. \qquad \text{EQ 17}$$

$C(x,y,z,t)$ obeys the homogeneous wave equation and will simplify to a spherical wave at large distances from the source, falling to zero at infinity. This is just the Sommerfeld radiation condition. Ignoring the time dependence, we need to formulate an expression relating the wave field at a depth $z_0$

$C(x,y,z_0) = C_0(x,y,z)$ to the same wave field evaluated at another depth $z_1$ $C(x,y,z_1) = C_1(x,y,z)$ which is unconstrained to any set values of $z_1 - z_0$ . (See fig. 2.3)

Mathematically, the inverse problem of reconstruction can be solved by means of the following integral relation which is a form of the Rayleigh-Sommerfeld diffraction integral. (Sommerfeld (1954))

$$B(\xi,\eta) = i\frac{a_1}{\lambda}\iint A(x,y)T_z(x,y,\xi,\eta)dx\,dy \qquad \text{EQ 18}$$

where:

A(x,y)- are the measured values of the complex amplitude sampled on the x-y plane.

$T_z = \frac{1}{r_{12}}\exp\left|-ikr_{12}\right| \cos(n\hat{r}_{12})$ is the kernal of the integral.

n - is the normal to the x-y plane.

$\frac{a_1}{\lambda}$ is the ratio of the amplitude of the insonifying radiation to its wavelength.

The classical approach to the solution of this integral is to expand $r_{12}$ in a power series about z. The choice of terms retained in the series determines whether the solution is the Fraunhofer or Fresnel approximation. Since we are working with spatially band limited data, we will retain the explicit representation for $r_{12}$. Also, since the data are sampled at discrete points, we re-represent the integral in terms of summations.

$$B(\xi_k,\eta_l) = i\frac{a_1}{\lambda}\sum_j\sum_i A(x_i,y_j)\ T_z(x_i,y_j,\xi_k,\eta_l)\Delta x\ \Delta y \qquad \text{EQ 19}$$

We can make the following substitutions:

$$r_{12} = \sqrt{z^2 + (\xi_k - x_i)^2 + (\eta_l - y_i)^2}$$

$$k = \frac{2\pi}{\lambda}$$

$$\cos(n\hat{r}_{12}) = \frac{z}{\sqrt{z^2 + (\xi_k - x_i)^2 + (\eta_l - y_j)^2}}$$

And we can express the full complex amplitude as:

$$A(x_i,y_j) = a(x_i,y_j)\ \exp\left[i\alpha(x_i,y_j)\right]$$

Plugging these expressions into eq. 18 we get the full summation representation of the integral:

$$B(\xi_k,\eta_l) = i\frac{a_1}{\lambda}\sum_j\sum_i a(x_i,y_j)\ \frac{z}{z^2+(\xi_k-x_i)^2+(\eta_l-y_j)^2}$$
$$\exp\left[i\left[\alpha(x_i,y_j) - \frac{2\pi}{\lambda}\sqrt{z^2+(\xi_k-x_i)^2+(\eta_l-y_j)^2}\right]\right]\Delta x\ \Delta y \qquad \text{EQ 20}$$

We can separate eq.20 into real and imaginary parts. This will be somewhat simpler to implement on a computer.

$$\text{Real}(B) = -\sum_j\sum_i a(x_i,y_j)\frac{z}{r_{12}^2}\sin\left[\alpha(x_i,y_j) - kr_{12}\right]\Delta x\ \Delta y \qquad \text{EQ 21}$$

$$\text{Im}(B) = -\sum_j\sum_i a(x_i,y_y)\frac{z}{r_{12}^2}\cos\left[\alpha(x_i,y_y) - kr_{12}\right]\Delta x\ \Delta y \qquad \text{EQ 22}$$

Where we have removed the constant term $\frac{a_1}{\lambda}$ .

This is the brute-force form of wavefront reconstruction used in this thesis. The mathematical derivation is essentially the

same as that given by Vinogradov and others (1977), but the actual computer implementation has been slightly modified since that work. The major advantages of this form are its stability and the fact that the data can be irregularly sampled in space. The major disadvantage is the extreme slowness of the algorithm. Typical reconstructions of 50 x 50 arrays required 55 to 60 minutes on a PDP-11 computer. An alternative method might be used which takes advantage of the speed of the Fast Fourier transform algorithm. This technique is known as the angular-spectrum reconstruction technique.

### 2.3.2. ANGULAR SPECTRUM REPRESENTATION

The angular spectrum representation of a wavefield has been widely used in antenna theory (Bracewell,1965). The Fourier transform pair of aperture distribution and its angular spectrum is directly analogous to the the transform pair of a waveform and its spectrum. This analogy allows interpretation of the angular spectrum representation in terms of well-known signal processing theorems and provides considerable insight into the process of solving the inverse diffraction problem. The general formulation of the angular spectrum representation as a solution to the inverse diffraction problem was developed by Sherman(1967,1968,1969), Wolf and Shewell (1967) , Shewell and Wolf (1968), and Lalor (1968,a,b).

Following the derivation of Shewell and Wolf (1968), we can express the wave field in eq.14, U(x,y,z), as a superposition of plane waves :

$$U(x,y,z) = \int_{-\infty}^{\infty}\int A(\nu_x,\nu_y)\, e^{i(\nu_x x + \nu_y y + \gamma z)}\, d\nu_x d\nu_y$$

EQ 23

where:

$$\gamma = \sqrt{\frac{u_i^2}{c^2} - \nu_x^2 - \nu_y^2}$$

EQ 24

In the case:

$$\frac{u_i^2}{c^2} \geq \nu_x^2 + \nu_y^2 \quad \text{, the waves}$$

EQ 25

$$A(\nu_x,\nu_y)\, e^{i(\nu_x x + \nu_y y + \gamma z)}$$

will be homogeneous plane waves propagating in all directions within the region $-\frac{\pi}{2} \leq \theta \leq \frac{\pi}{2}$, where $\theta$ is the angle between the positive z-axis and the direction of propagation.

Alternatively, when

$$\frac{u_i^2}{c^2} < \nu_x^2 + \nu_y^2 \quad \text{, the waves:}$$

EQ 26

$$A(\nu_x,\nu_y)\, e^{i(\nu_x x + \nu_y y + \gamma z)}$$

will be inhomogenwous waves which propagate in all directions perpendicular to the z-axis and attenuate exponentially in the +z direction. We can express the field $U_i(x_i,y_i,z_i)$ in the x-y plane at any arbitrary depth $z_i > 0$ in terms of eq.22 as:

$$U_i(x_i,y_i,z_i) = \int_{-\infty}^{\infty}\int A(\nu_x,\nu_y) e^{i(\nu_x x_i + \nu_y y_i + \gamma z_i)}\, d\nu_x d\nu_y$$

EQ 27

This equation has the same form as a 2-dimensional Fourier

transform of the function $A(\gamma_x,\gamma_y)e^{i\gamma z_i}$. If we replace (i) with a dummy variable (j) and transform back, we will recover $A(\gamma_x,\gamma_y)$ which can then be substituted back into eq. 26 to give:

$$A(\gamma_x,\gamma_y) = e^{-i\gamma z_j} \left|\frac{1}{2\pi}\right|^2 \int_{-\infty}^{\infty} U_j(x_j,y_j)\, e^{-i(\gamma_x x_j + \gamma_y y_j)}\, dx_j dy_j$$

EQ 28

Substituting eq. 27 into eq. 26 gives the full integral representation relating the wavefield $U_j$ at any $z_j \geq 0$ with the same wavefield evaluated at any other depth $z_i \geq 0$ ( $U_i$):

$$U_i(x_i,y_i,z_i) =$$

$$\left|\frac{1}{2\pi}\right|^2 \int_{-\infty}^{\infty} e^{i(\gamma_x x_i+\gamma_y y_i+\gamma z_i)} \int_{-\infty}^{\infty} U_j(x_j,y_j) e^{-i(\gamma_x x_j+\gamma_y y_j+\gamma z_j)}\, dx_j dy_j d\gamma_z d\gamma_y$$

EQ 29

When $z_j \geq z_i \geq 0$ eq. 28 is the solution to the forward diffraction problem. In the case $0 \leq z_i \leq z_j$ eq. 28 corresponds to the inverse diffraction problem, or backward propagation problem. Evaluating this integral as written is a very difficult task, so we will make it a bit more tractable by interchanging the order of integration. This gives:

$$U_i(x_i,y_i,z_i) = \int_{-\infty}^{\infty} K_{ij}(x_i - x_j, y_i - y_j)\, U_j(x_j,y_j)\, dx_j dy_j$$

EQ 30

where;

$$K_{ij}(x_i - x_j, y_i - y_j) \equiv K_{ij}(x_i - x_j, y_i - y_j, z_i - z_j) =$$

$$\left|\frac{1}{2\pi}\right|^2 \int_{-\infty}^{\infty} e^{i(\gamma_x(x_i - x_j)+\gamma_y(y_i - y_j)+\gamma(z_i - z_j)}\, d\gamma_x d\gamma_y$$

EQ 31

$K_{ij}$ is the kernal of the linear transform relating the field $U_i$ at $z=z_i$ to the field $U_j$ at $z=z_j$. If we limit ourselves to discussion

of two planes, $z=z_0$ and $z=z_1$, then, $K_{10}$ is called the forward wave propagator, and $K_{01}$ is the inverse, or backward, wave propagator.

In the next section we will examine the form of these propagators and use the angular spectrum representation to gain some insights into the physical meaning of our wavefront reconstruction technique. But before we can do this we need to establish that the space-domain and angular spectrum reconstruction techniques are equivalent. The forward wave propagator can be rewritten in a simplified closed form by comparing eq. 30 with the Weyl integral. The Weyl integral expresses spherical waves as a superposition of plane waves:

$$\frac{e^{ikr}}{r} = \frac{i}{2\pi}\int_{-\infty}^{\infty}\int e^{i(\gamma_x(x_1-x_0)+\gamma_y(y_1-y_0)+\gamma|z_1-z_0|)}\, d\gamma_x d\gamma_y \qquad \text{EQ 32}$$

where;

$$r = \sqrt{(x_1-x_0)^2+(y_1-y_0)^2+(z_1-z_0)^2}$$

Comparing eqs. 31 and 32 shows that:

$$K_{10}(x_1-x_0, y_1-y_0) = \frac{1}{2\pi}\frac{\partial}{\partial z_0}\left|\frac{e^{ikr}}{r}\right| \qquad \text{EQ 33}$$

So, eq. 29 can be rewritten as:

$$U_1(x_1,y_1) = \frac{1}{2\pi}\int_{-\infty}^{\infty}\int U_0(x_0,y_0)\frac{\partial}{\partial z_0}\left|\frac{e^{ikr}}{r}\right| dx_0 dy_0 \qquad \text{EQ 34}$$

This is the Rayleigh diffraction formula of the first kind. It can be shown (Sommerfeld, 1954) that this is equivalent to the Rayleigh-Sommerfeld diffraction formula given in eq. 17. Since the space-domain reconstruction technique was derived directly from eq.

17, the space-domain and angular-spectrum reconstruction techniques can be seen to be two sides of the same coin.

### 2.3.3. PHYSICAL INTERPRETATION OF WAVEFRONT RECONSTRUCTION

Given a complex wavefield such as that in eq. 15, we can form a two-dimensional Fourier transform of V(x,y,z):

$$A(\nu_x,\nu_y,z) = \iint U(x,y,z)e^{i\phi(x,y,z)}e^{-2\pi i(\nu_x x+\nu_y y)}\,dxdy \qquad \text{EQ 35}$$

The back transform will be given by:

$$V(x,y,z) = \iint A(\nu_x,\nu_y,z)e^{2\pi i(\nu_x x+\nu_y y)}\,d\nu_x d\nu_y \qquad \text{EQ 36}$$

We can give a physical interpretation to the frequencies $\nu_x$ and $\nu_y$ by considering a unit plane wave in three dimensions:

$$B(x,y,z) = e^{ik(\alpha x+\beta y+\gamma z)} \qquad \text{EQ 37}$$

where $\alpha$, $\beta$, and $\gamma$ are the direction cosines of the wavenumber vector $k=\frac{2\pi}{\lambda}$. The direction cosines are related to one another by :

$$\gamma = \sqrt{1-\alpha^2-\beta^2}$$

and are related to the spatial frequency domain by:

$$\alpha = \lambda\nu_x \quad , \quad \beta = \lambda\nu_y \qquad \text{EQ 38}$$

Substituting for $\alpha$ and $\beta$ in eq. 36, we get:

$$B(x,y,z) = e^{ikz\sqrt{1-(\lambda\nu_x)^2-(\lambda\nu_y)^2}}\,e^{2\pi i(\nu_x x+\nu_y y)} \qquad \text{EQ 39}$$

Comparing this with the back transform in eq. 35, we can see the eq. 35 can be thought of as a superposition of plane waves over all azimuths, with complex amplitude given by:

$$A(\nu_x,\nu_y,z) = A_o(\nu_x,\nu_y,0)e^{ikz\sqrt{1-(\lambda\nu_x)^2-(\lambda\nu_y)^2}} \qquad \text{EQ 40}$$

We can see from the condition given in eq.36 that as the spatial frequencies get lower and lower, they correspond to plane waves more and more parallel to the z axis. Conversely, as the spatial frequency increases it approaches one cycle per wavelength $\lambda$, which corresponds to a wave propagating parallel to the surface. As the spatial frequencies increase beyond this point, $\gamma$ becomes imaginary, so the first exponential in eq. 38 becomes an attenuator with respect to z. This is the case defined by eq.25, which means these values of spatial frequency correspond to inhomogeneous waves. Except in the very near field, these waves will not be observed due to the strong z-dependent attentuation. These waves carry information about details smaller than a wavelength in size, which we can't resolve.

Going back now to eq.19 which expresses the space-domain inverse propagator, we find that this propagator has preforce limited the range of spatial frequencies to much less than those which would give rise to inhomogeneous waves. This becomes more apparant by referring back to fig 2.3, where we see that the range of angles of plane waves used in the reconstruction (as given by the angle between n and r ) is limited by the relative sizes of the observation and reconstruction grids and the distance between them. This accounts for the extreme stability of the method. It also shows that including terms corresponding to higher spatial frequencies would only bring information into the reconstruction from sources

outside the region of interest.

2.3.4. SOURCES OF ERROR

The three major sources of error in reconstructing wavefronts at depth are due to errors in phase measurement, errors in amplitude measurement, and sampling effects. Errors in phase measurement have been quantitatively examined by Goodman and Silvestri (1969) ,as reported by Boyer (1971). Given a function g(x) with a Fourier transform G(/),

$$G(/) = \int_{-\infty}^{\infty} g(x) e^{-2\pi i x/} dx$$

EQ 41

G(/) will have amplitude given by |G(/)| and phase $\phi(/)$. Since we measure the phase digitally , we defacto divide the range of phase angles from 0 to $2\pi$ into N cells each of width $\frac{2\pi}{N}$. Neglecting, for the moment, effects due to amplitude quantization, this results in a quantized phase function $\hat{\phi}(/)$, which takes on the values of the cells' midpoints. This phase function, rather than being a smooth curve ends up being a summation of rectangle functions. The width of each rectangle is determined by the number of phase points that we have put into the cell. So what we reconstruct is a superposition of sinc functions:

$$\hat{g}(x) = \sum_{m=-\infty}^{\infty} \mathrm{sinc}(m+\tfrac{1}{N}) g_m(x)$$

EQ 42

where m is the order of the reconstructed image and the $g_m$ are a set of coefficients determined from the quantization interval and the actual phase spectrum of the data. The spectrum phase-

quantized function $\hat{g}(x)$ consists of the primary image (from the m=0 term) summed with false images due to each of the higher order terms in (m). Each of these images is attenuated by the factor $\mathrm{sinc}(m\pm\frac{1}{N})$. Also, each of the images is displaced in the space domain due to a term in the quantized spectrum that goes as $e^{iNm}$. As m and N increase, the higher order terms are displaced further away from the primary image. Thus, the primary image is not displaced in space and is attenuated by a factor $\mathrm{sinc}(\frac{1}{N})$. The intensity of the false images goes as:

$$I_m \sim \frac{1}{m^2N^2} \qquad \text{EQ 43}$$

So, the accuracy with which we can quantize the phase will determine the number of out of focus false images which will interfere with our desired primary image.

To see what happens because of errors in amplitude measurement, we refer to eq. 19. If the measured amplitude $a(x_i,y_i)$ contains errors $\delta a$, each of these errors will be propagated back to the reconstruction plane with the same attenuation as the corresponding amplitude. This means that the total error in $B(\xi_k,\eta_l)$ will be in the same ratio as the mean measured amplitude $\hat{a}$ to the mean error $\delta\hat{a}$.

Errors due to sampling a continuous wavefield can be understood in light of the Whittaker-Shannon sampling thorem. This theorem states that a band-limited function can be exactly reconstructed if it is sampled at a rate greater than twice the highest frequency component. This reconstruction is done by constructing a

sinc function about each sample point:

$$f(x) = \sum_{j=-\infty}^{\infty} f(j\Delta x)\ \mathrm{sinc}\left(\frac{x}{\Delta x}-j\right) \qquad \text{EQ 44}$$

So, if the highest frequency component of f(x) is W, then eq. 35 holds true for $\Delta x < \frac{1}{2W}$. If, however, f(x) (or our wavefield a $(x_i, y_j)$) contains components of order n+mN, these will be propagated back like those of order n. So, aliased high frequency components will be propagated back like low frequency components and added to the the desired wavefield, degrading the image we obtain.

Closely allied to the problem of aliasing is the generation of Moire' patterns by superposing geometrical patterns. Superposing a rectangular sampling geometry on a circularly-symmetric pattern such as the measured phase will result in the generation of Moire' zone plates. These zones in the phase distribution can be approximated by a Fresnel zone plate. The zones in a Fresnel zone plate are generated at distances $\frac{nr^2}{2\Delta x}$ from the origin, where r is the radius of the first zone, $\Delta x$ is the sampling interval, and n = $\pm 1, \pm 2, \ldots$ . Each of these zone plates can produce a second image, since they appear to be phase distributions of weaker sources. To avoid interference of these images with the primary image, we must image objects smaller than half the distance between the primary pattern and the first higher order pattern (El Sum (1967)). Since the phase distribution is not binary, the secondary and higher order zone plates are produced at $45^o$, $22\frac{1}{2}^o, \ldots$ and their intensity decreases with increasing order (Van Rooy, 1971). All of these sources of error will be evaluated for our particular experiment in Chapter 4.

CAPTIONS FOR CHAPTER II

2.1. The source geometry and the equivalent body force representation is shown here for the opening of a tensile crack. The body waves produced by this source will be superposed on the incident wave recorded at the receiver.

2.2. (a) The applied stress $t_{yy}$ on the faces of the crack is produced by a plane wave incident along the x-axis.

2.2 (b) The area over which the stress is applied is assumed to be the area K. This is the source region for the first arrivals model.

2.3. The x-y plane is the surface of the model and is referred to as the observation plane. The reconstruction plane ($\xi$-$\eta$ plane) is at a depth (z) in the model. The normal to the observation plane is represented by the unit vector n. The vector connecting a point in the reconstruction plane and a point in the observation plane is $r_{12}$.

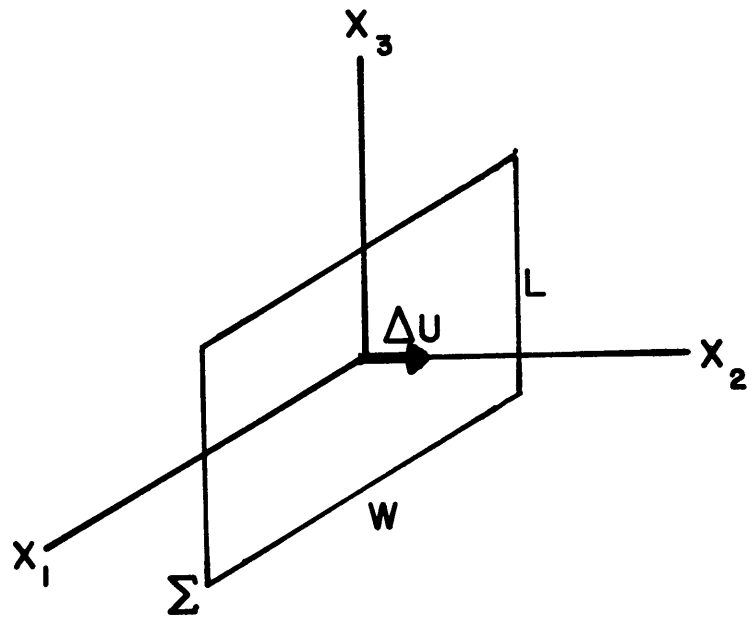


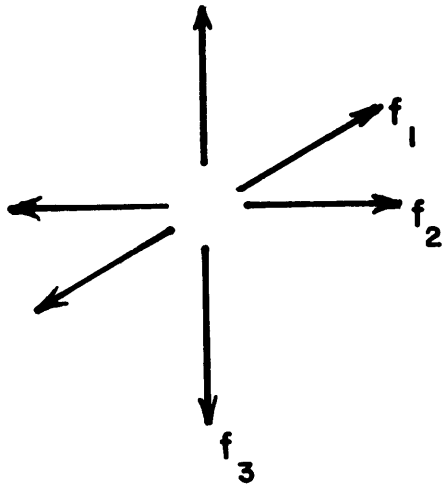


$f_1 \propto \lambda$

$f_3 \propto \lambda$

$f_2 \propto \lambda + 2\mu$

Figure 2.1

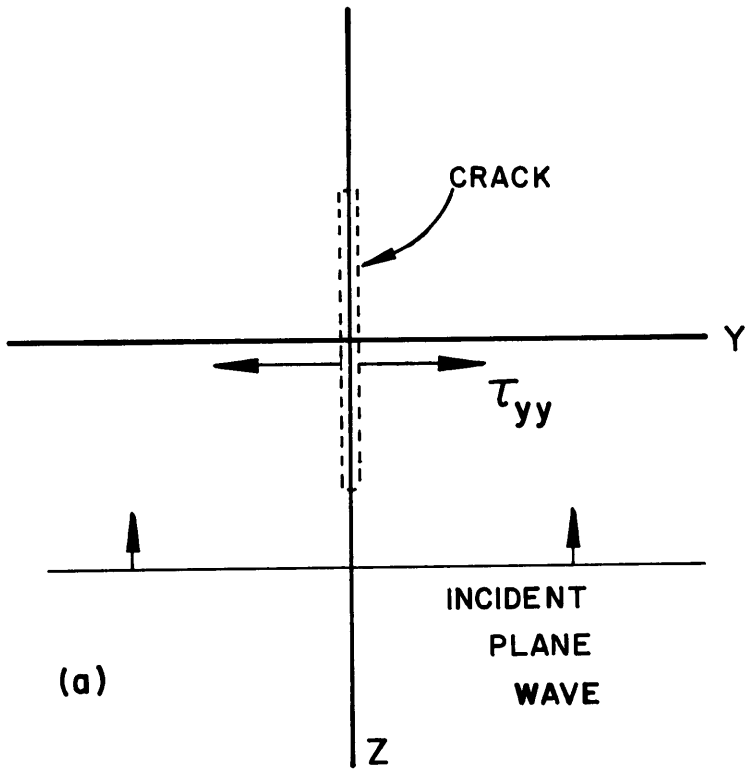


Figure 2.2

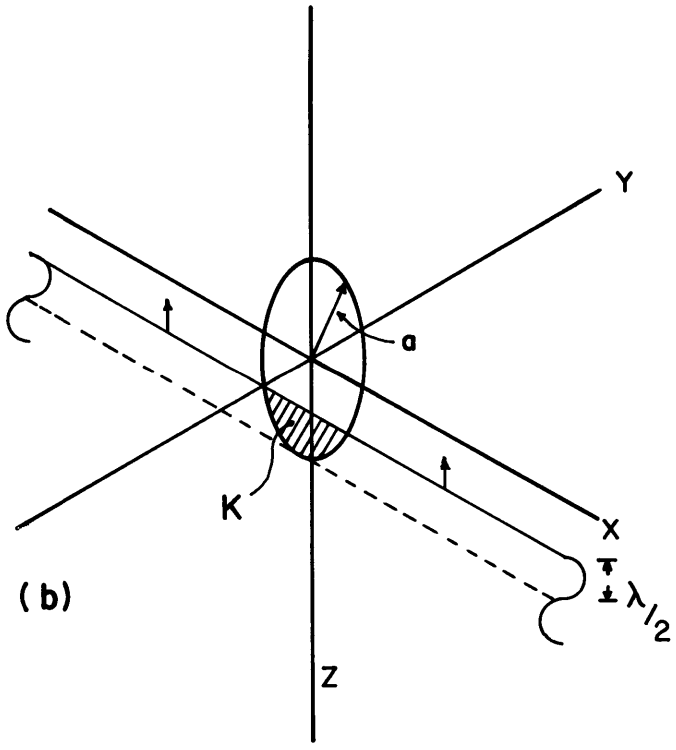


PLANE WAVE LOADING A PENNY-SHAPED CRACK

Figure 2.3

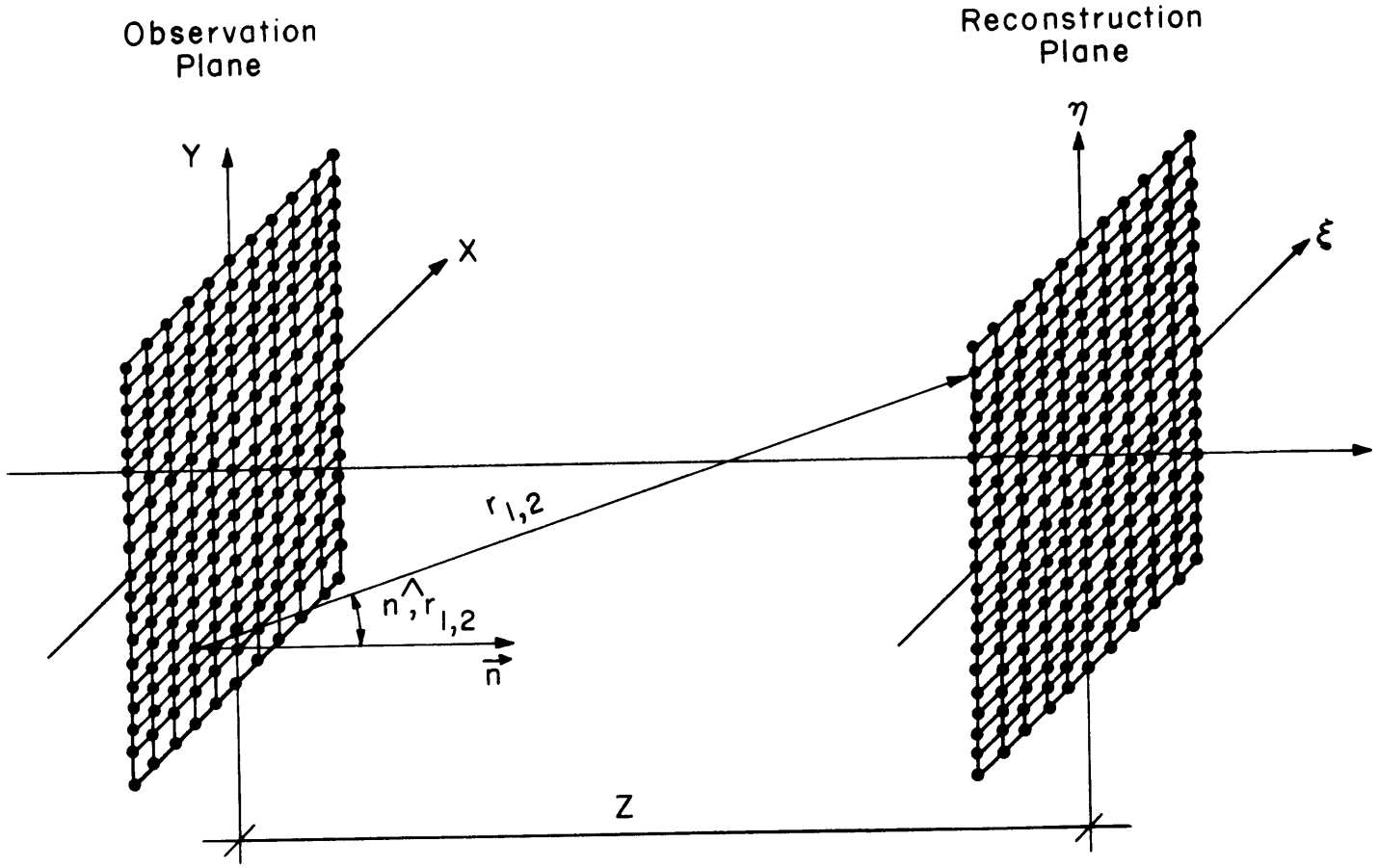
Observation Plane
Reconstruction Plane
Y
X
η
ξ
$r_{1,2}$
$\hat{n}, r_{1,2}$
$\vec{n}$
Z

# 3. THE EXPERIMENT

In order to test the effectiveness of the downward continuation technique and make use of this technique along with more traditional seismic methods to examine the energy re-radiated from a penny-shaped crack in the near-field it is necessary to obtain a useable data set. In using real-earth field data, we are hampered by the low spatial sampling density of most seismic data and the lack of precise fore-knowledge of the structure under study. As early as 1927 Terada and Tsuboi used laboratory models to overcome these diffculties in their studies of surface waves. From this time on a great number of researchers have resorted to model seismology in order to obtain data that was more tractable than real-earth data yet provided some insight into actual propagation effects. With such a long history of model seismology extant, it was not unreasonable to turn to small scale models in the evaluation of our problem.

This chapter begins with a discussion of the background and history of model seismology and some of the problems inherent in using models. The first (and most time-consuming) experimental task was to evaluate and refine model seismology techniques. The second section of the chapter begins with the description of the problems encountered in this task and the solutions we developed. The final section will discuss the actual experiments conducted on the penny-shaped crack problem.

## 3.1. MODEL SEISMOLOGY

### 3.1.1. HISTORY

The history of model seismology can be divided into two eras; work prior to 1951, and developments following 1951. As noted above, the first recognised work in the field was that done by Terada and Tsuboi(1927). The techniques and materials use in this work, and all work up until 1951, were rather different than those used today. Terada and Tsuboi used agar (a gel used in the cultivation of bacterial cultures) as their medium and excited a layered model with a continuous vibrational source. Their data consisted of photographs of surface standing waves. While this provided a good qualitative picture of surface waves, it did not provide any quantitative information that could be directly applied to the interpretation of conventional seismic records. Nonetheless, Terada and Tsuboi concluded that model seismology could be used to provide an intermediate step between the elegance and simplicity of mathematical models and the complexity of real earth data.

The next major work in model seismology was that of Rieber (1936,1937) who used a spark source to study wave propagation as applied to reflection sesmology. Again the data consisted of photographs but in this work a Schlieren technique was used to record the position and shape of wavefronts reflected and diffracted by screens of various shapes. As with the earlier work, little quantitative information was gleaned ,but the results gave great impetus to the development of frequency-wavenumber techniques in exploration seismology. At about the same time Schmidt (1939)

reported for the first time an experimental observation of head waves. This work made use of Schlieren techniques to record wavefronts in layered media.

All of these workers and their contemporaries made use of photographic techniqes. While they suceeded in providing striking visual representations of wave propagation phenomena, their results were not easily applied to the interpretation of seismic records. Obviously, some change in technique was required to make model seismology more directly applicable to the interpretation of seismic records.

The usefulness of model seismology took a great step forward at the beginning of the 1950's with the advent of readily available piezoelectric transducers. The year 1951 ,in particular appears as a watershed in the history of model seismology with the publication of work by Kaufman and Roever (1951) and Riznichenko and others (1951). In both of these cases the experimenters used transducer receivers coupled with oscilloscopes to record the surface motion of the models. Though some experiments have been undertaken since 1950 using photographic recording techniques and other forms of sources,by far the bulk of model seismic studies have used transducers both as sources and receivers.

Subsequent to 1951 a great number of researchers turned to model seismology to aid in the interpetation of real data. The number of yearly contributions in the field continued to climb through the 1960's until (according to O'Brien and Symes (1971)) a peak of over seventy papers were published in 1966. About this

time, however, seismologists outside of the Eastern European countries began to turn away from model seismology and concern themselves with more sophisticated processing of real earth data.

The decline of interest in model seismology could be traced to the increased capabilities of digital computers,the inherent limits of the model recording systems, and limitations in the complexity of possible models. Since model data consisted of oscilloscope traces , the model data did not lend itself to digital processing. These records could only be photographed, and due to the thickness of the traces, could not be digitized accurately. Further, the records became more and more complex as the models became less simplistic, until a point was reached where model seismograms rivaled real earth data in their complexity. With faster and more powerful computers allowing the processing of vast amounts of data, exploration seismologists, in particular, began to feel their time could more effectively be spent analysing field sections than data from idealised analog models. In Eastern Europe and the U.S.S.R., however, high technology digital equipment was not as readily available, with the result that, as Western contributions to model seismology have markedly declined since 1966, Soviet work has continued at a high level.

Only recently have new advances in recording technique renewed Western interest in model seismology. The availability of new interface electronics has generated a resurgence of interest in model seismology among exploration geophysicists. In particular, high speed analog to digital converters now make it possible to

obtain digital records of model seismograms. These records can be directly compared to real earth data and can be directly processed with existing programs. This allows a quick comparison of idealized models and real structure. Hilterman (1971,1974) has discussed a number of possible applications to exploration and within the last year a consortium of exploration companies has been formed to undertake extensive model studies at the University of Houston.

This new recording and processing capability finally allows models to be used in the way Tsuboi an Terada forsaw fifty years ago. It is now possible to construct simple analog models and obtain digitised records of surface motion that closely match the form of real field data. This allows one to test new processing techniques on idealised,known structures, and to compare these results with inferred real strutures. To make the results of model seismology experiments meaningful, however, one must carefully examine the shortcomings of models, and fully understand the assumptions and approximations made in modeling.

### 3.1.2. ASSUMPTIONS AND APPROXIMATIONS IN MODELING

The most obvious difference between model seismolgy and real earth seismolgy is the vast disparity in scales. If one were able to construct an exact scale model of some structure using real earth materials, the records obtained would be every bit as complex as field data. Obviously, if laboratory experiments are to provide additional insight into interpretation of seismic records, some approximations in complexity of models will have to be made. Furthermore, there would be great difficulties in using real earth

materials for models because of problems in bonding layers and in scaling physical properties. Thus, it is necessary to decide beforehand what simplifications to make in modeling the structure and to determine which parameters must be scaled accurately and which can be more or less ignored.

Parameters which must be carefully considered in elastic wave propagation models are largely dimensional. That is, the velocities of seismic waves and the ratio of the wavelengths of these waves to the linear dimensions of structures in the medium are parameters which must be scaled accurately. In addition, density, Poisson's ratio, bulk modulus, and Q should all be similar to these quantities in the earth. Other physical properties, such as microinhomogeneity, and stress amplitude are nearly impossible to model and are taken to be of relative unimportance. Table 3.1 summarizes the quantities considered in three-dimensional modeling and lists commonly used scale factors.

TABLE 3.1

SCALE FACTORS FOR 3-D MODELS

| QUANTITY | DIMENSIONS | SCALE FACTOR |
|---|---|---|
| Mass | M | $10^{-15}$ |
| Length | L | $10^{-5}$ |
| Time | T | $10^{-5}$ |
| Density | $M/L^3$ | 0.5 to 3 |
| Velocity | L/T | 1 |
| Elastic Modulus | $M/LT^2$ | 0.5 to 3 |
| Poisson's ratio | - | 1 |

| | | |
|---|---|---|
| Q | - | 0.2 to 100 |
| Wavelength | L | $10^{-5}$ |
| Frequency | 1/T | $10^{5}$ |
| Strain | - | not scaled |
| Stress | $M/LT^2$ | not scaled |
| Viscosity | M/LT | not scaled |

### 3.1.3. SOME PROBLEMS IN MODELING

The two most important problem areas encountered in model seismology have to do with interfaces and sources and receivers. The interface problem involves both bonding and material selection in its resolution. Current source and receiver problems center around the response of piezoelectric materials to both electrical and mechanical boundary conditions. These difficulties constitute the only non-standard problems in model seismology investigations . (All other problems that arise in model seismology are similar to those which arise in any seismic investigation.) In this section we will discuss some of the general considerations in the resolution of these problems and describe the specific remedies found in our own experimental work.

#### 3.1.3.1. INTERFACES AND BONDING

Many models are constructed of materials that pose severe bonding problems when multi-layer models are needed. Metals, such as aluminum,brass, or steel, are desirable for model studies since they are very low loss and are easily machined. A problem arises when two dissimilar materials , modeling different velocity layers,

must be fused together to model a welded interface. If we consider a bonded contact to be made up of three layers (see fig. 3.1) we can express the reflection and transmission coefficients as :

$$R = r_{12} + \frac{r_{12}t_{12}\exp\left|2iu\frac{h}{c_2}\right|}{1 - r_{12}r_{23}\exp\left|2iu\frac{h}{c_2}\right|} \qquad \text{EQ 1}$$

$$T = \frac{t_{12}t_{23}\exp\left|iu\frac{h}{c_2}\right|}{1 - r_{12}t_{23}\exp\left|2iu\frac{h}{c_2}\right|} \qquad \text{EQ 2}$$

for a normally incident harmonic wave.

O'Brien and Symes have calculated these values for a bond between brass and aluminum using Ardalite as the bonding agent (Ardalite is an adhesive commonly used in bonding metallic models.). Their results show that the bond (if perfect) will have to be less than .0025 times the wavelength of the incident wave in thickness to have a 1% or less effect on R and T. This would require a perfect bond less than 0.1 mm thick in most models. Another result, reported by Toksoz and Schwab (1964) used a steel and brass model bonded with epoxy. The assumption of perfect bonding gave errors of up to 20 % in Rayleigh wave phase velocity calculations as compared to experimental results for a bond 0.2 mm thick and waves with $\lambda$ = 2-3 cm. These and other model results have shown that the thickness of the bond,even assuming perfect bonding, is of paramount importance for waves propagating parallel to the interface, and of less importance for waves arriving normal to the interface.

The assumption of perfect bonding,however, is seldom justified. Schwab and Burridge (1968) used an epoxy resin bond 0.7 mm in thickness to join together two identical steel plates. The transmission and reflection coefficients for a wavelength to thickness ratio of 200-to-1 were measured to be 0.97 and 0.05, respectively. In addition, they examined the frequency dependence of the partition coefficients and found that it was necessary to model the bond as consisting of patches of perfect bonding interspersed with patches of total non-bonding.

The bonding problem can be solved only by using adhesives with acoustic impedances close to the impedance of the model material. O'Brien and Symes report that such adhesives will reduce the necessity of bond thinness by over $10^2$. That is, the bond can be as much as .1 times the wavelength in thickness and still produce less than a 1% error in the partition coefficients if the acoustic impedance of the adhesive is within 5 % of that of one of the model layers. Additionally, extreme care must be exercised in machining the interface surfaces and evenly distributing the adhesive. In our experimental work the model was cast out of epoxy in the first place, so that any subsequent bonding with epoxy adhesive would have the absolute minimum effect on wave transmission. Also, faces to be bonded were carefully machined to tolerances better than 0.1 mm and the epoxy adhesive was distributed as evenly as possible. The precautions were sufficiently successful that attempts to obtain reflection from the glued interface with nearly normal incidence proved fruitless.

3.1.3.2. SOURCE AND DETECTOR

As mentioned above, most work in model seismology since 1951 has been done using ultrasonic transducers as sources and receivers. Even with this long experience, very little theoretical work has been done on transducer source design. This means that the design and construction of the source and receiver will depend more on ingenuity and mechanical ability than any other part of the experiment. With this in mind, let us review the major requirements we have for model sources and receivers.

The source must be capable of being "fired" every few milliseconds since we obtain our record by stacking repetitive signals on an oscilliscope. Further, the source dimensions should be fairly small with respect to pulse wavelength so that it models a point source. The last requirement (and the bottom line in source construction) is that the source be able to produce pulses which are as short as possible and still produce enough radiation to be well above the noise level. The last two requirements tend to be mutually exclusive and require some judicious compromises. The receiver shares with the source the need to be of small physical dimensions (in order to sample a small area of the model). This is at odds with the other primary requirement,which is the need for high sensitivity. Also the receiver should be easy to position on the model and should give easily reproducible results. The final requirement for the receiver is that it have the minimum effect on the model when it is in use. With some design criteria established, let us now review some of the characteristics of transduc-

ers to see how we can best achieve these goals.

A number of single crystals , such as quartz and Rochelle salt, exhibit the phenomenon of piezoelectricity. That is, when strained, these crystals develop electrical charges on certain of their faces, and, conversely, when electrical potentials are applied to these faces, the crystal's dimensions will change. In addition to naturally occurring crystalline piezoelectric materials, two artificial piezo-ceramics are commonly available based on lead zirconate-titanate or barium titanate. The transducers used in our experiment were made from the former of these two piezo-ceramics (The commercial name for this ceramic is PZT4 or PZT5 depending on the Q of the material.). These transducers were discs cut from plates polarised in the direction of their thickness. This means that a voltage applied to the two parallel surfaces will correspond to a strain in the direction perpendicular to these surfaces.

The electromechanical response of such plates has been treated using equivalent electrical circuits by Mason (1948) Lavergne and Chauveau (1961), Redwood (1961,1962,1964), Belincourt and others (1964), and O'Brien and Symes (1971). These treatments can be used to predict some of the problems we can expect from our transducers and give some insight into their treatment. Fig. 3.2 shows a representation of a plate transducer in welded contact with two homogeneous media , and the lumped parameter equivalent circuit that is valid for frequencies below resonance as given by O'Brien and Symes (1971). The mechanical impedances of the materials are

given by $Z_i = \rho_i c_i LW$. Fig. 3.3 shows the response of such a system to a voltage impulse at time t=0. The plate will expand or contract depending on the polarity of the voltage, and will generate a uniform force with magnitude NV at each interface. This force will generate elastic waves into both media and back into the transducer itself. The wave transmitted into medium 1 will have an amplitude proportional to $-NVZ_1/(Z_0 + Z_1)$ and the wave transmitted into medium 2 will have an amplitude proportional to $-NVZ_2/(Z_0 + Z_2)$. Each interface will also generate a wave back into the transducer with amplitudes given by $NVZ_0/(Z_1 + Z_0)$ and $NVZ_0/(Z_0 + Z_2)$, respectively. The waves reflected back into the transducer will transmit a portion of their energy through the interface on each bounce, as shown in the figure, the end result being a decaying train of successive pulses.

Fig. 3.4a shows an experimental record that exhibits just such behavior. This record resulted when the the transducer was cemented to the sample but nothing was attached to the back of the transducer, making it a free surface with $r_2 = -1$. Obviously, such a source is of little use, since the train of source pulses will drown out any signal we are trying to study. The model, however, suggests that by welding a medium to the back of the transducer with acoustic impedance equal to that of the transducer ($Z_0 = Z_2$), making $r_2 = 0$, we can eliminate the internal reflections. Fig. 3.4b shows an experimental record which was obtained under the same conditions as 3.4a but the back of the source transducer in this case was cemented to a short column of epoxy. The epoxy column was loaded with powdered lead to bring its density near to that of the

transducer. This record shows that most of the internal reflections have been removed, giving us a source with a sufficiently short time function to be used in subsequent experiments.

When the plate is used as a detector, the impulse response is slightly different. Fig. 3.5 shows the open circuit voltage response of the equivalent circuit to an impulsive mechanical force applied at the interface with medium 1. If the receiver is unbacked $r_2 = -1$ and the impulse response will be a train of doublets decaying with time. In the case where $r_1$ is small, only the first doublet will be significant, and the receiver will act as an accelerometer. In the case where the receiver is backed such that $Z_2 = Z_0$, then $r_2 = 0$, and, the impulse response will become one half cycle of a square wave. If the period of this half cycle is small with respect to the period of the observed signals, the output voltage of the transducer will be directly proportional to the force of the incident signal, or the particle velocity. In the case of our experimental work, the receiver was backed in the same way as the source. The duration of the square wave pulse is given directly by the resonant frequency of the transducers, in our case all transducers have 1 MHz. resonant frequencies. Since the predominant energy in the recorded signal was .5 MHz or lower, our receivers acted as velocity recorders. The final form of the receivers and sources constructed for our experiment will be described in the next section.

## 3.2. EXPERIMENTAL APPARATUS

Since the source and receiver were the most intractable parts of the apparatus to fashion, we begin the description of the experimental set-up with these components. We have given ,in the preceding section, a list of the desired qualities of the source and receiver. We will now see what compromises were necessary in the actual construction of the source and receiver. As mentioned above, all of our transducers were compressional disks cut from PZT4 or PZT5 sheets. The transducers were chosen in three diameters : .125 inch, .25 inch, and .5 inch. The resonant frequency of all of the disks (determined by their thickness) was 1 MHz. The first problem confronted was getting sufficient pulse amplitude from the source so that the signal at the receiver would be above the noise level. While the smaller disks would have been preferable in terms of modeling a point source, it was found that only the .5 inch disks could provide sufficient signal levels.

The second problem to be solved was the problem of the source "ringing". The solution to this was suggested by the equivalent circuit models as described above. The difficulty here arises in affixing both the backing material and the connections for the electrodes to the back of the disk. Since it would be very difficult to fabricate a solid backing plate that would provide access clearance for the electode wires, it was decided to use loaded epoxy as described above. The amount of lead powder to include in the epoxy was arrived by at attempting to match the density of the hardened loaded epoxy to that of the transducers. A lucite tube

was machined to accept the transducer as shown in fig 3.6, and the epoxy mixture was poured into this tube. The problem with this fabrication scheme is the difficulty of guaranteeing repeatability. Local concentrations of the lead powder can greatly affect the reflectivity at the interface with the transducer. Though the sources constructed all provided very similar signals, there was some unavoidable variation from source to source. We attempted to alleviate this problem by using one source for all experiments, though five sources were constructed in all as possible back-ups.

Fig. 3.7 is a photograph of the source and receiver used throughout most of the experiment. The construction of the receiver posed many different problems than the construction of the source. It can be immediately seen that the source is significantly larger than the receiver. As with the source, we would prefer to use as small a transducer as possible. The rationale in this case,though, is that we want to sample the signal at a point rather than averaging over a large contact area. An attempt was made to use a commercially available probe called a pinducer which has a diameter of .8 mm. The signal levels with this probe were, unfortunately, of the same amplitude as the noise for all but the highest input voltages. We reluctantly abandoned this approach since high input voltages could quickly destroy our source transducers. Early attempts to use a larger transducer with a small probe attached to one face resulted in undesirable ringing in the probe-transducer system. The final solution was to affix a small drop of epoxy to one of the .125 inch transducers. The epoxy used was a fast-setting type which hardened in 7 to 10 minutes. By

dipping the receiver probe into this material shortly before it hardened, it was possible to form a droplet hanging from the transducer which hardened before it dropped off. The droplet, upon hardening, forms an almost perfect half-sphere. This half-sphere has an impedance close to that of the model and provides excellent coupling with the receiver transducer. As with the source construction technique, there is a great deal of difficulty in making identical receivers and we ,again, used only one receiver for all experiments, though three were constructed. Also, like the receiver, the support tube was bonded only around the edges of the transducer to minimize its interaction with the transducer, and the tube was filled with lead-loaded epoxy.

The next requirement is a method of attaching the source and receiver to the model. The source can be quickly and firmly attached to the model by using any of a host of heat-sensitive adhesives which polymerize on cooling. The source is then well coupled to the model, but can be removed with gentle heating. We would prefer, however, not to attach the receiver quite so permanently since we would like to record model seismograms at many points on the model. To do this we constructed a mechanical stage from commercially available components. The entire stage assembly is shown in fig. 3.8. The base of the stage is a screw-fed dovetail slide attached to a rigid aluminum plate. The slide can be positioned with an accuracy of $\pm$ .002 inch over a range of 4 inches along the x-axis. On top of this slide is attached another set of three orthogonal micrometer controlled slides. This upper stage can be moved in the x,y,or z directions with $\pm$.002 inch accuracy over a

range of 1 inch in each direction. This stage allows us to position the receiver above any point on the surface of the block within a 4 inch by 4 inch area, to an accuracy of $\pm$ .005 inch or better, which fulfills our requirement of easy positioning of the receiver. The requirement of minimal effect of the receiver on the model is met by isolating the model from the receiver support apparatus with layers of neoprene rubber. This requirement is further answered by the very small area of contact.

The last requirement for the receiver we must deal with is repeatability. We can overcome much of this problem by placing the receiver at one spot and making as many observations as possible before repositioning. To make meaningful comparisons between records from different spots on the surface, we need to ensure that the contact pressure between the model and receiver is a constant as possible. To this end, a spring support system was devised that allowed the receiver to be lowered onto the model with highly repeatable contact pressure. Cross-sectional and exploded views of this spring system are shown in fig. 3.9. In the experimental runs, the probe was positioned ~ 5 mm. (.25 inch) above the block using the vertical adjustment of the positioning stage. The probe was then lowered to contact the model surface by rotating the lever at the top of the mechanism. In an automated system this hand-operated lever could be replaced with a remote-controlled stepping-motor.

Having solved our mechanical problems, we now turn our attention to the electronics required to power our source,record the

waveforms, and measure travel times. A block diagram of the entire system is shown in fig. 3.10. All of the electronics consists of off-the-shelf commercial equipment with the exception of the time delay circuit. This circuit is a simple TTL time delay which has proven to be stable to within .05 microsecond. The most important piece of equipment, though, is the x-y scanner. This device is the interface between the oscilliscope and hard-copy. The trace on the oscilliscope screen is divided into 1024 points and then scanned. Each point is converted to a pair of voltages corresponding to the x-y position, and these voltages are applied to a servo-controlled x-y plotter which traces the curve onto a sheet of paper. These paper records can then be digitised with a manual digitiser. Theoretically the output of the x-y scanner could be directly digitised and recorded in digital format. The figure indicates where these components could be included in the recording system. Unfortunately, the expertise in digital electronics necessary to successfully implement this was unavailable to us.

The input to the source transducer was provided by a Velonix pulse generator which was capable of producing pulses up to 2 kV. The Velonix pulse generator was triggered by a Dumont pulse-generator which could provide very stable repetition rates on the order of milliseconds. The output of this generator was split to trigger both the Velonix generator and the sweep generator of the oscilloscope. Thus, the scope scanned every time a pulse was generated, and each pulse was stacked on top of the previous pulse. So each recorded waveform actually consisted of the average of many hundreds of pulses. Likewise, the timing circuit averaged the

travel times for 100 to 1000 pulses for each measurement. All of the equipment proved to be very stable and reliable through most of the experiment. In the latter stages of the experiment some instrumental drift began to set in, but this could be ameliorated by recording certain records at nearly the same time, as will be explained in the next section.

## 3.3. EXPERIMENTAL RESULTS

Once the problems of determining the optimum source and transducer configurations had been solved, and a recording and timing system had been developed, three model experiments were conducted. The models were constructed of a casting resin obtained in the Soviet Union and consisted of two blocks with nominal dimensions of 15 cm. x 15 cm. x 30 cm. The resin used in the models had much the same properties as a commercially available resin used in the United States (See Appendix), nonetheless, the first experiment was a determination of some of the acoustical properties of the casting resin. In the second experiment, the homogeneous block used in the first experiment was sawed in half and a penny-shaped crack was machined into the center and the block was re-cemented together. The second experiment consisted of examining the total wavefield produced by a P-wave vertically incident on this dry crack. The third experiment consisted of introducing a fluid (water) into the dry crack and recording the differences in signals recorded at the surface resulting from a vertically incident P-wave on both the wet crack and dry crack.

### 3.3.1. FIRST EXPERIMENT

In the first experiment, two sources were attached to the block. (see fig.3.11). The sources were attached on opposite sides to model a refraction geometry and a reflection geometry. The source on the top of the block was positioned .5 cm. outside of a 10.16 x 10.16 cm (4 in. x 4 in.) grid inscribed on the top of the block with a carborundum scriber. (See fig. 3.12) This grid provided a visual reference for positioning the recording probe, and allowed accurate positioning when re-occupying a recording location. The grid was marked out in rectangular coordinates with the origin of the grid located at the center of the block's top surface. Since the micrometers used in the positioning stage were calibrated in inches, the grid was scribed in inches. The x,y coordinates measured in inches were then converted to metric values, with the positive x direction taken to point toward the micrometer stage, this convention put the reflection source at point (x,y)=(-5.58,0.0) (measured in cm.). The transmission source was located on the opposite side of the block directly beneath the center of the reference grid. Typical records for the direct and reflection experiments are shown in figure 3.13.

Waveforms were recorded every 5 mm (.2 inches) in the x and y directions. Along the x axis, recordings were made every 2.5 mm (.1 inch). Time picks were made of the first arrival and two subsequent arrivals for the reflection experiment, Time picks for the direct experiment were only made for the first arrival. Plotting the arrivals as a function of position along the x-axis for the

reflection experiment and fitting a line through the points using a least-squares fit gives a velocity of 2.4 km. per second for the first arrival. (See fig. 3.14)

The second arrival velocity works out to be 1.03 km. per second. Looking at the record shows this arrival to be very high amplitude, the question was whether this arrival corresponded to an S-wave arrival or a Rayleigh wave arrival. Fortunately, the model used corresponded well to a physical representation of Lamb's Problem. The medium can be considered a homogeneous half-space with both source and receiver on the surface. Bullen (1965) shows that in the case of a free-surface on a homogeneous half-space when:

$$\left|2 - \frac{c^2}{\beta^2}\right|^2 = 4\left|1 - \frac{c^2}{\alpha^2}\right|^{\frac{1}{2}}\left|1 - \frac{c^2}{\beta^2}\right|^{\frac{1}{2}} \qquad \text{EQ 3}$$

then c will have a real root lying between 0 and $\beta$ . This real root corresponds to the velocity of the Rayleigh wave that is realisable in the medium (cf. Bullen eq. 5.1).

Thus, given a shear velocity ($\beta$) and a P velocity ($\alpha$) we can solve for possible Rayleigh wave velocities (c) and, alternatively, given the P velocity ($\alpha$) and the Rayleigh wave velocity (c), values of ($\beta$) which satisfy Eq. 3. correspond to realisable S-wave velocities.

Assuming first, that the observed second arrival is a shear wave we can easily solve for the Rayliegh wave velocity . If we let the left side of Eq. 3. be A and the right side be B we can plot values of A and B for a given ($\alpha$) as a function of (C). The

points where A = B correspond to roots of (C). Referring to fig. 3.15 we see that the value of (C) which falls between 0 and ($\beta$) is .97 km. per second. In this case, we can solve for Poisson's ratio:

$$\sigma = \frac{\lambda}{2(\lambda+\mu)} \qquad \text{EQ 4}$$

since;

$$\alpha = \sqrt{\frac{\lambda + 2\mu}{\rho}} \qquad \text{EQ 5}$$

and,

$$\beta = \sqrt{\frac{\mu}{\rho}} \qquad \text{EQ 6}$$

we get:

$$\sigma = \frac{1}{2}\,\frac{\left|\frac{\alpha^2}{\beta^2} - 2\right|}{\left|\frac{\alpha^2}{\beta^2} - 1\right|} \qquad \text{EQ 7}$$

which gives $\sigma$ = .400 for our block.

Alternatively, if the second arrival is assumed to be the Rayleigh wave, we are given (c) and ($\alpha$) , and we plot A and B as functions of ($\beta$) . The results of this calculation are shown in figure 3.16. For this case we get $\beta$ = 1.1 km per second. This gives a Poisson's ratio of .379. So, in either case, Poisson's ratio is slightly less than .4 . Furthermore, in either case, the Rayleigh and S-wave velocities are so similar that, within the dimensions of the models, we will never be able to get sufficiently far from the source to observe separate Rayleigh and S arrivals.

The transmission, or direct, experiment gives similar values for the P-velocity. Figure 3.17 shows the arrival times for the first arrival as a function of x, along the x-axis. If the thickness of the block is (Z) and the source is positioned exactly underneath the origin of the reference grid, then, the distance from the origin to the source will be just (Z). Then the direct-line distance from the source to a given receiver position (X,Y) will be given by :

$$S = \sqrt{X^2 + Y^2 + Z^2} \qquad \text{EQ 8}$$

so the travel-time for this path will be:

$$T = \frac{1}{V} S \qquad \text{EQ 9}$$

We have recorded the arrival times every 5 mm over the grid, which gives us a total of 441 observations. We can solve for the best $(\frac{1}{V})$ in a least-square sense. The resulting line is shown in fig. 3.18. This corresponds to a velocity of 2.38 km per second, which is in very good agreement with the value obtained from the reflection geometry.

These velocities indicate that, in the case of a direct experiment, the S-waves would arrive at (0,0) 50 - 60 microseconds after the first P. Also, referring back to fig 3.13 we can see that the period of the first arrival is about 2 microseconds. This period corresponds to a wavelength for the P-waves of about 5mm. Thus, the spatial sampling interval ($\Delta$) is about equal to the wavelength ($\lambda$) of the insonifying radiation.

Summarizing the results of the first experiment:

$\alpha \sim 2.4 \frac{km.}{sec.}$

$\beta \sim 1.0 \frac{km.}{sec.}$

$\sigma \sim .397$

$\lambda \sim 5$ mm.

3.3.2. SECOND EXPERIMENT

The second experiment required sawing the block into two pieces. This was done using a DoAll band saw. The rough surfaces left by the band saw were machined on a milling machine to an accuracy on the order of .01 mm. After this was done, a circular depression was machined into one half of the block. This depression was 2.54 cm in diameter with a depth of 1.5 mm. Two grooves were then machined into the surfaces to provide access for introducing fluids into the crack. The dimensions of the crack in terms of the wavelength determined in the first experiment were: diameter $\sim 5 \lambda$, thickness $\sim .3 \lambda$. (See fig. 3.19). The grooves for fluid transport had a width and depth on the order of $.25 \lambda$. These dimensions were a compromise between the need to provide adequate fluid flow and the desire to minimize diffraction by the fluid transport channels. To further reduce possible diffraction effects by the fluid transport channels, PVC tubing was epoxyed into each channel. The acoustic properties of PVC are almost identical to the epoxy used to make the model (See Appendix). If the epoxy joining the tube to the model fills any voids completely, only the

internal diameter of the tubing will give rise to diffraction. The internal diameter of the tubing was .5 mm which is much less than $\lambda$, indicating that diffraction effects due to this space should be slight. Alternatively, if the glue joint is spotty, there might be small voids between the tubing and the machined channel. The tubing is a tight press-fit in the channels, so these voids, if they exist should also be much smaller than $\lambda$ in size.

After the machining was completed, the block was glued together using an epoxy similar to the material used to originally cast the block. It was necessary to re-scribe the reference grid, since the block's dimensions were changed by loss of material in the sawing operation. This placed the crack center about .75 mm to the plus x side of the y-axis. The source was again attached directly beneath the origin of the reference grid. Between the first and second experiments, the first transmission source developed an internal short and was replaced. Thus, there is no guarantee that the source functions would be identical. This precluded direct comparison of waveforms recorded in the first experiment with those recorded in this experiment. Qualitatively,however, the waveforms are very similar and show the same major arrivals. Actual waveforms were recorded at 1 inch spacing (2.54cm) but arrival time and amplitude of the first positive peak were recorded every .2 inch (5mm).

Figure 3.20 shows the amplitude and arrival times of the first positive peak, recorded every 5 mm. There is a great deal of noise in the amplitude data, which is due to the presence of a viscous

oil applied to the surface of the block to enhance coupling between the model and receiver. The use of oils or greases to increase coupling is a common practice in model seismology. However, due to the fact that the receiver probe in our work had a spherical shape the coupling between the block and probe depended on the thickness of the oil film, this determined how high up the probe the grease coupled and ,thus, the amplitude of the signal. Nonetheless, a major feature is visible, there are two distinct peaks in amplitude centered around ($\pm$3.0,0.0). The travel time data, on the other hand, shows no discernable effect due to the presence of the crack.

The data recorded in this experiment were later used in conjunction with that recorded in the third experiment in order to locate the crack. All subsequent experiments were conducted without the use of any oils on the surface. In order to obtain sufficient signal levels in these runs, the input voltage to the source transducer was increased from 600v. to 1000v. The resulting records were, on the average, 1/2 the amplitude of the records in the first and second experiments, but still well above the noise level.

### 3.3.3. THIRD EXPERIMENT

The final experiment consisted of a number of runs to examine differences between waveforms recorded above the crack when it was dry and when it was filled with water. The waveforms for these runs were collected by recording the waveform with the crack dry, and without moving the probe, filling the crack with fluid and re-recording the waveform. By recording in this fashion, we are

assured of maintaining the same contact pressure, and, therefore, the same gain. Also, by recording both the wet and dry waveforms at nearly the same time, instrumental drift is reduced to a minimum.

The wet and dry records were almost identical but exhibited some slight differences. (See fig. 3.21) The source of these differences can be explained by referring to the work of Fehler and Aki (1978) described in chapter II. Plugging the elastic parameters of the block (See sec. 3.3.1 and Appendix) into eq. 2.2 we find that the crack stiffness factor for a water-filled crack is ~ 20. This means that the wet (or water-filled) crack will have minimal effect on the passage of the incident P-wave. We can, therefore, consider the wet records to be a good representation of the primary signal. On the other hand, the dry records contain a superposition of the primary signal and any signal due to the presence of the crack. This means we can recover the signal due just to the presence of the crack by subtracting the wet waveform from the dry waveform.

The records resulting from this differencing scheme were then filtered with a 3-pole butterworth lo-pass filter which had a high-frequency cutoff of 1 MHz. Since the cutoff of the analog recording system was 750 KHz, the filter cutoff was comfortably above the frequency range of the data. The wet waveform and the difference between the wet and dry waveforms at the origin are shown in fig. 3.22. It can be seen that the differenced record has the same form as the wet waveform, but is 180 degrees out of phase. Referring back to fig. 3.21 we can see that the scattered signal is

moved out in time with respect to the incident signal as we move away from the origin. Travel times for the first arrivals of the scattered signal are consistent with a signal originating at the depth of the crack. The scatter in the data is sufficiently bad that we can not localise the source to a particular portion of the crack. Fig. 3.23 shows the geometry which can give rise to such an arrival.

Armed with this piece of information we can return our attention to the result of the second experiment. That result showed a large amplitude peak around x= $\pm$3.0 cm. These two peaks could arise in the case where the differential in travel time between the direct waves from the source and the re-radiated waves from the crack is equal to 1/2 the period. This would make the first up-pulse of the re-radiated signal arrive in phase with the first up-pulse of the direct wave, resulting in a peak in the amplitude. According to the theoretical analysis of energy re-radiated by a dry crack, the peak energy should be re-radiated normal to the faces of the crack. Therefore, by just looking at the amplitude distribution of the first complete cycle at the surface, we can get a rough estimate of the depth and orientation of the crack. In the next chapter we will use the downward continuation techniques described in chapter 2 to reconstruct the complex amplitude at the depth of the crack using the results from both the second and third experiments. This will provide a check of both the rough estimate just described and the phenomenological model of re-radiation by a crack described in the second chapter.

FIGURE CAPTIONS FOR CHAPTER III

3.1. Eq. 3.1 and 3.2 express the transmission coefficient (T) and the reflection coefficient (R) for a plane wave ($e^{i\omega t}$) normally incident on a bonding layer of thickness (h), with a velocity in the layer of ($c_2$). The three sets of transmission and reflection coefficients for this geometry are designated by the arrows ($r_{ij}$) and ($t_{ij}$).

3.2. The transducers used in our experiment can be approximated by a piezoelectric plate welded between two different media. The acoustic impedances of the media ($Z_i$) are given by $Z_i = LW\rho c_i$. The approximate equivalent electrical circuit is shown for this system when the transducer is vibrating in thickness at a frequency below resonance.

3.3. This figure shows the approximate mechanical response of a piezoelectric plate to an impulsive voltage source as derived by Redwood (1963). (a) shows the amplitude of the waves transmitted and reflected at each interface. The waves reflected back into the transducer by medium 1 and medium 2 are designated P and Q, respectively. (b) shows the generation of multiple reflections. (c) shows the pulses generated by these reflections that will be transmitted into medium 1. The time delay between pulses is given by $\tau = \frac{T}{c_0}$.

3.4. (a) This experimental record shows the decay time of source ringing when the source is cemented to the model and the back of the transducer is a free surface. The signals we will be examining from the crack model are expected to arrive in the first 10-15

microseconds, which would be totally obscured by continuing radiation from the source. (b) Loading the back of the transducer with lead-impregnated epoxy reduces the ringing time to less than 5 microseconds, giving a much cleaner source time function that will not obscure scattered signals.

3.5. This is the exact electrical response of a flat-plate transducer to a mechanical impulse arriving from medium 1 , as derived by Redwood (1964). (a) shows the amplitudes of the transmitted waves. (b) shows the internal reflections of the stress pulse. (c) shows the voltage response of the transducer. Again, $t = \frac{T}{c_0}$. If $t$ is very short with respect to the period of the incident pulse, and the transducer is backed such that $r_2 = 0$, the receiver will have an output voltage proportional to the incident stress.

3.6. This figure shows a cross-sectional view of the source holder. The transducer is cemented to the backing tube only at the very edge to reduce interaction. The electrodes and connecting wires were coated with a thin insulating film so that the high triggering voltages would not short through the lead powder. Later dismantling of the sources showed that the lead-loaded epoxy had made essentially perfect contact across the entire back of the transducer.

3.7. The assembled source and receiver are shown in this photograph. We can easily see the round epoxy tip of the receiver probe which allows minimal contact area. The internal construction of the probe is essentially the same as that of the source. The probe is coated with a conductive silver paint which, when grounded,

provides electrical shielding. The shielding is necessary since the pulse generator (operating at a few kilohertz) acts as a radio transmitter and, since the signal from the probe is greatly amplified, any RF picked up will overwhelm the actual signal we are interested in.

3.8. This photograph shows the entire probe positioning assembly. The two stages provide accurate positioning in x and y. The vertical micrometer can be used to vary the contact pressure. The lever (a) operates a cam which lowers the probe to the surface of the model. The probe is raised when being moved from one location to the next in order to reduce wear on the probe tip and to avoid lateral stressing of the probe which could bend it.

3.9. Cross-sectional and exploded views of the probe-lowering mechanism. The lever and cam at the upper left end of the enclosure (6), can be used to displace plunger (5) up to .5 inch. When this plunger is fully depressed by the cam it does not contact the bottom of the hole in plunger (3), so that only the pressure of spring (4) displaces plunger (3). The receiver can be attached to this plunger using either the internal or external threads, providing the ability to test many different receiver configurations. This opposed spring system gives highly repeatable contact pressures. Measurements made by re-occupying a given x-y location many times showed variations of 5 % or less in measured amplitudes.

3.10. Block diagram of electronics used in the experiment. This system was developed for velocity measurements of earth-materials and was easily modified for model experiments. The digital recording system shown was not a part of our experimental apparatus, but is shown to indicate where such devices could be added.

3.11. This view shows the location of the sources used in the first experiment. The reflection and transmission sources were made as similar as possible, and both were mounted to the block using a heat-sensitive adhesive which polymerises on cooling giving a brittle but rigid bond. The second source on the bottom of the block was only used temporarily to compare source characteristics.

3.12. This photograph shows the reference grid scribed into the top of the model. The grid allows a quick visual check when resetting the probe location.

3.13. These records were both recorded at (2.54,0.0). The times $t_i$ shown on the reflection record were measured directly in the laboratory by matching a delayed timing pulse to the break of each arrival. The peak (A) in the direct record is the first positive peak which was used for the arrival time and amplitude measurements discussed in the text. Arrival times for the direct records were measured by aligning the delayed timing pulse with the first break of this arrival.

3.14. The arrivals plotted here correspond to the times $t_i$ in the reflection record shown in figure 3.12 plotted as a function of receiver position along the x-axis. The first arrival is the direct P-wave from the source (X's). The second arrival (triangles) is either the direct S-wave or the direct Rayleigh wave. The Third arrival corresponds to the first reflection off of the bottom of the block (asterisks). The lines through the points are the calculated least-square fit to velocity for each set of arrivals.

3.15. If we set the left side of Eq.3 equal to a quantity (A):

$$A = \left|2 - \frac{c^2}{\beta^2}\right|^2$$

And we set the right side of Eq. 3. equal to a quantity (B):

$$B = 4\left|1 - \frac{c^2}{\alpha^2}\right|^{\frac{1}{2}} \left|1 - \frac{c^2}{\beta^2}\right|^{\frac{1}{2}}$$

then the points where A=B will correspond to realisable solutions of Eq. 3. for set values of $\alpha$, $\beta$, and C. In this figure we assume we know $\alpha$ and $\beta$ and plot the quantities A and B against the unknown (C). The result is a value of .97 Km./sec. for the Rayleigh wave velocity.

3.16. In this figure we assume we know $\alpha$ and (C) , and we plot A and B against the unknown ($\beta$). The result is a shear velocity of 1.1 Km./sec.

3.17. The arrival times (in microseconds) of the direct signal from the source plotted as a function of position along the x-axis, measured in cm. describe a smoothly varying hyperbolic curve.

3.18. The entire suite of 441 direct arrival times are shown here as a function of total tavel-path (S). Where (S) is the direct-line distance from the center of the source to the receiver as described in the text. The line through these points corresponds to a least-square fit to ( $\frac{1}{V}$ ), and gives a velocity of 2.38 Km./sec.

3.19. This photograph was taken after the block was cut and machined, just before it was re-cemented together. The "crack" and the fluid access channels can be easily seen in this view.

3.20. The amplitude and arrival time of the first positive peak as a function of position along the x-axis for the second experiment as compared to the results from the first experiment. The amplitude shows a pair of peaks on either side of the central peak that can be explained by re-radiation from the crack. The arrival times, however, show no discernable effect due to the presence of the crack.

3.21. Waveforms recorded when the crack is filled with water are considered to be essentially equal to the unperturbed incident signal. The difference between the wet and dry waveforms at a given point, then gives just the signal radiated due to the presence of the crack. Since the differenced record is just a lower amplitude inverse of the incident signal it can be explained as re-radiation by the crack which has been excited by the incident P-wave. This figure shows two of the pairs of wet and dry records which were used to make the differenced records.

3.22. The wet (incident) record and the corresponding differenced record are shown here for the 0,0 point of the reference grid. The amplitude of the differenced record is about one-fifth that of the wet record for corresponding peaks.

3.23. We can roughly estimate the depth of the crack by assuming that the amplitude peaks seen in fig. 3.20 are caused by the superposition of the incident signal and in-phase energy re-radiated by the crack. The block is 13.7 cm. thick, so , if the peak occurs at $x = \pm 3$ cm., the signal from the source will have traveled a distance ($S_0$) given by eq. 8. In this case $S_0 = 14.02$ cm. If we assume that the re-radiated signal comes from the center of the crack and will give a peak in amplitude if it arrives in phase with the incident signal, we can then estimate the depth to the center of the crack by solving for a difference in travel path $\Delta S = \frac{\lambda}{2}$ . Where $\Delta S = S_0 - S_1$ , and $S_1 = S_{1a} + S_{1b}$ . In the case of our model if we take $S_{1a} = 6.6$ cm., this would give $S_1 \sim 14.25$ . Then $\Delta S$ will be ~.22 cm which is $\sim\frac{\lambda}{2}$. This means we can explain the amplitude peaks by postulating an out of phase source in the center of the block.

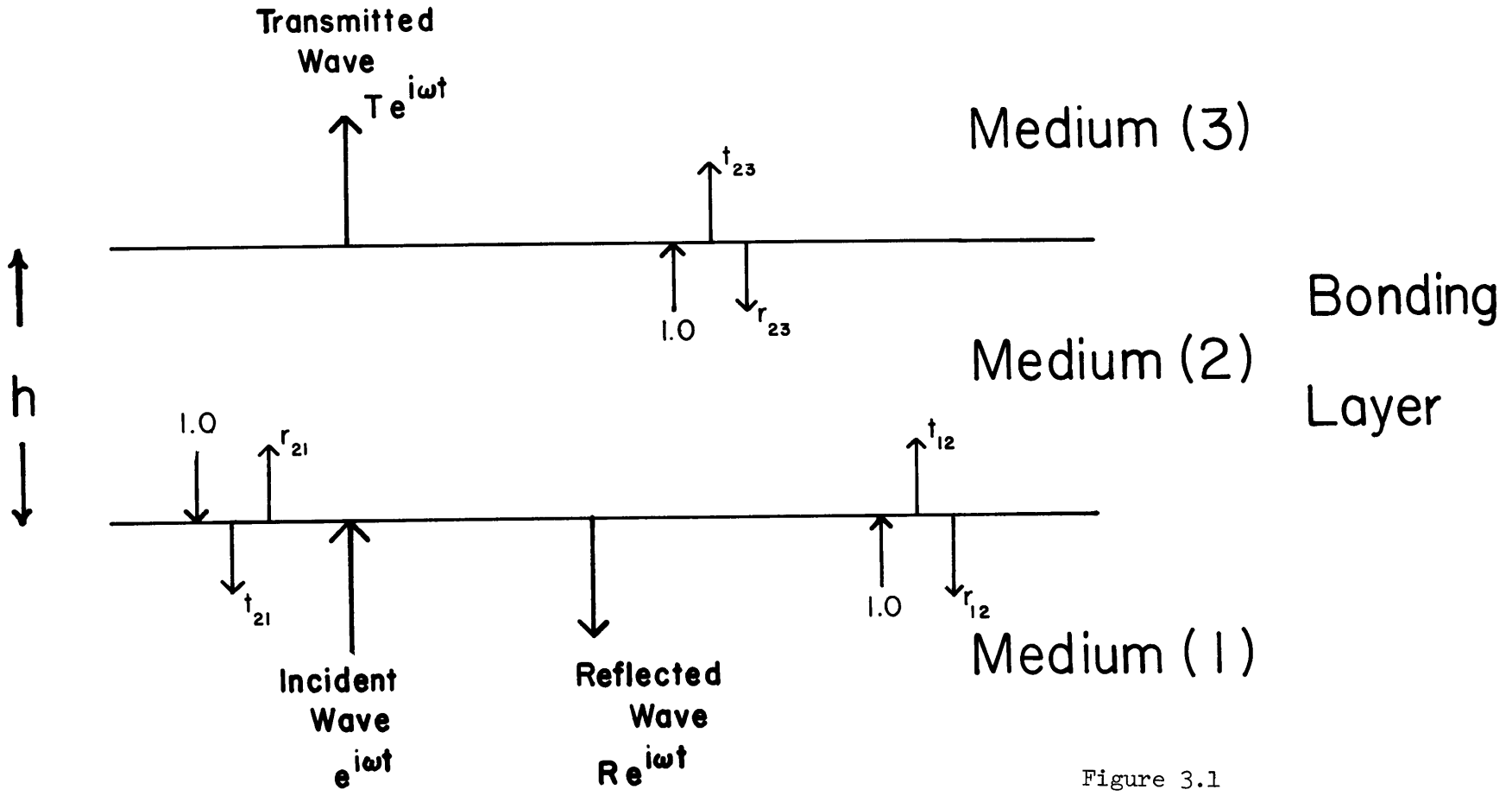
Transmitted
Wave
$Te^{i\omega t}$
Medium (3)
$t_{23}$
1.0
$r_{23}$
Bonding
Layer
Medium (2)
h
1.0
$r_{21}$
$t_{12}$
$t_{21}$
1.0
$r_{12}$
Medium (1)
Incident
Wave
$e^{i\omega t}$
Reflected
Wave
$Re^{i\omega t}$

Figure 3.1

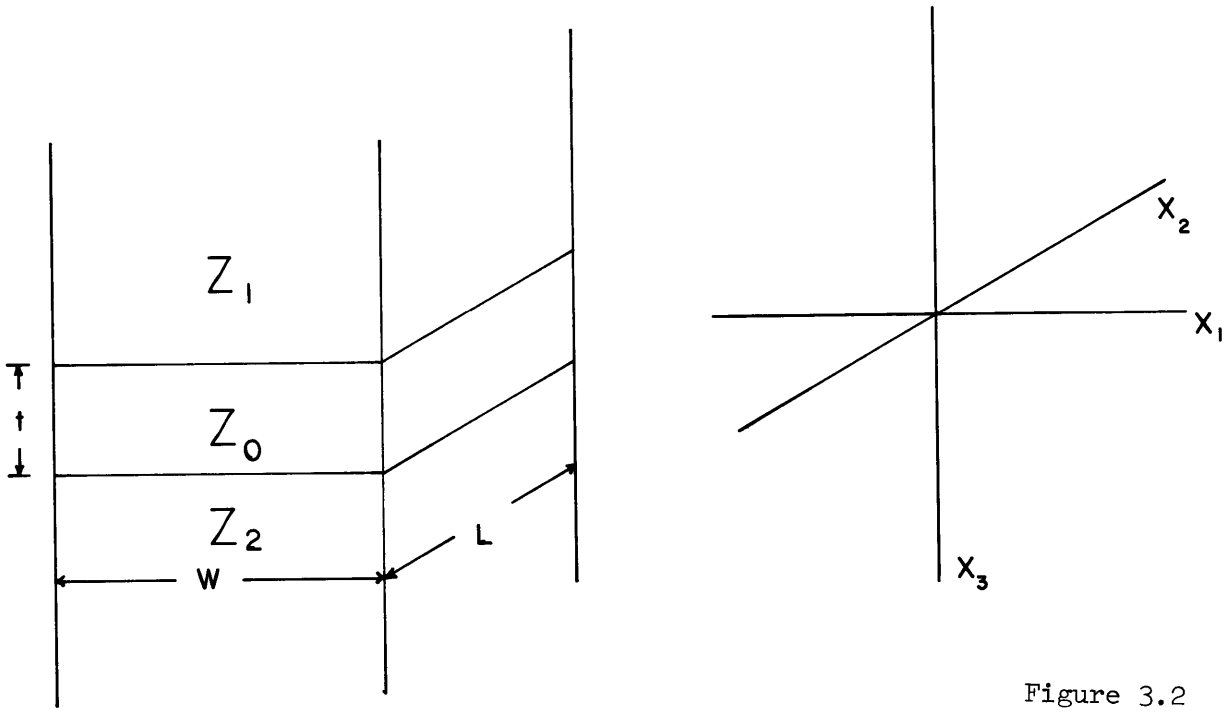


Figure 3.2

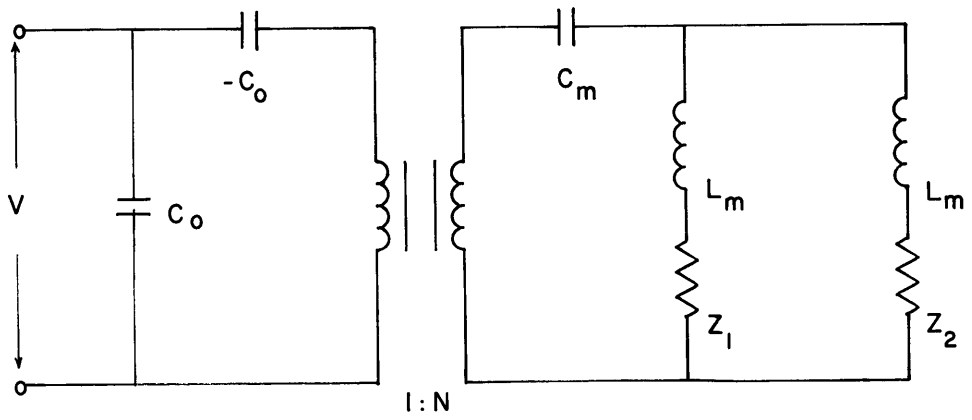

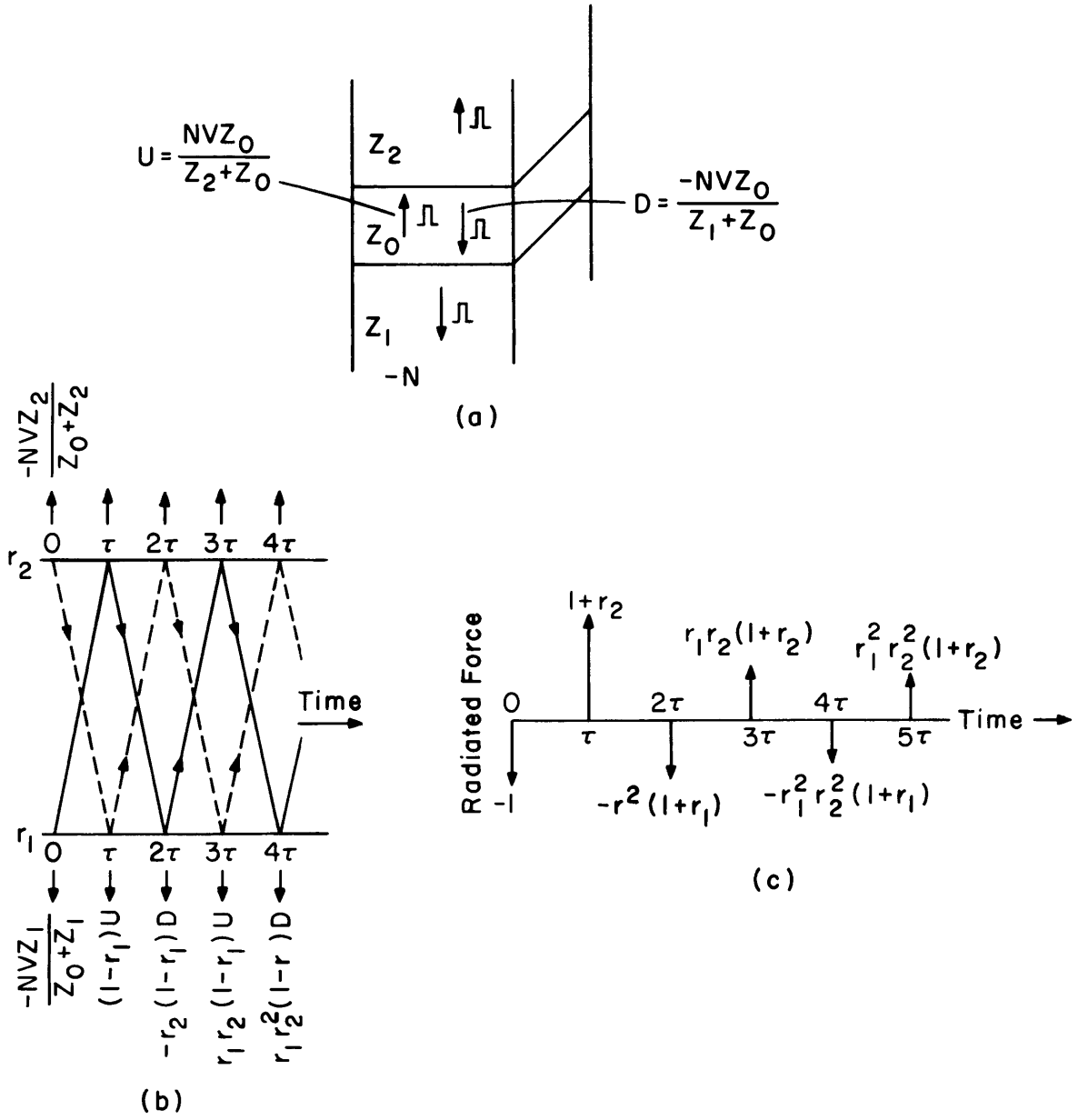


Transducer as Source

Figure 3.3

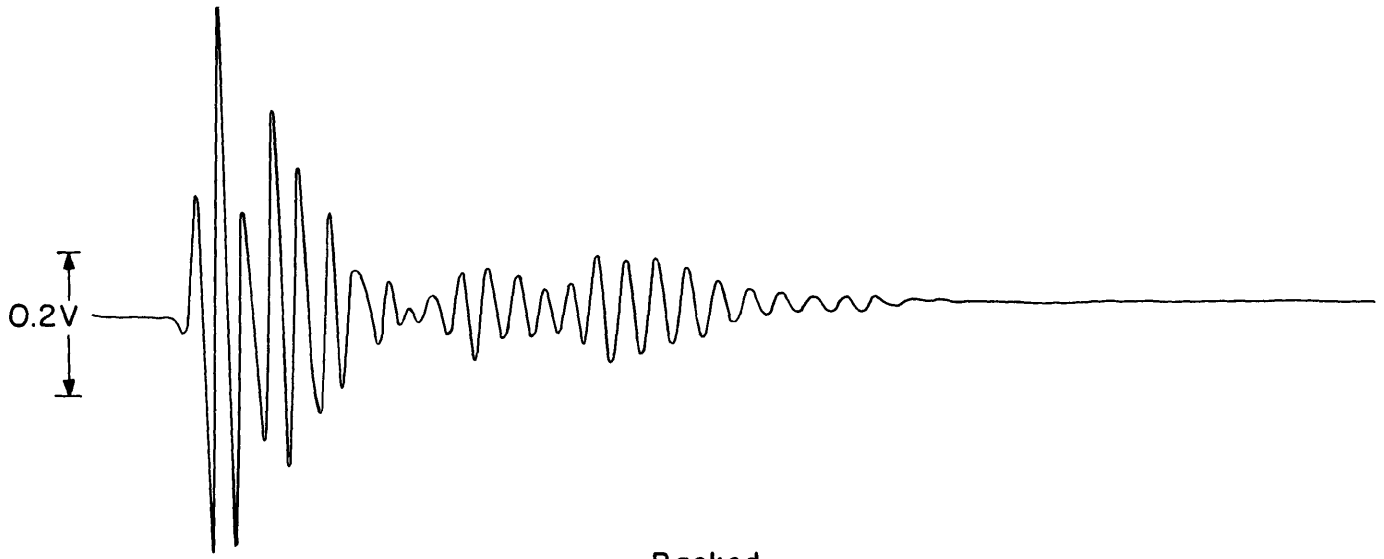


Figure 3.4

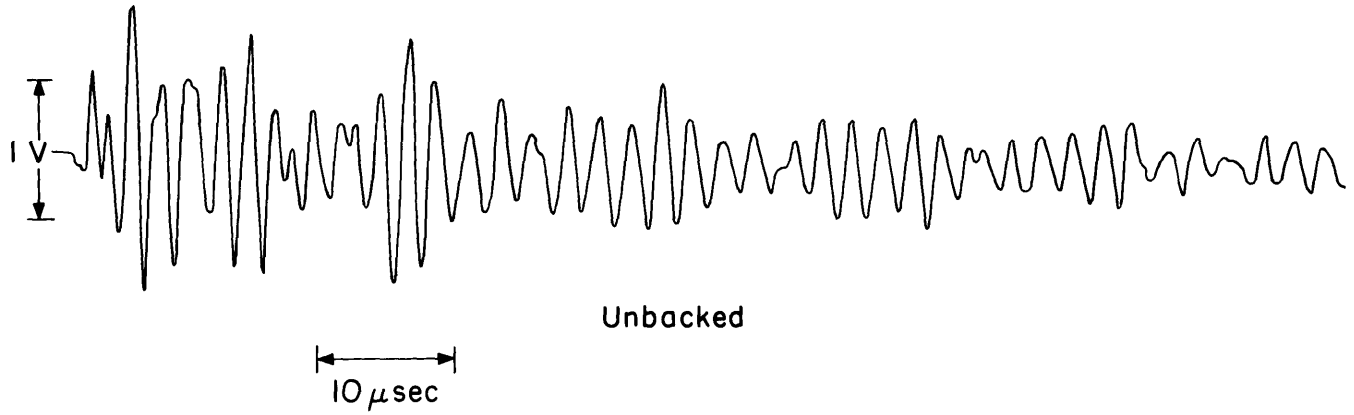

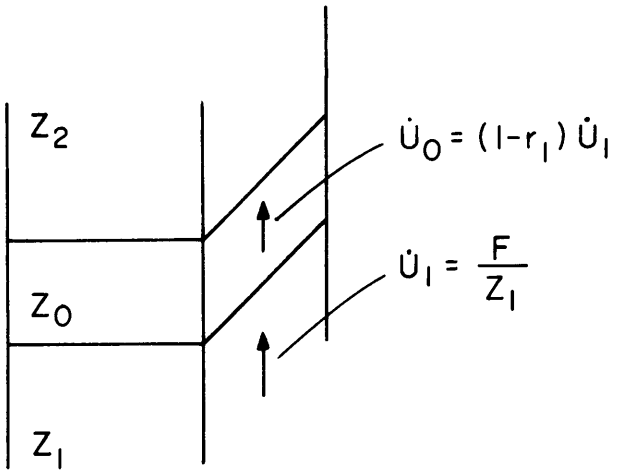


(a)

Figure 3.5

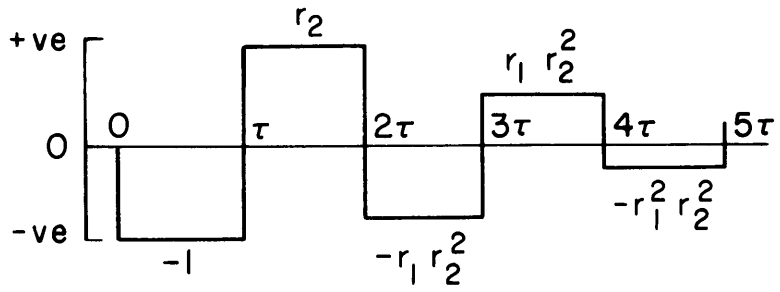


(c)

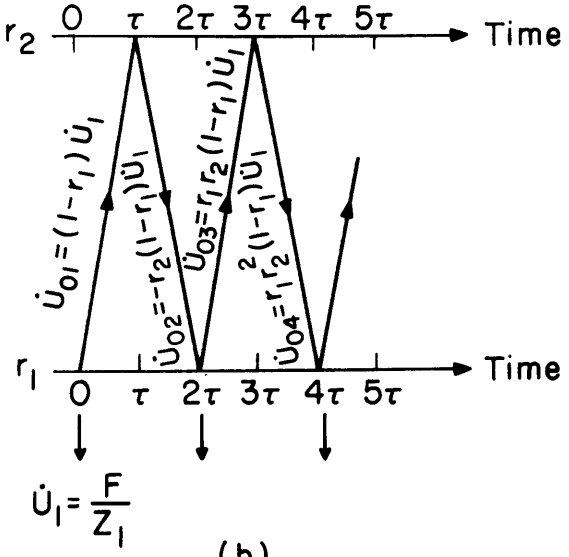


(b)

Transducer as Receiver

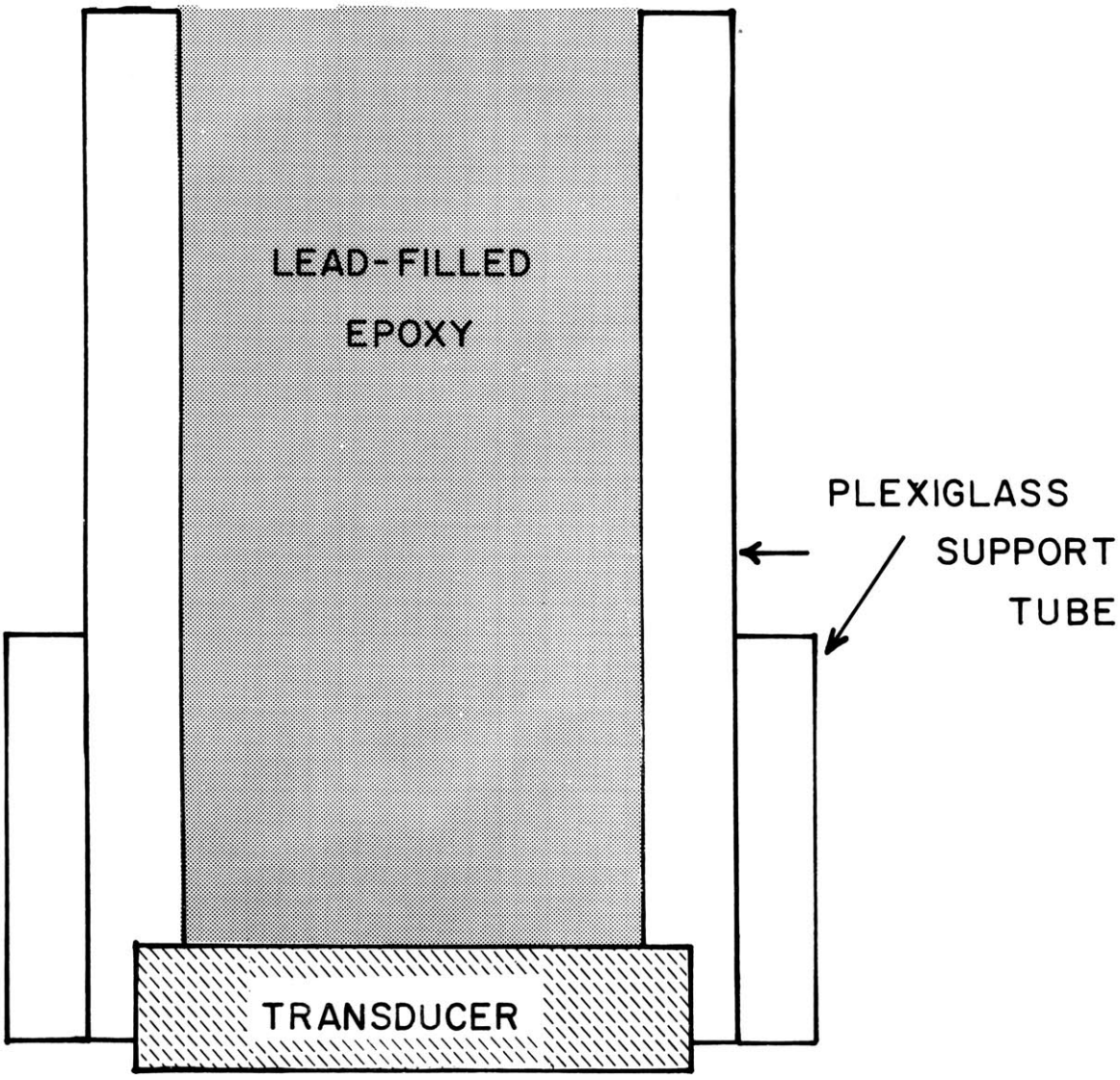
LEAD-FILLED
EPOXY
PLEXIGLASS
SUPPORT
TUBE
TRANSDUCER
SOURCE

Figure 3.6

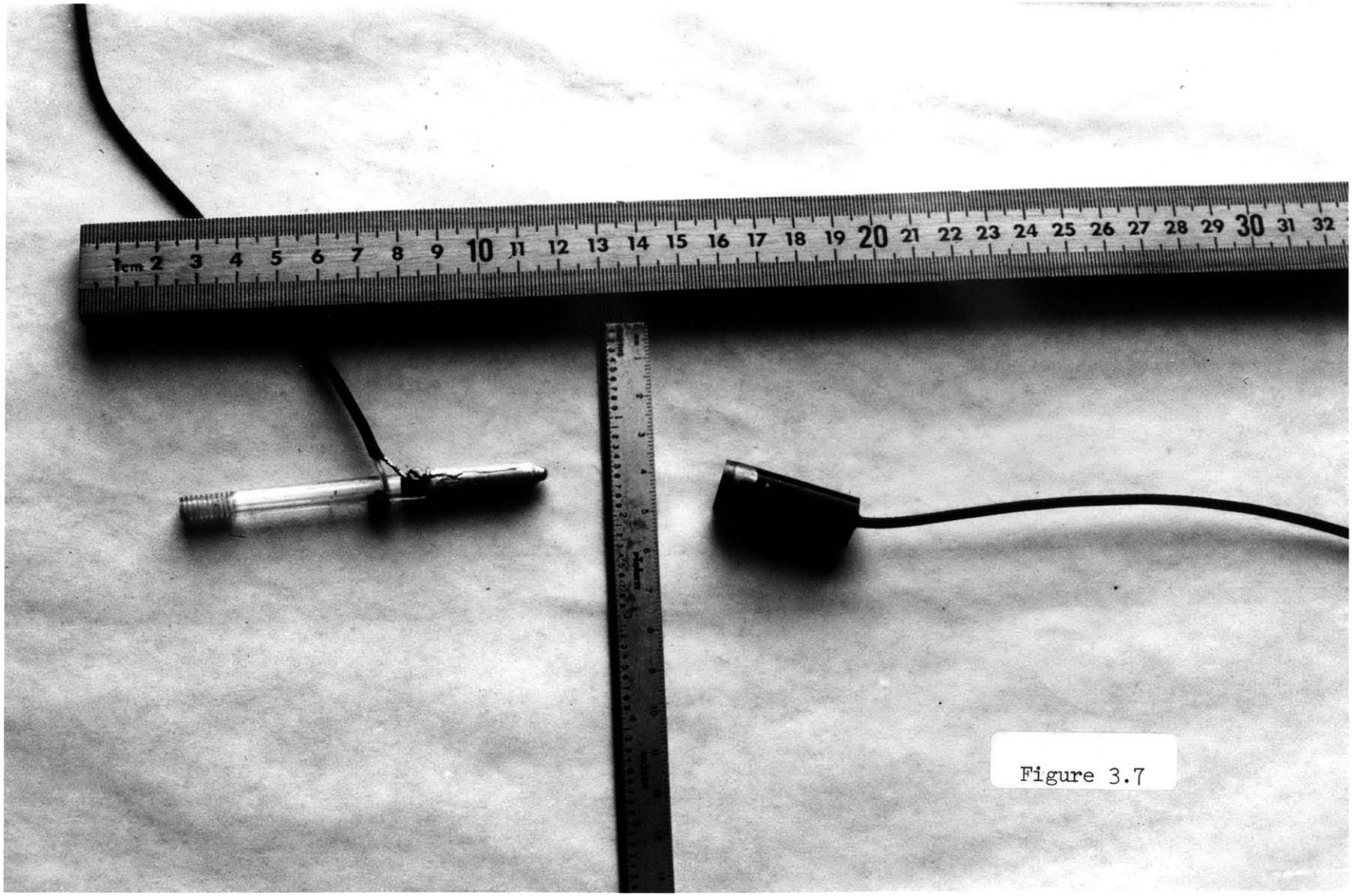
1cm 2 3 4 5 6 7 8 9 10 11 12 13 14 15 16 17 18 19 20 21 22 23 24 25 26 27 28 29 30 31 32

Figure 3.7

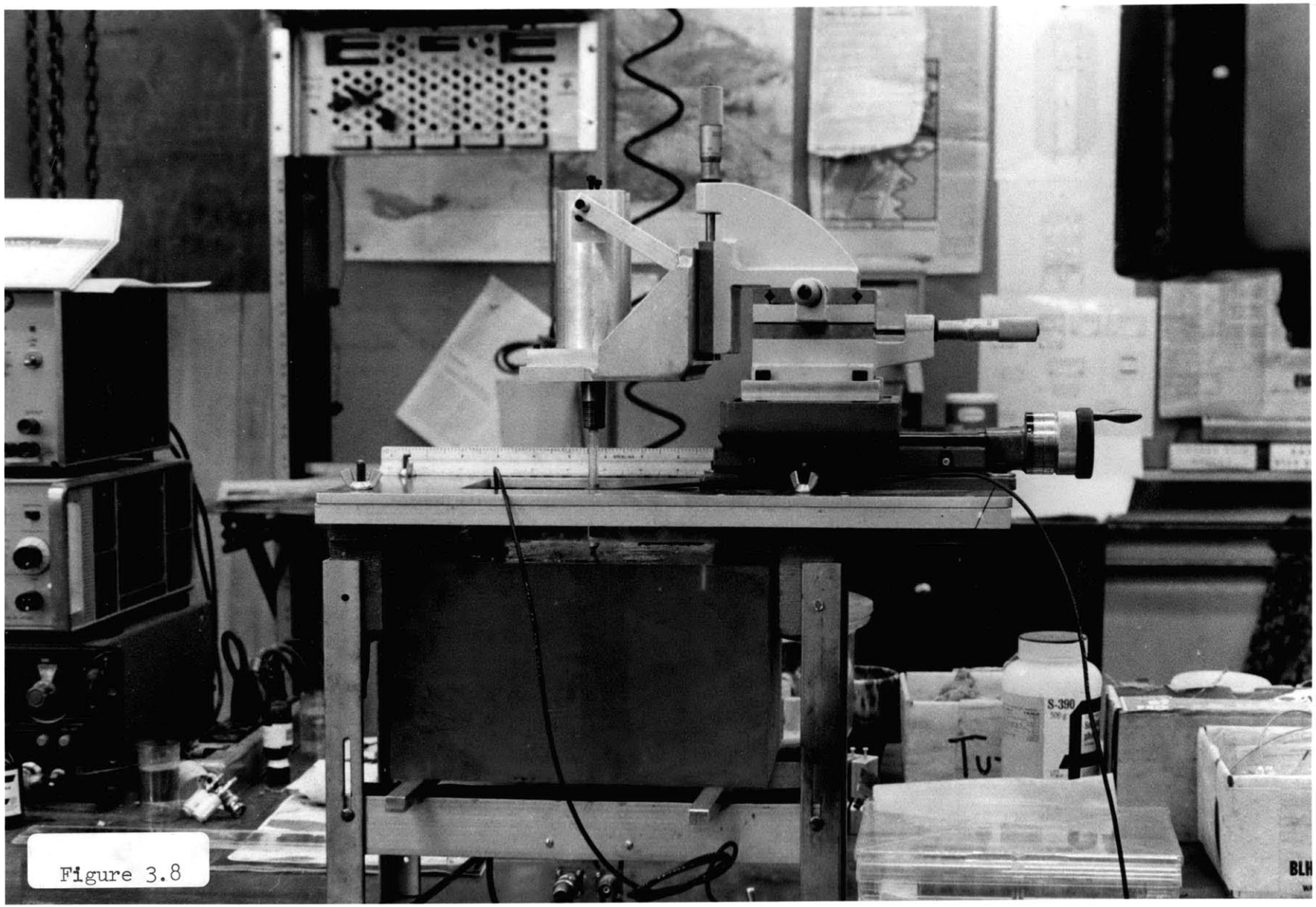


Figure 3.8

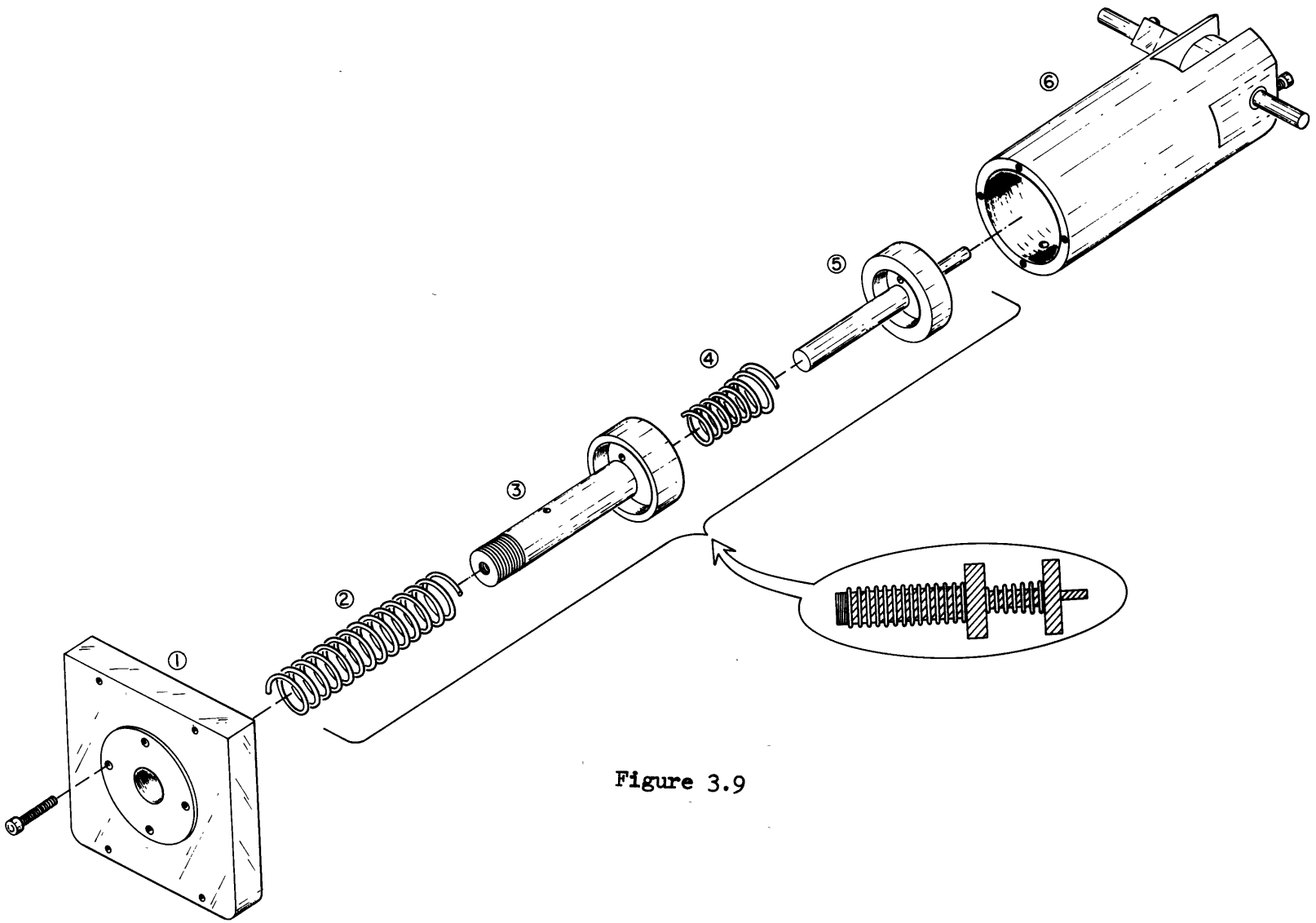


Figure 3.9

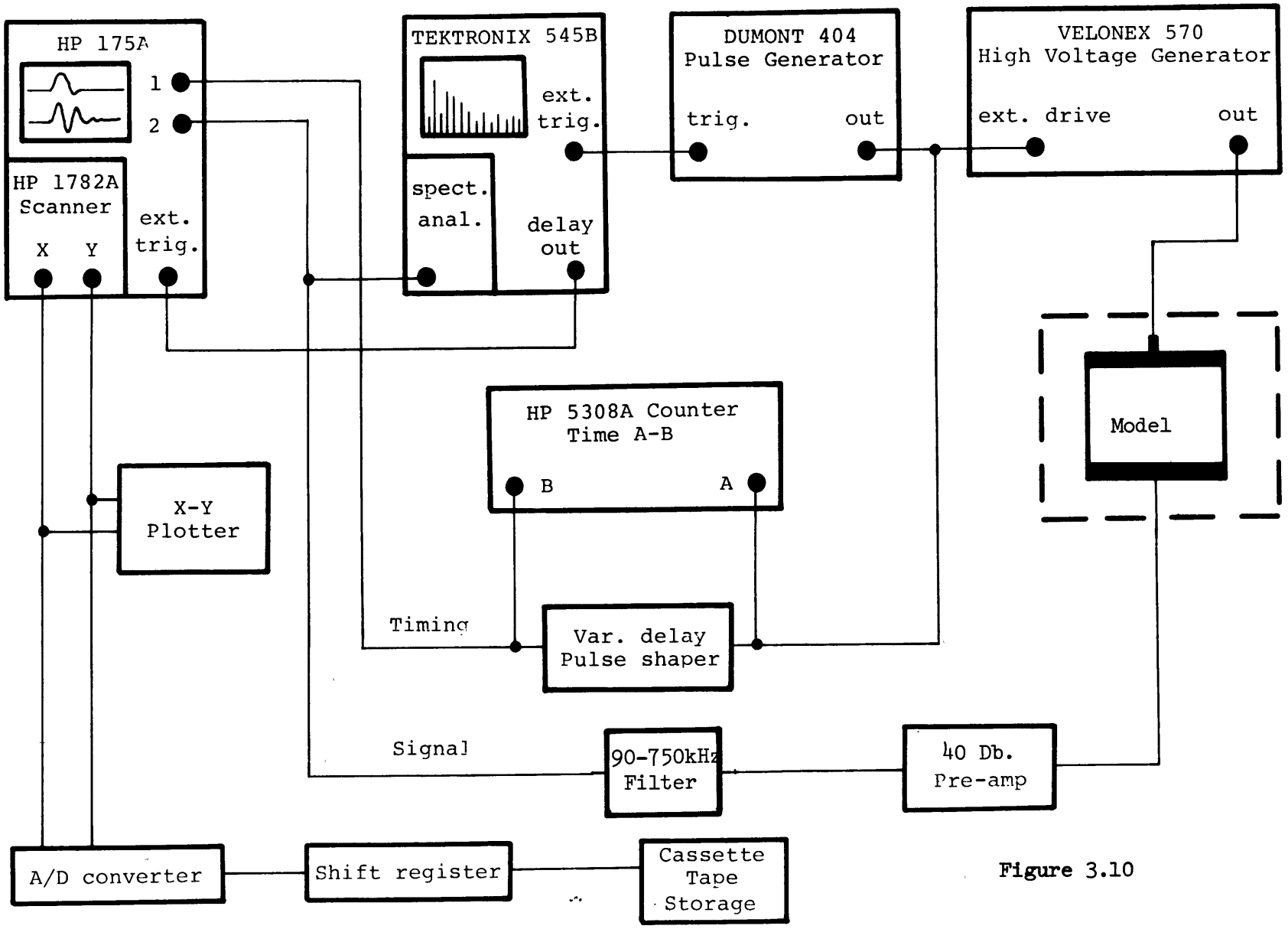
HP 175A
1
2
HP 1782A
Scanner
X
Y
ext.
trig.
TEKTRONIX 545B
ext.
trig.
spect.
anal.
delay
out
DUMONT 404
Pulse Generator
trig.
out
VELONEX 570
High Voltage Generator
ext. drive
out
Model
HP 5308A Counter
Time A-B
B
A
X-Y
Plotter
Timing
Var. delay
Pulse shaper
Signal
90-750kHz
Filter
40 Db.
Pre-amp
A/D converter
Shift register
Cassette
Tape
Storage

**Figure** 3.10

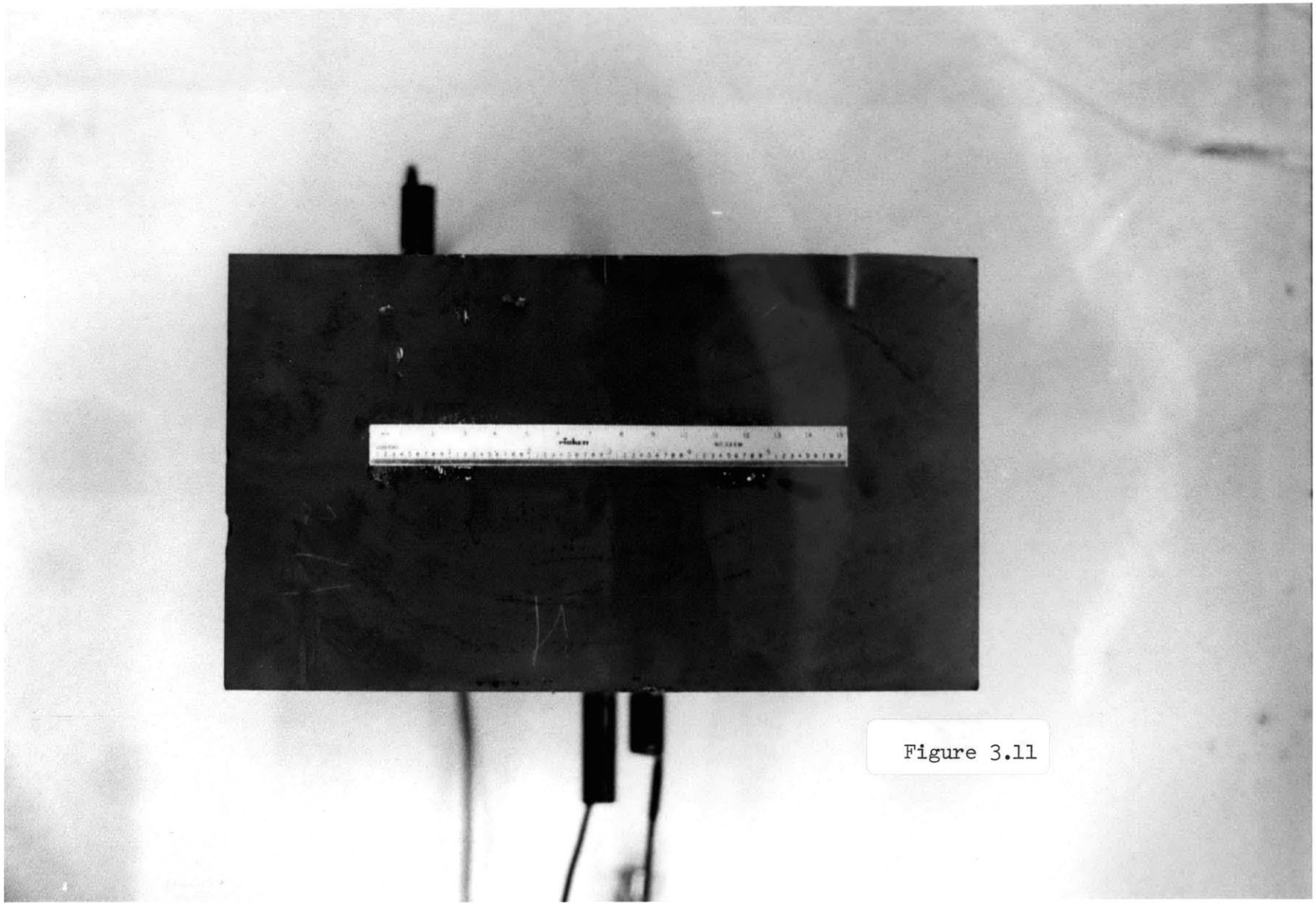

Figure 3.11

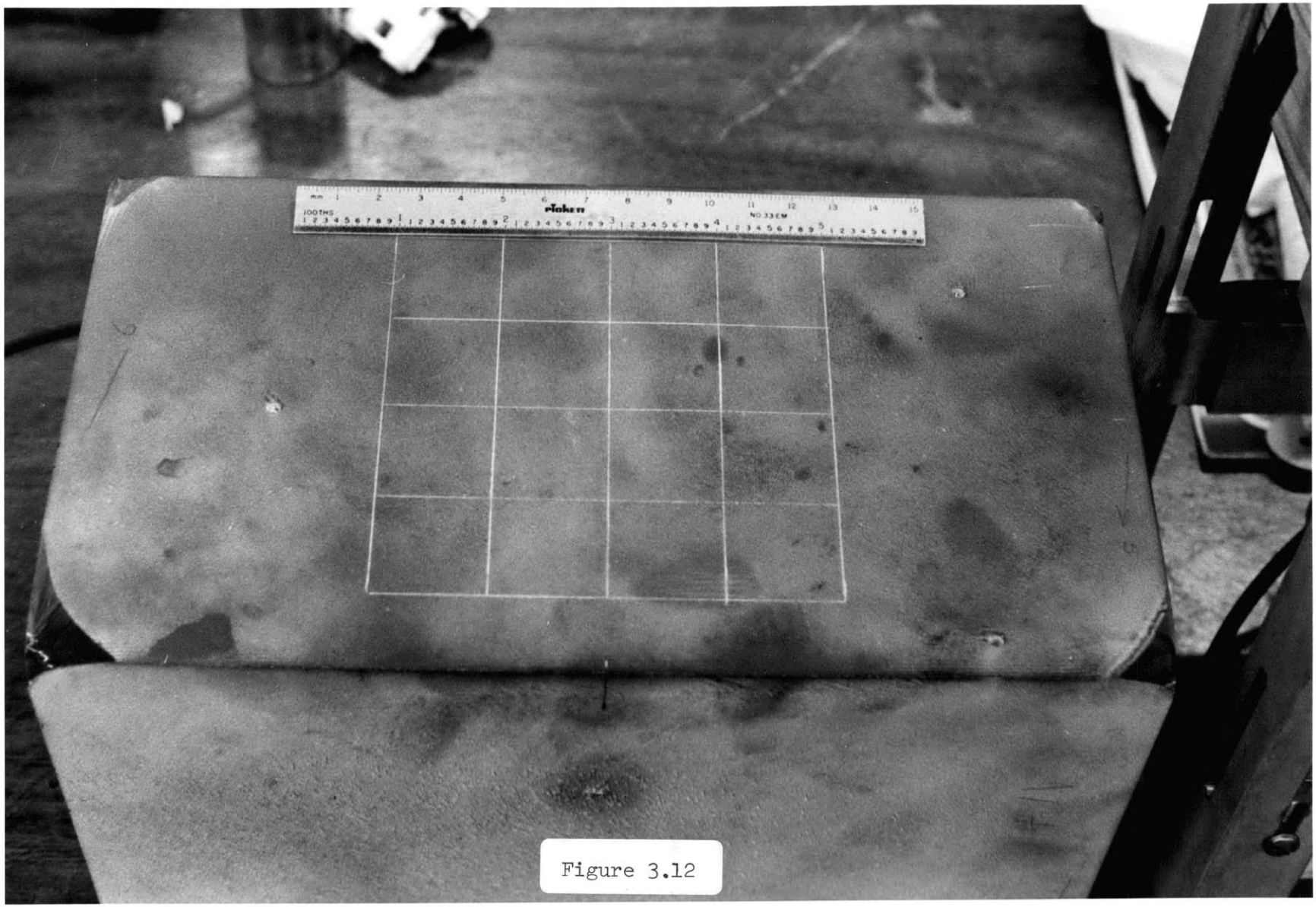

Figure 3.12

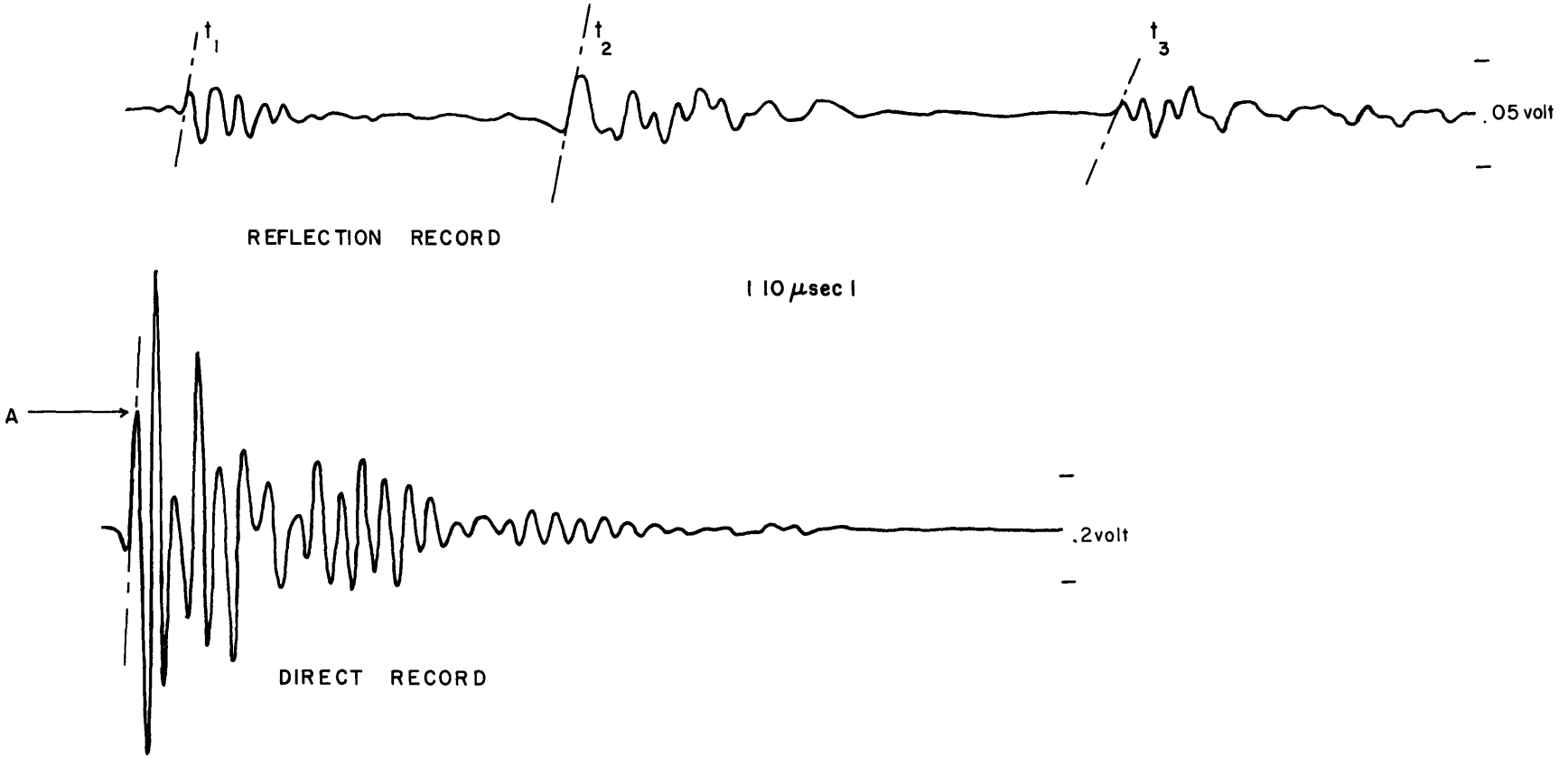


**MODEL SEISMOGRAMS for (2.54, 0)**

Figure 3.13

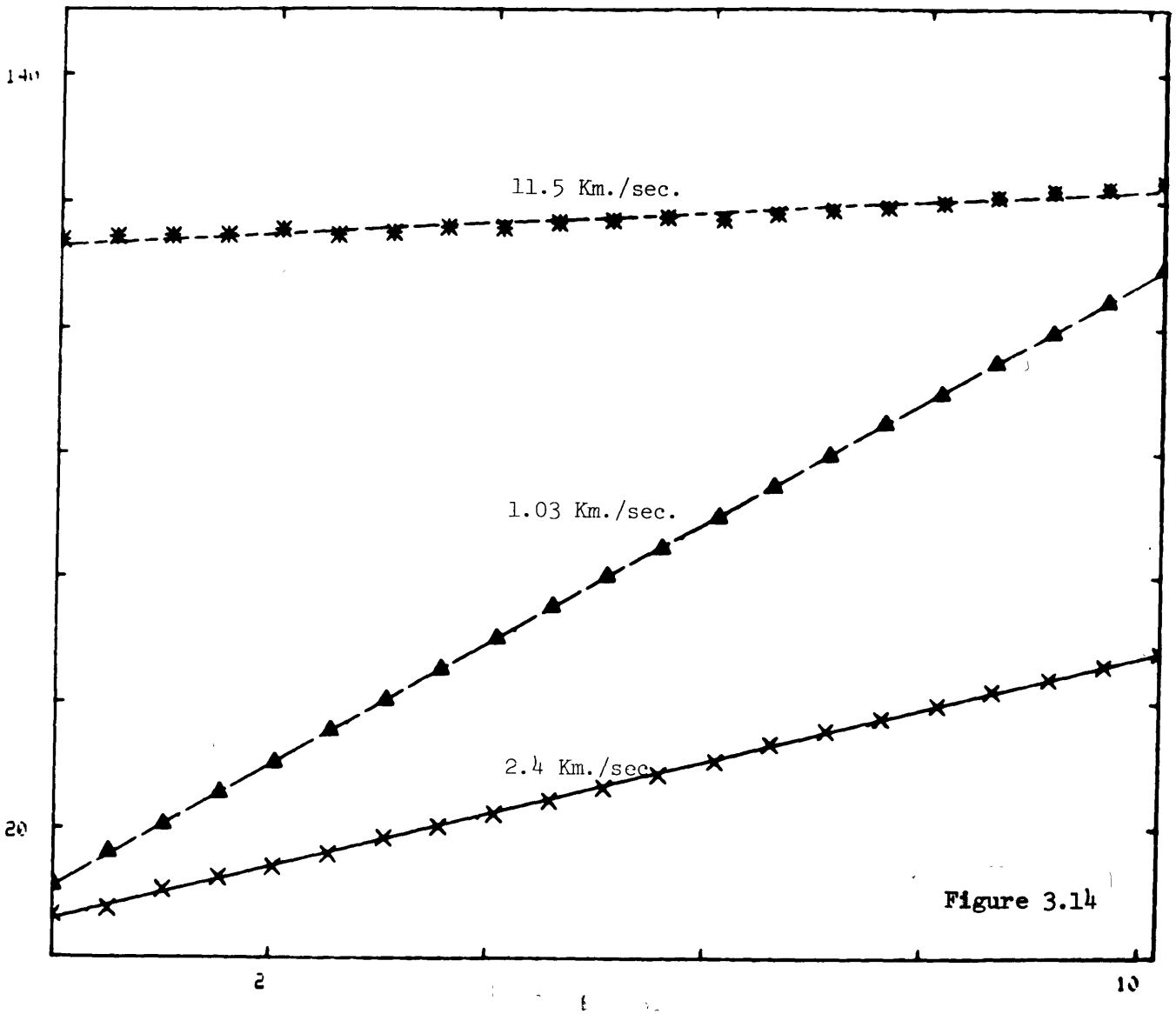


**Figure 3.14**

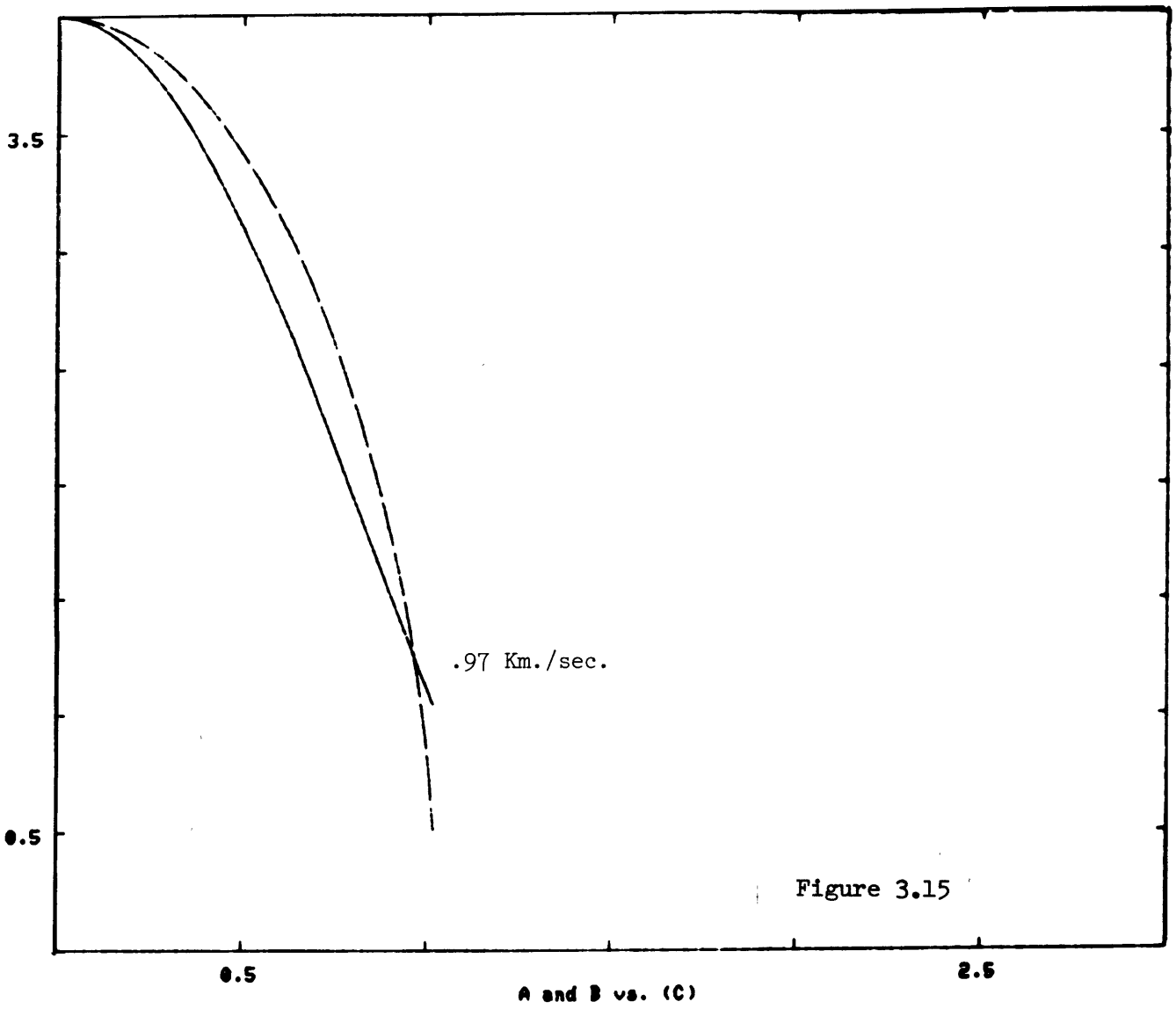


Figure 3.15

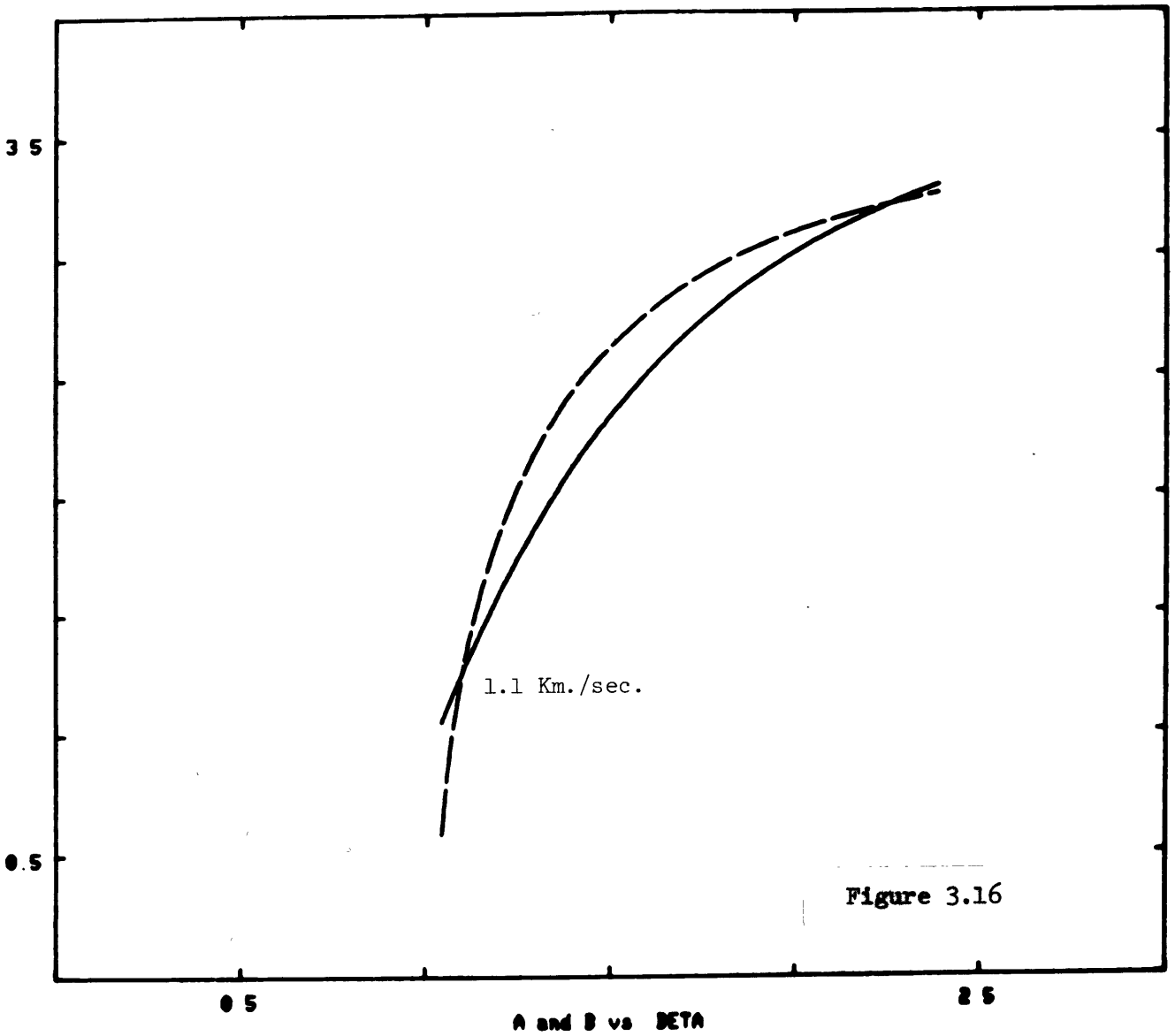


Figure 3.16

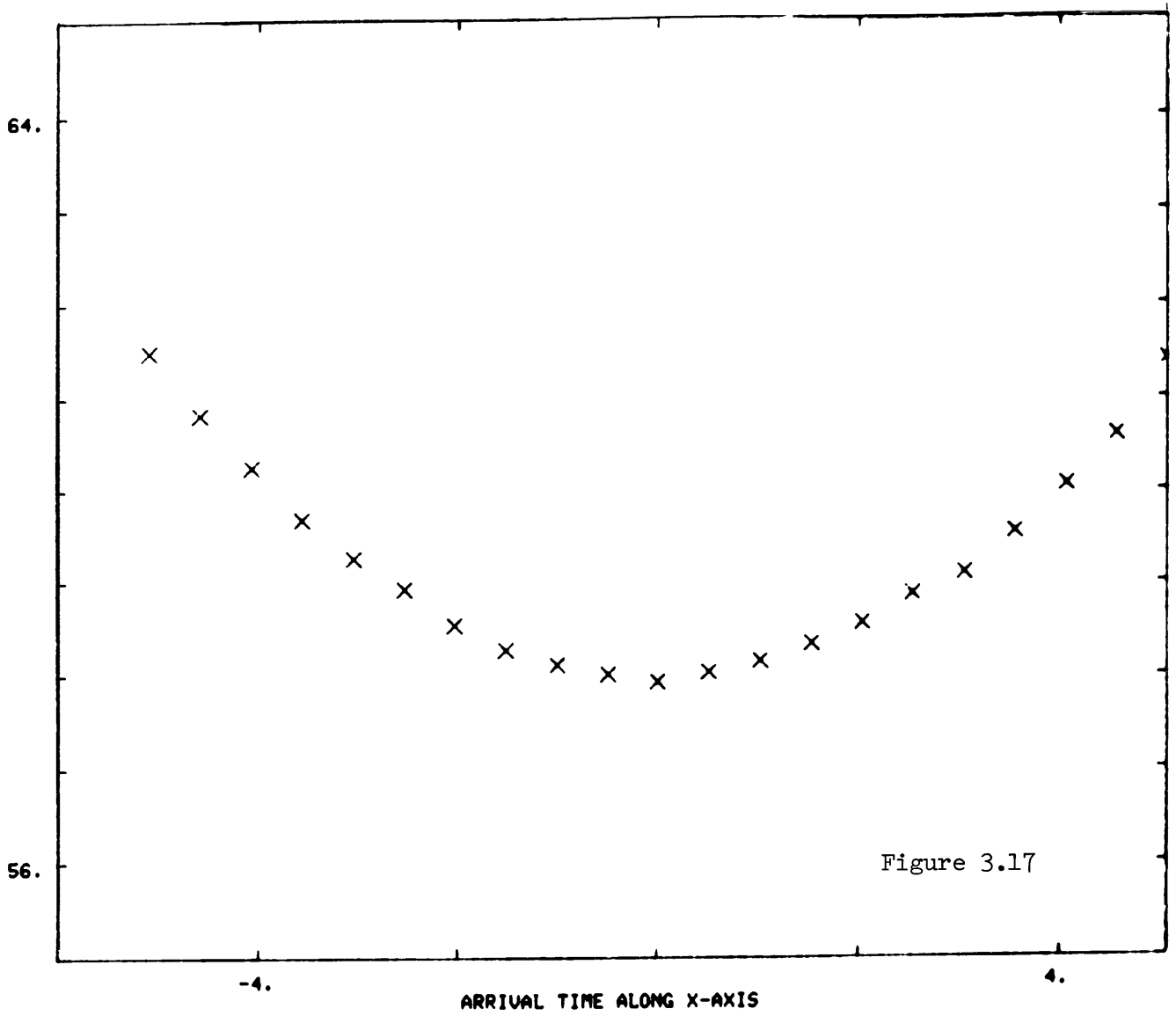


Figure 3.17

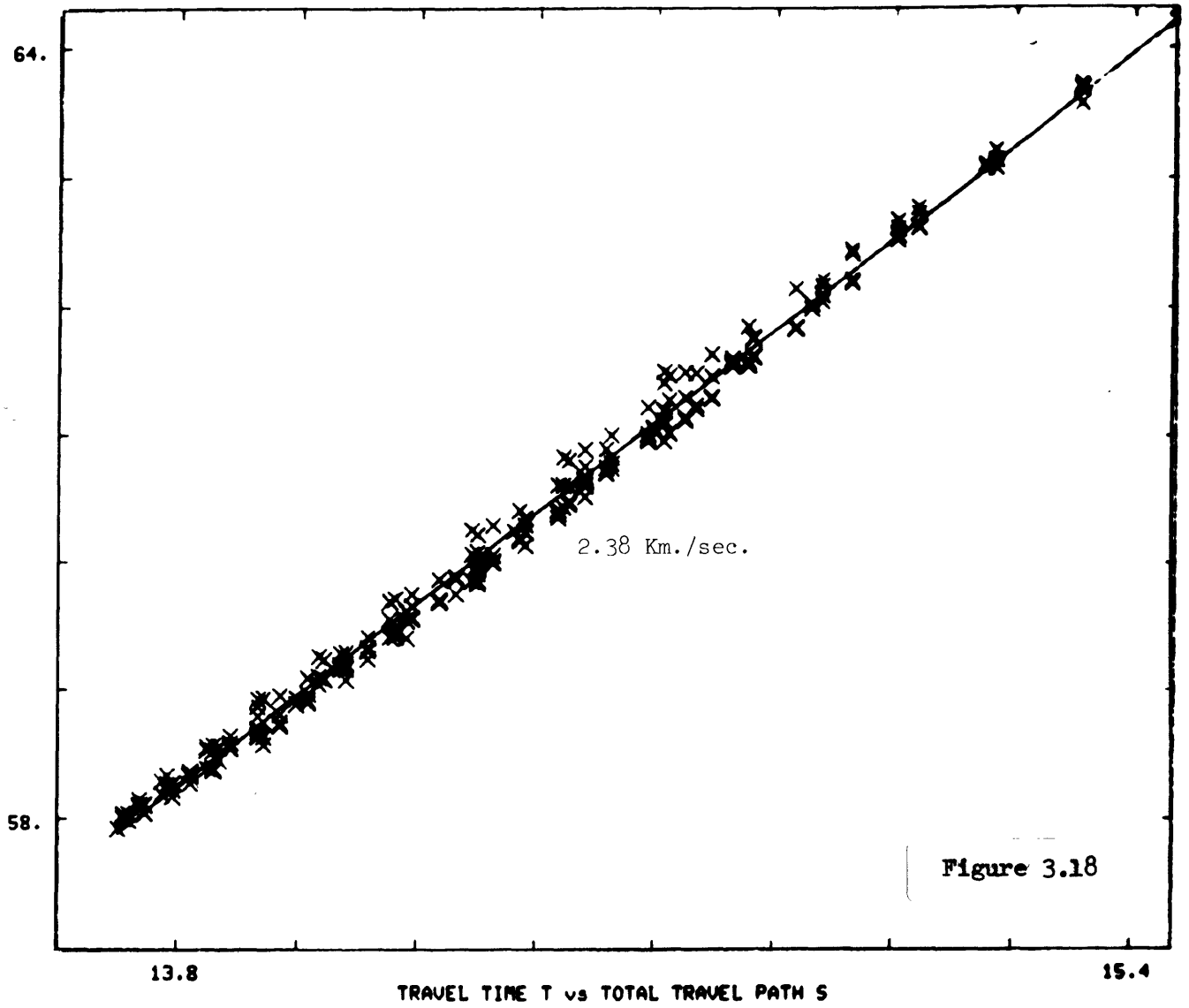


Figure 3.18

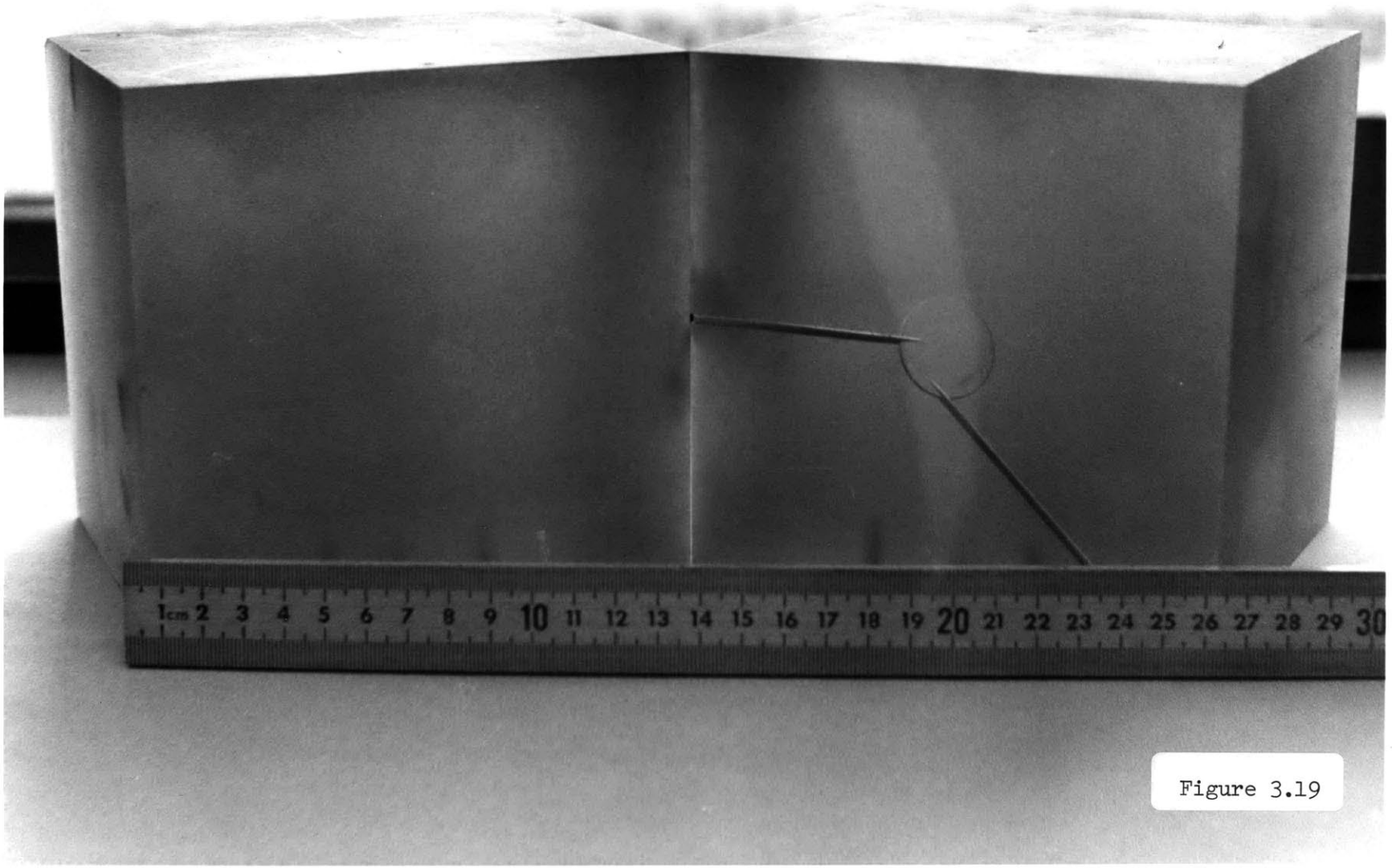
1cm 2 3 4 5 6 7 8 9 10 11 12 13 14 15 16 17 18 19 20 21 22 23 24 25 26 27 28 29 30

Figure 3.19

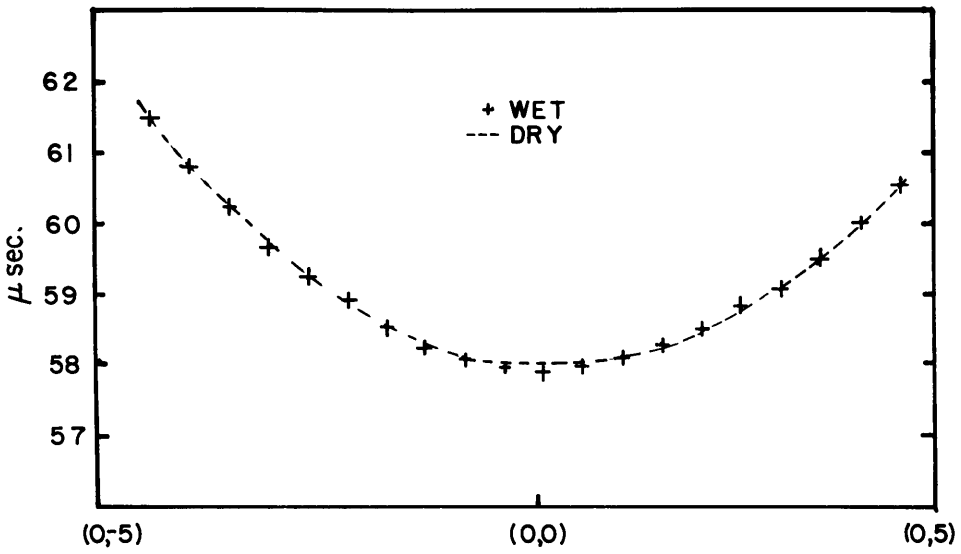


ARRIVAL TIME

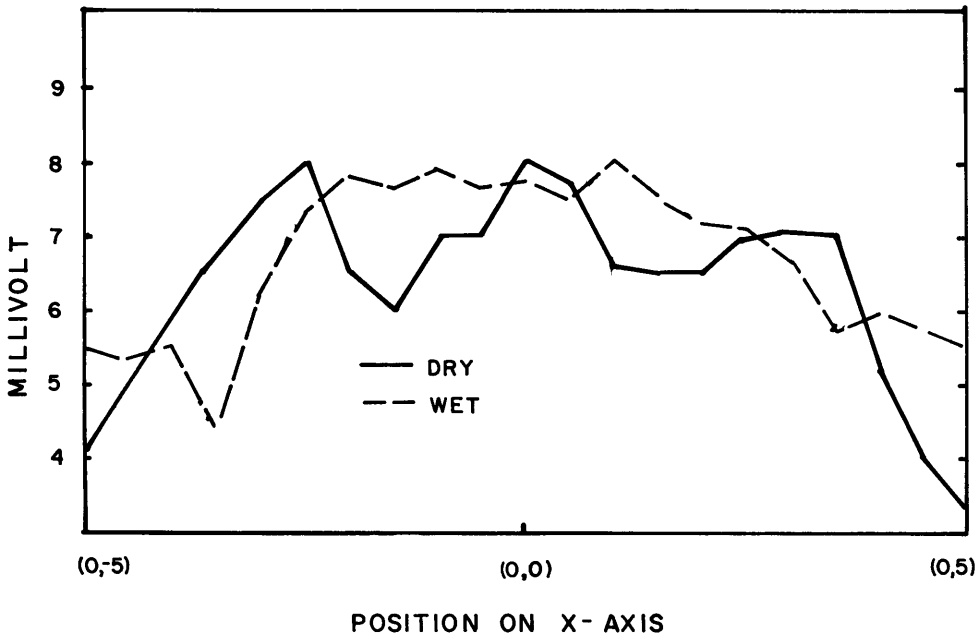


AMPLITUDE

Figure 3.20

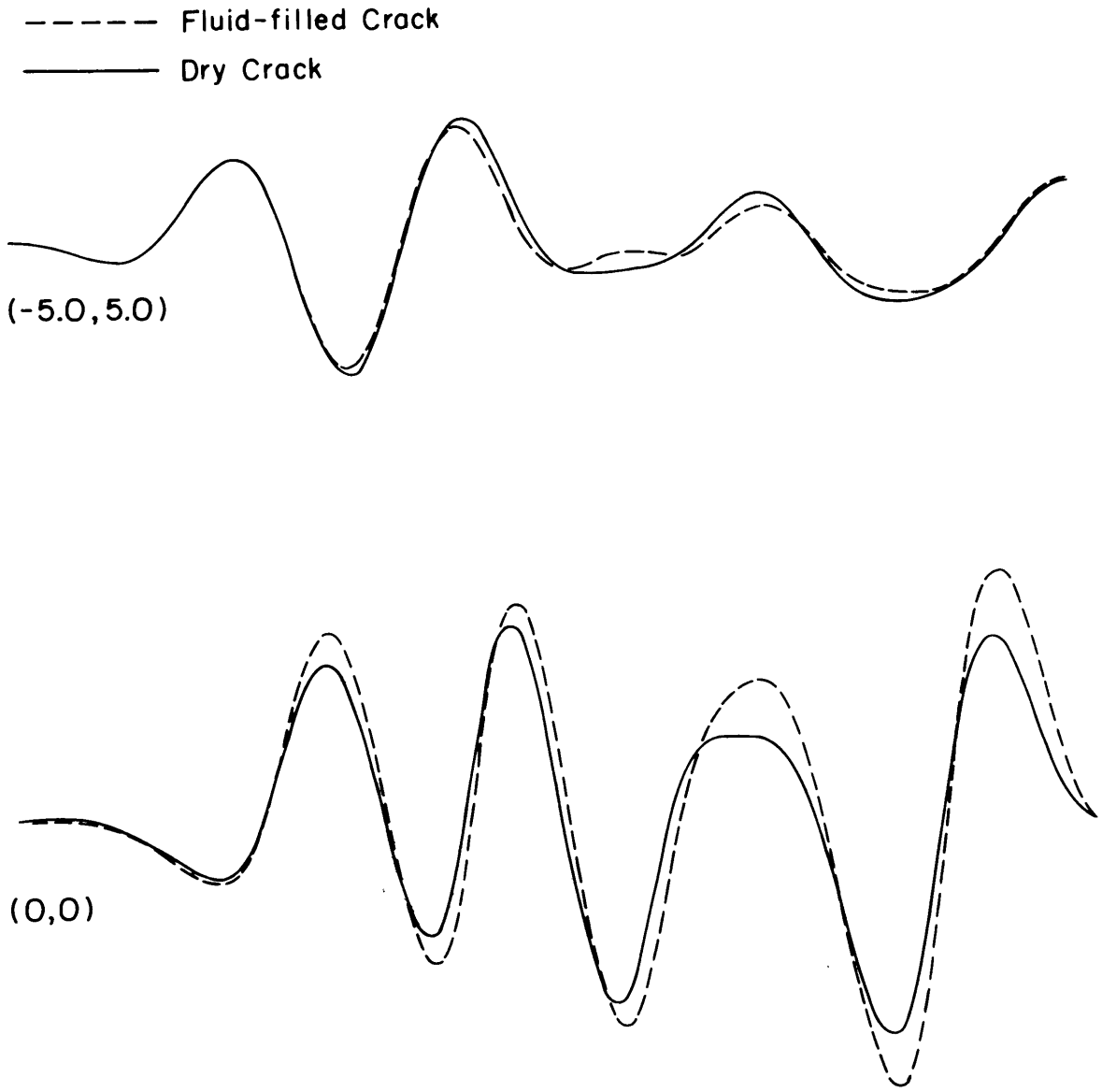


Figure 3.21

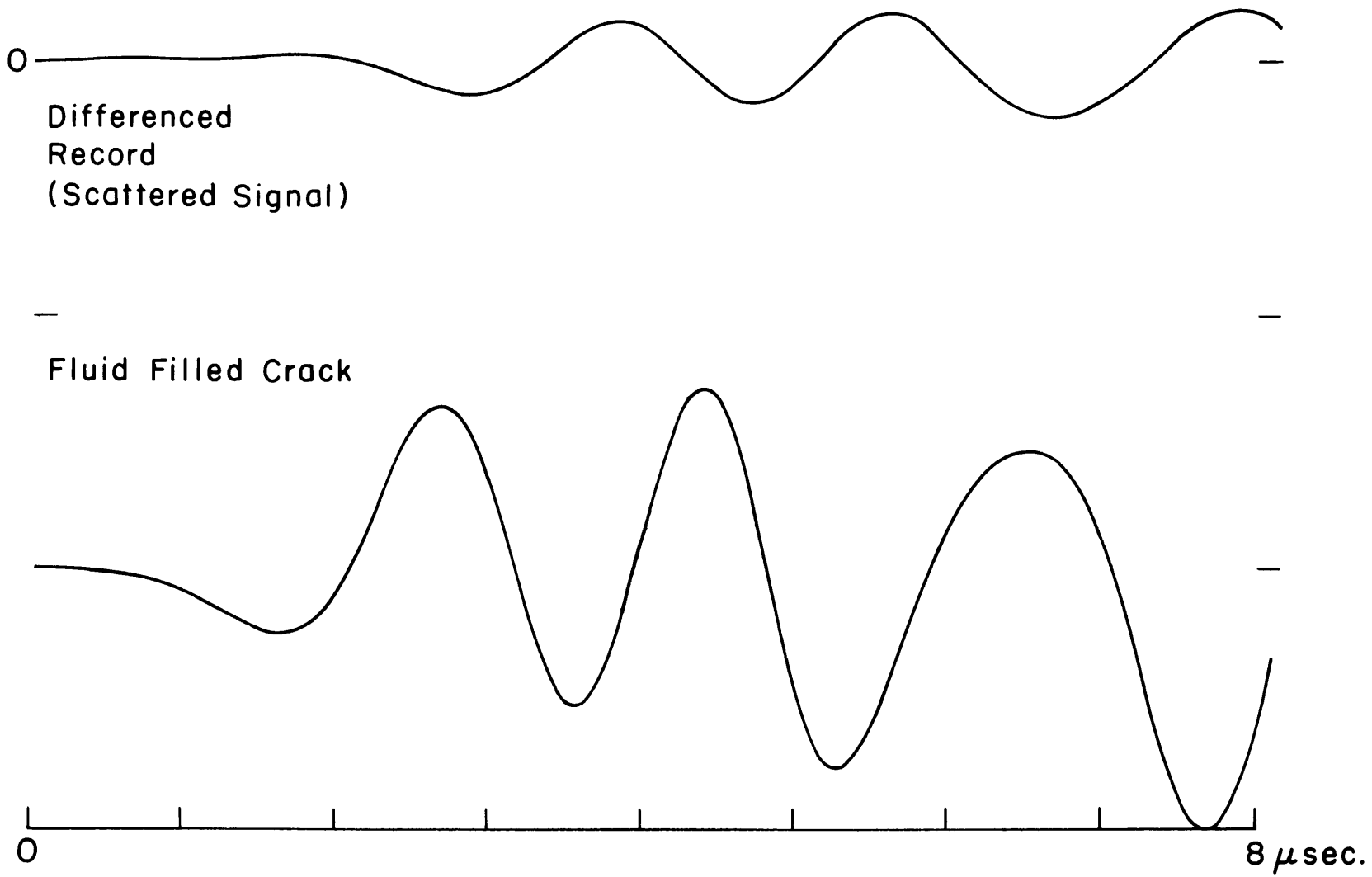


Model Seismograms Recorded at (0,0)

Figure 3.22

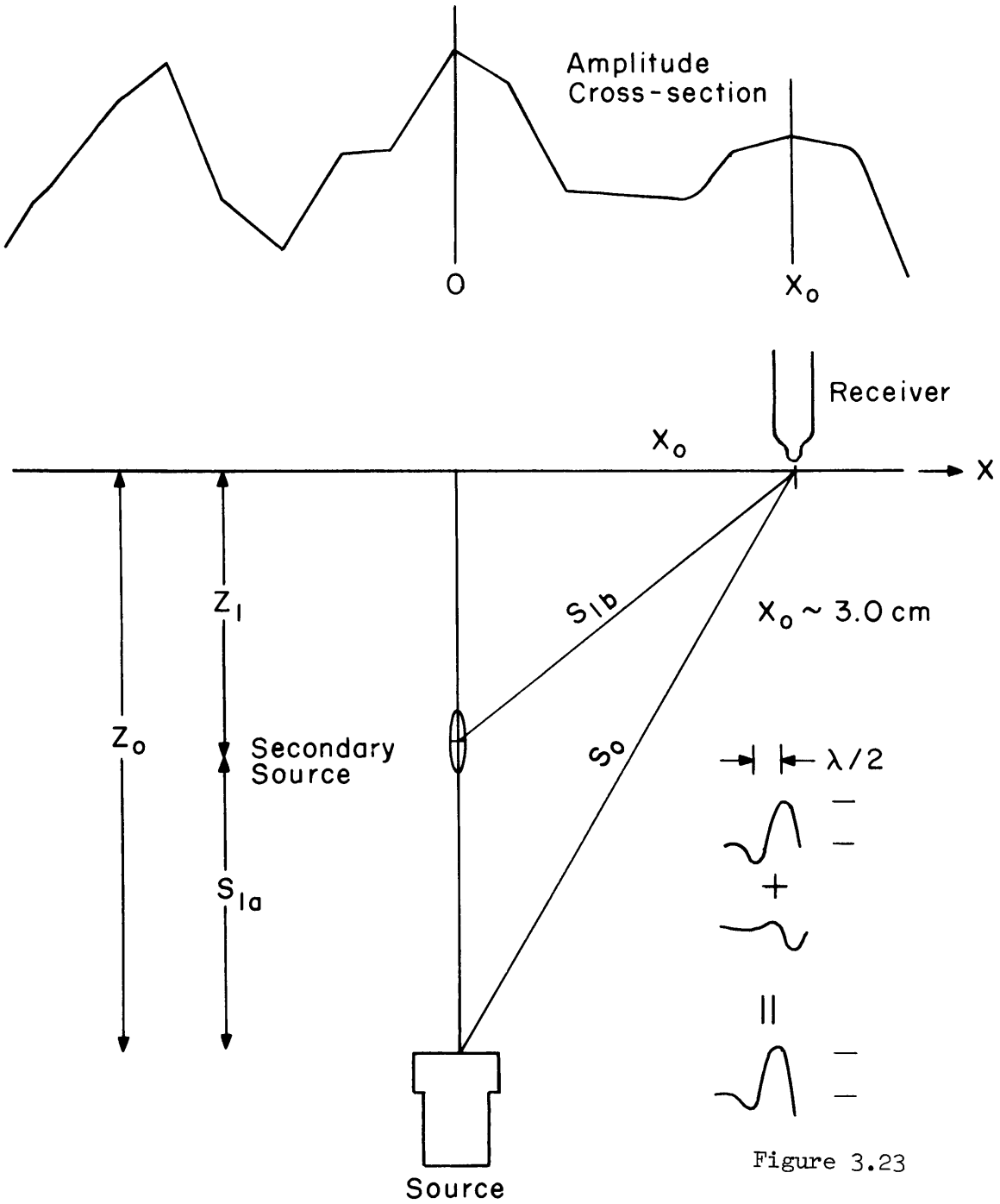
Amplitude
Cross-section
0
$X_o$
Receiver
$X_o$
X
$Z_1$
$S_{1b}$
$X_o \sim 3.0$ cm
$Z_o$
Secondary
Source
$S_o$
$\lambda/2$
$S_{1a}$
Source

Figure 3.23

# 4. ANALYSIS OF RESULTS

The first experiment was conducted solely to establish the model's parameters, so we will begin this chapter with an analysis of the second experiment. The second experiment was tailored to the collection of data for the wavefront reconstruction technique. We start with a general discussion of the sources of error in the recording technique and proceed to the discussion of the wavefront reconstruction results.

## 4.1. RESULTS FROM WAVEFRONT RECONSTRUCTION

### 4.1.1. SOURCES OF ERROR

After the block was machined for the second experiment and re-glued, the arrival times and amplitudes of the first positive peaks were recorded over a 21 x 21 grid. The arrival times were determined by measuring the delay required to align the timing pulse with the waveform. Fig. 4.1 shows the alignment of the timing pulse with a typical first arrival. By setting the scanning rate of the oscilliscope up to .5 microsecond per cm., the precision and repeatability of arrival time measurements were greatly enhanced. Repeated measurements at the same point varied by approximately $\pm$.02 microsecond. Noting the slight deviations of the observed times from the fitted lines in fig.3.14 demonstrates that this accuracy is adequate for our purposes.

While errors in travel time measurement are small, errors in amplitude measurement increase as the amplitude of the signal increases. This occurs because the amplitudes are measured

directly on the screen of the oscilliscope. As the amplitude of the signal increases, the gain of the oscilliscope must be decreased to fit all of the trace onto the screen. The precision to which the screen can be read is about ± .5 mm. Over the range of scope gains used, the precision results in a range of amplitude errors of ± .1 mv. for the smallest, to ± .5 mv. for the largest signals. Though this amplitude error increases with amplitude, it is always a fixed percentage of the amplitude.

In the derivation of the wavefront reconstruction technique, a monochromatic scalar wave field was assumed. We now have enough information from the experiment to determine if our data meets this criterion. Fig. 4.2 shows the spectrum of the first 50 microseconds of three typical waveforms. If we restrict our attention to the first 10 microseconds of signal we are assured of an effectively monochromatic signal. To verify the scalar nature of the wavefield we refer to the measured P and S velocities, and the known structure of the model. The minimum P-wave travel time from the source to the recording plane is 57.9 microseconds. The travel time for an S-wave along the same path would be 100 microseconds, or, well into the coda of the record. Even if the crack were to scatter significant amounts of S energy, the differential travel time between the P and S signals would be over 20 microseconds. So, by limiting our attention to the first 10 microseconds of the record, we ensure that we will record only P-wave energy in a narrow band around 500 kHz. Having verified that the data are amenable to the use of the wavefront reconstruction technique, let's verify that the technique gives reasonable results.

The recorded arrival times for each grid point were converted to phase lags by setting the phase of the earliest arrival to zero and dividing the difference in arrival time by the measured period of the signal. So, at each grid point our data is now in the form $A\,e^{i\phi}$. The data were recorded over a 21x21 grid, but the reconstruction was done using a 45x45 grid. The amplitude values measured near the edge of the 21x21 grid were all on the order of 3 mv., which was the lowest measured amplitude. Also, as the edge of the grid was approached, the travel times became longer, with the values at the edge of the grid all being within .05 microsecond of each other. The 45x45 grid was constructed by filling out the grid with the lowest measured amplitude and latest arrival time. This had the effect of allowing energy to propagate out of the area of immediate interest, and reduced sideband problems. The $A\,e^{i\phi}$ values were converted to complex numbers for the reconstruction using:

$$\text{Complex Amplitude} = A(\cos(\phi) + i\sin(\phi)) \qquad \text{EQ 1}$$

In figure 4.3 we see the amplitude and phase of the first arrivals as recorded at the surface for the case where the crack is filled with fluid. Recalling the results of section 3.3.3, we know that this is very close to the unperturbed incident signal. To test the wavefront reconstruction technique, we used this data to reconstruct the spatial amplitude distribution at a depth of 25 $\lambda$, or, just above the source. The amplitude distribution a(x,y) is recovered from the complex amplitude A(x,y) by,

$$a(x,y) = \sqrt{(\text{Im } A(x,y))^2 + (\text{Re } A(x,y))^2} \qquad \text{EQ 2}$$

The results of this calculation are shown in fig. 4.4. Gratifyingly enough, we see that the energy converges to an area about five grid points on a side. Since the grid points in the figure correspond to the spatial sampling interval employed in the experiment ( 5 mm), we can estimate that most of the energy converges back to an area 2.5 cm on a side. Since the source tranducer was 1 cm in diameter, we have succeeded in propagating the wavefield back to a region on the order of the size of the source. We have shown here only the spatial amplitude distribution of the wavefield because the phase distribution of the reconstruction is somewhat more difficult to display and interpret. Fig. 4.5 shows the phase distribution calculated for the unperturbed wavefield in the center of the block. The interference-pattern-like rings are (according to Boyer, 1971, El Sum, 1967, and Boyer and Van Rooy, 1970) a manifestation of the Moire Effect we discussed in Chapter 2. For the purposes of interpreting the amplitude distributions, we need only to know that these are predominantly first-order rings, the higher-order rings , which give rise to spurious images, being outside the area of reconstruction. So, for our purposes, this effect does not impair the amplitude reconstructions, but makes contour plots of the phase inordinately "busy". It is for this reason that the remaining figures show only the amplitude distributions. Thus reassured, we now turn our attention to using the technique to determine the actual orientation of the crack from the recorded data.

## 4.1.2. RECONSTRUCTIONS

In the last chapter we used the amplitude distribution on the recording plane to show that the crack could lie in the center of the block. This provides a good starting point for picking a depth for reconstruction. Fig. 4.5 shows the amplitude distribution of the unperturbed wavefield (actually the field reconstructed for a water-filled crack.) at a depth of 15 $\lambda$, or 7.5 cm. We see that the energy is beginning to focus into a smaller region, but there is no readily apparant structure to the amplitude distribution. This lack of structure is in direct contrast to the reconstructed wavefield shown in fig. 4.6. This reconstruction is also for a depth of 15 $\lambda$, but the input data are for the case where the crack is dry. In these, and subsequent figures, the crack is located in the center of the plots between the two central + marks. The axis of the crack is along a line connecting these two marks, and the diameter of the crack is slightly less than the distance between the two marks. The most striking difference between fig. 4.5 and 4.6 is a sharp drop in amplitude along a line corresponding to the crack location for the case where the crack is dry. From such a reconstruction we could certainly infer the presence of some sort of scattering structure and narrowly define its orientation. We would be hard-pressed however to make a good quantitative estimate of its size.

We computed reconstructions for both the fluid-filled and dry crack at a number of depths in the range from 4 cm. deep to 9 cm. deep. For all of the fluid-filled crack reconstructions, The wave-

field showed no discernable symmetry or pattern. Another example of such a reconstruction is shown in fig. 4.8. The reconstructions for the dry-crack all showed the same basic structure; a sharp linear low in amplitude between two large peaks. The axis of symmetry between the peaks always was oriented parallel to the crack and was always very close to the actual crack location. Two more examples of dry-crack reconstructions are shown in fig. 4.9 and 4.10 for depths just above the crack and in the top third of the crack, respectively. The orientation of the crack is quite evident in both reconstructions. As a final exercise in wavefront reconstruction, we reconstructed the dry-crack wavefront just above the source transducer. In doing so we violated one of the assumptions which went into the derivation of the wavefront reconstruction technique; namely, that the wave propagated through a source-free region. Even so, the technique resulted in a well-concentrated amplitude peak, corresponding quite well with the size and location of the source transducer. In fig. 4.11 and 4.12 we show the amplitude distribution of the unperturbed wavefront and the dry-crack wavefront just above the source.

We knew the orientation of the crack beforehand, so we were able to say that the reconstructions showed the presence of the crack, but it would be advantageous to be able to show a physical reason for the distinctive structure seen in the dry-crack reconstructions. We find such a reason by going back to the source model formulation in Chapter 2. We postulated that the observed wave-field could modeled by the superposition of the incident wave and the wave-field produced by the opening of a tensile crack. We

then calculated the far-field P-wave field due to an equivalent source based on the opening of a tensile crack. The radiation pattern of P-waves produced by this source model is shown in fig. 4.13. As we can see the two lobes of the radiation pattern bear a strong resemblance to the reconstructed amplitude distributions. This allows us to define the orientation of the crack with very little ambiguity. For information on the size of the crack, we will turn to data from the third experiment as analysed in terms of our source model.

## 4.2. RESULTS FROM SOURCE MODEL

### 4.2.1. FINAL FORMULATION OF SOURCE MODEL

Using the data set collected in the first and third experiments, it is now possible to finish the formulation of the source model. We have seen, in Chapter 2, that the time dependence of the displacement of the crack face should be the same as in the incident plane P-wave. This knowledge will allow us to define the spatial dependence and temporal dependence of the source function in terms of the incident wave. We can define the spatial dependence because of one implication of considering the incident wave to be a plane-wave when it encounters the crack, which is that the dislocation function will have the same shape across the source width at any distance $\vec{\xi}_1$ along the source length (L). So, if we write the source time function in the form:

$$\Delta U(\vec{\xi},t) = D\ (t - \frac{\vec{\xi}_1}{v}) \qquad \text{EQ 3}$$

where v is the velocity with which the displacement discontinuity (

or slip function) propagates. We can remove the $\xi_2$ dependence,

$$\int_{\Sigma} \dot{\Delta U}(\xi, t - \frac{r}{\alpha})\, d\Sigma_{\xi}$$

$$= W \int_{0}^{L} \dot{D}\,(T - \frac{r}{\alpha} - \frac{\xi_1}{v})\, d\xi_1$$

EQ 4

Where $\alpha$ is the compressional wave velocity, and L and W are the length and width of the source, respectively.

The integral can be further simplified by making the following approximation for the (r) dependence. We take $\xi$ to be the vector from the origin taken at a fixed point on the source surface ( $\Sigma$ ) to a point on $\Sigma$, $\hat{r}$ to be the vector from this point to the observation point, and $\hat{R}$ is the vector from the origin to the observation point, where the unit vector in this direction is denoted as $\hat{n}$ (Such that $\hat{R} = \hat{n} \cdot R$ . ). We can write :

$$r^2 = R^2 + \xi^2 - 2\xi \cdot \hat{R} = R^2\left( 1 + \frac{\xi^2}{R^2} - \frac{2\xi \cdot \hat{R}}{R^2}\right)$$

EQ 5

taking the square root gives;

$$r = R\sqrt{\,1 + \frac{\xi^2}{R^2} - \frac{2\xi \cdot \hat{n}}{R}\,}$$

EQ 6

We can expand the square root,

$$r = R\left|1 + \frac{1}{2}\left(\frac{\xi^2}{R^2} - \frac{2\xi \cdot \hat{n}}{R}\right) - \frac{1}{8}\left(\frac{\xi^2}{R^2} - \frac{2\xi \cdot \hat{n}}{R}\right)^2 + \frac{1}{16}(\ldots)^3 \ldots\right|$$

EQ 7

If we neglect terms:

$$R\,\frac{1}{2}\,\frac{\xi^2}{R^2} - R\,\frac{1}{8}\,4\frac{(\xi \cdot \hat{n})^2}{R^2} = \frac{1}{2}\left(\frac{\xi^2}{R} - \frac{8\xi \cdot \hat{n})^2}{R}\right)$$

EQ 8

and terms of higher order, we are left with,

$$r = R - \xi_1 \cdot \hat{n}$$

EQ 9

This is the Fraunhofer far-field approximation. We are justified in making this approximation when $\frac{\lambda}{4}$ is much greater than the neglected terms in eq. 5. In the case of our model, this criterion is met when the travel path from the scattering portion of the crack to the observation point is more than about 4 cm.

We can now rewrite eq. 3, using $r = R - \xi_1 \cos\phi$,

$$\int_{\Sigma} \dot{\Delta U}(\xi, t - \frac{r}{\alpha}) d\Sigma_{\xi} = W \int_0^L \dot{D}(\xi_1, t - \frac{R - \xi_1 \cos\phi}{\alpha}) d\xi_1$$

EQ 10

If we denote the Fourier transform of the slip velocity $\dot{D}(t)$ by $\dot{U}(\omega)$, where this transform is given by:

$$\dot{U}(\omega) = \int_{-\infty}^{\infty} \dot{D}(t) e^{-i\omega t} dt$$

EQ 11

The Fourier transform of eq. 10 is,

$$\Omega(\hat{x},\omega) = W \int_0^L \dot{U}(\omega)\, e^{-i\omega\xi_1 (\frac{1}{v} - \frac{\cos\phi}{\alpha})} d\xi_1$$

$$= WL\dot{U}(\omega) \frac{\sin X}{X} e^{-iX}$$

EQ 12

where $X = \frac{\omega L}{2} (\frac{1}{v} - \frac{\cos\phi}{\alpha})$. If we combine this with eq. 2.5 we get the complete expression for the far-field amplitude spectral density,

$$\left|\Omega^P(\hat{x},\omega)\right| = \frac{WL}{4\pi\rho R\alpha^3} (\lambda + 2\mu\sin^2\theta\sin^2\phi)\, \dot{U}(\omega) \frac{\sin X}{X} e^{-iX}$$

EQ 13

We shall now use the relation between the slip U and the displacement of incident P waves $W_{z_o}$ obtained earlier on the basis of a

quasi-static argument. From Eq. 2.14, we have

$$U = C \sqrt{\frac{a}{l_p} \frac{\sigma(1-\sigma)}{1-2\sigma}} W_{z_o}$$

EQ 14

where C is an unknown constant to be determined by the results of our model experiments. In the frequency domain, Eq. 14 can be transformed into a relation between the Fourier transform $\dot{U}(\omega)$ of slip velocity and that of incident wave displacement.

$$\dot{U} = i\omega C \sqrt{\frac{a}{l_p} \frac{\sigma(1-\sigma)}{1-2\sigma}} W_{z_o}(\omega)$$

EQ 15

Putting the above equation in Eq. 13, we can write the Fourier transform of the scattered wave displacements $U^P(\hat{x},\omega)$ in terms of that of the primary wave displacement $W_{z_o}(\omega)$.

Because of the geometry of our experiment it is possible to minimize effects due to the presence of the free surface and attenuation effects through a judicious choice of data points. Fig 4.14 shows the free surface effect on the horizontal and vertical displacements due to a unit incident plane P-wave. If the angle of incidence is in the range of 0 to 10 degrees, the amplification effect due to the free surface will be fairly constant, giving a variation of only 5 % over this range. This effect is made even smaller when we consider that, for data points within 5 cm. of the origin, the difference between angle of incidence of the incident and scattered waves is less than 5 degrees. This means that the free surface effect on the vertical displacement due to the incident wave and the scattered wave is virtually the same for data points near the origin. By restricting ourselves to this set of

data points we will gain two other advantages. First, since $\phi \sim 0$ and $v = \alpha$, x is nearly zero and $\frac{\sin X}{X}$ is unity. Secondly, the path length for the scattered wave will be nearly the same as the vertical distance from the incident wave front to the observation point. The implication of this is that the two signals will be attenuated nearly the same amount by anelastic attenuation.

For $\phi \sim 0$, then, Eq. 13 will be greatly simplified. We now rewrite Eq. 13 and 15 in terms of amplitude $A_{z_1}$ of primary waves observed at the surface. Since $A_{z_1}$ is about one half of $A_{z_o}$, we obtain from Eq. 13 and 15 ( putting $\phi \sim 0$ ) the amplitude ratio of scattered wave to primary wave as

$$\left|\frac{U^P(\omega)}{W_{z_1}(\omega)}\right| = \frac{C\omega\lambda WL}{2\pi\rho R\alpha^3} \sqrt{\frac{a}{l_p}} \frac{\sigma(1-\sigma)}{1-2\sigma}$$

EQ 16

for $\lambda = \mu$,

$$\left|\frac{U^P(\omega)}{W_{z_1}(\omega)}\right| = 0.125 \frac{CWL}{Rl} \sqrt{\frac{a}{l_p}}$$

EQ 17

Following the argument of section 2.2.2, we shall assume that $L \sim \frac{l_p}{2}$ and $W \sim 2a$. Then, the above equation becomes

$$\left|\frac{U^P(\omega)}{W_{z_1}(\omega)}\right| = 0.125\, C \frac{2a\,\frac{l_p}{2}}{Rl} \sqrt{\frac{a}{l_p}}$$

$$= 0.125\, C\, \frac{a}{R} \sqrt{\frac{a}{l_p}}$$

EQ 18

Since a = 1.27 cm, R = 7.5 cm

$$l_p = \frac{2.4 \times 10^5}{500 \times 10^3} = 0.5\text{cm}$$

$$\frac{a}{r} = \frac{1.27}{7.5} = 0.17$$

$$\sqrt{\frac{a}{l_p}} = \sqrt{\frac{1.27}{0.5}} = 1.59$$

$$\left|\frac{U^P}{W_{z_1}}\right| = 0.033 \times C$$

From fig. 3.22, the observed ratio is about 0.24. Therefore, C = 7.3. Putting this value of C back into Eq. 14, we obtain

$$U = 7.3 \sqrt{\frac{a}{l_p}} \frac{\sigma(1-\sigma)}{1-2\sigma} W_{z_o}$$

$$= 7.3 \times 1.59 \times 0.375 \, W_{z_o}$$

$$\sim 3 \, W_{z_o}$$

The above result shows that the opening of the crack by P waves propagating along the crack is a little greater that the peak to peak displacement amplitude of the incident P waves for the crack of radius 1.27 cm and the incident wavelength of 0.5 cm.

### 4.2.2. DISCUSSION

While these results are strictly valid only for our experimental model, we have developed a number of techniques and a model which could be applied to other geometries and materials. From our results, we can outline a methodology to be employed in such studies. We can split our analyses into two categories, those which depend on the construction of differenced seismograms, and those which rely on single records. When only the first arrivals are

recorded, the wavefront reconstruction technique can be used to infer the approximate position and orientation of the crack. Further, if the ampltude of the first full cycle is available, we can use the construction of section 3.3.3 to estimate the depth of the crack. The data required for these two techniques is significantly less than that required for the source model study, but we can still gain highly useful information from them. Thus, if the position and orientation of the crack are the desired information, we can suggest the use of these techniques.

However, if the size of the crack is of importance, a source model study can be used. In the last section we derived for our specific model, a value of the coefficient C, which we could now use to derive the size of the crack from the ratio of the scattered signal to the incident signal. Since we would be simply re-deriving one of the the terms we used to calculate the factor C in the first place, this would be a circular exercise. We could, however, predict the ratio of the scattered signal to the incident signal for a different ratio of crack size to wavelength. Or, for a different crack size to wavelength ratio, we could calculate the size of the crack from the ratio of the signals. The important point is that a model can be derived which gives reasonable results, and which can be used for other experiments.

## FIGURE CAPTIONS FOR CHAPTER IV

4.1. These records were produced by the x-y plotter attached to the oscilliscope for a signal recorded at (0,0). In practice, the two pulses were aligned on the oscilliscope screen where the trace is somewhat thicker than this figure would indicate. Owing to the thickness of the trace our accuracy of time measurement was $\pm.02$ microsecond.

4.2. These amplitude spectra were calculated for the first 80 microseconds of the records from the locations indicated on the figure. Comparison with the actual records indicates that the energy at 500 kHz. corresponds to the first 10-15 microseconds of the time record. The spectrum calculated for (0,-3) shows noticeably higher amplitude for this peak, corresponding to the observed peak in the first arrival amplitude noted in the vicinity of $x \sim \pm 3$ cm..

4.3. A significant problem in 3-D wavefront reconstruction is how to display the results. An isometric representation allows easy visualisation, but it is difficult to convey quantatitive information in this way. This figure helps to visualise the nature of the data set recorded for the reconstruction experiment.

4.4. The unperturbed wavefield reconstructed just above the source transducer has converged to a small area only slightly larger than the dimensions of the transducer itself. This was the first test the wavefront reconsctruction technique needed to pass before being applied to the crack problem.

4.5. The Moire Effect, while a common phenomenon in optics, is not normally encountered in seismology. In our case it results from the superposition of a rectangular sampling grid on a highly symmetric radial phase pattern. While it degrades the quality of the distribution plots, it has no adverse effect on our amplitude plots.

4.6. We see here the spatial distribution of the amplitude of the reconstructed wavefront in the center of the block when the block contains a fluid-filled crack. In this and subsequent plots, the contours are in the units of the measured signal (millivolts produced by the transducer in response to a stress pulse), and range from 0 to the maximum amplitude in 5 unit increments. This amplitude distribution shows no symmetry or structure which could be attributed to the presence of the crack.

4.7. This figure shows the amplitude distribution for the reconstructed wavefront in the case where the crack is dry. This amplitude shows a significant drop along a line which coincides with the location of the crack.

4.8. The reconstructed wavefront at a depth just above the fluid-filled crack shows as little effect due to the presence of the crack as the reconstruction shown in fig. 4.6

4.9. This reconstruction is for a depth at the top edge of the dry crack. The major feature of a sharp drop in amplitude along a line corresponding to the crack location is present in this reconstruction as in the other dry-crack reconstructions.

4.10. Yet another reconstruction for the case where the crack is dry. In this case the reconstruction depth is in the top third of the crack.

4.11. For the purposes of comparison, we have contoured the reconstruction shown in fig. 4.4. Virtually all of the energy recorded at the surface has been propagated back to a small area, necessitating a much larger contour interval, but also indicating that reconstruction results are reasonable.

4.12. The data recorded for the dry crack also converges back to avery small area. The form is somewhat distorted since we have violated the assumption of a source-free propagation path by introducing the crack.

4.13. The radiation pattern for P-waves produced by the opening of a tensile crack bears a strong resemblance to the amplitude distribution of the reconstructed wavefronts in the vicinity of the dry crack.

4.14. The presence of a free-surface introduces amplification of the vertical displacement for near-normal angle of incidence. These curves show the vertical and horizontal displacements measured at the free surface as a function of angle of incidence for an incident plane P-wave of unit potential. The calculation of these curves is based on the formulation cited by Chouet, 1978.

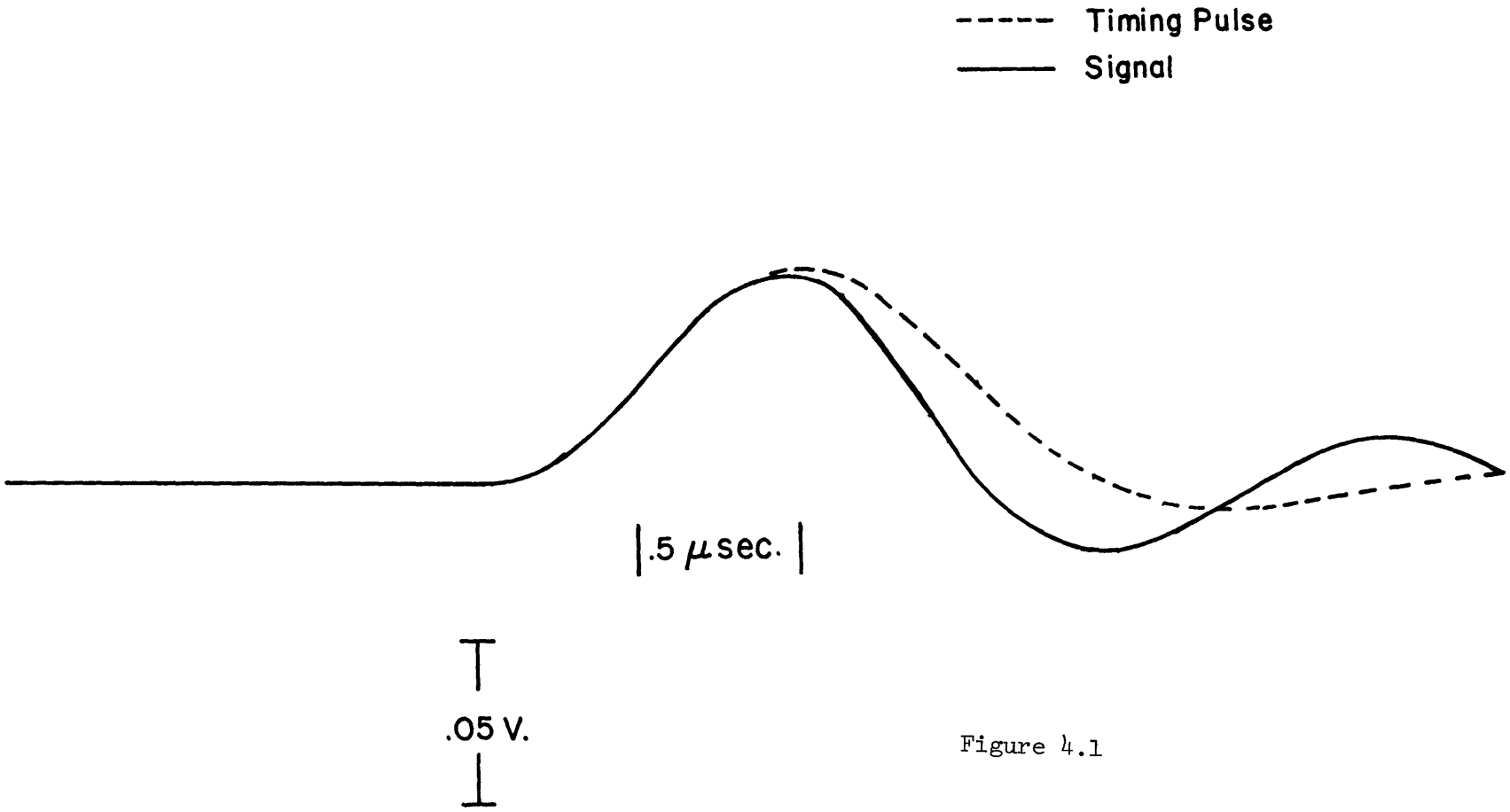


Figure 4.1

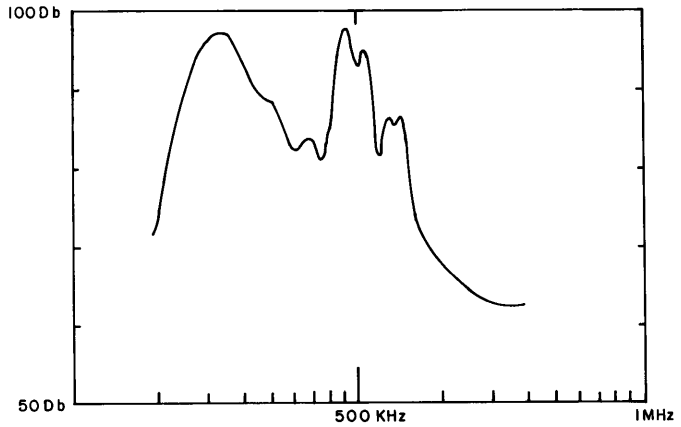


AMPLITUDE SPECTRUM AT (0,0)

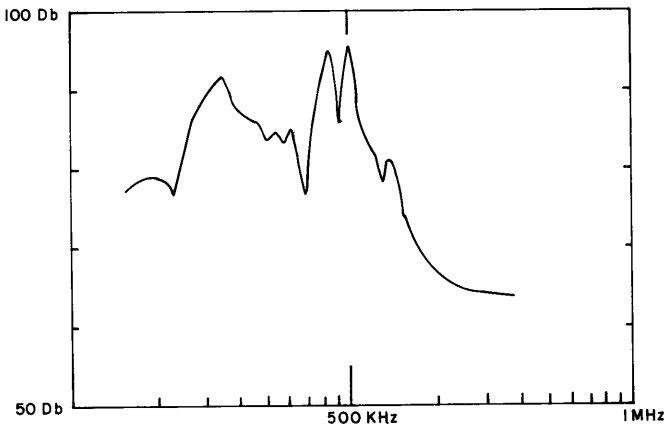


AMPLITUDE SPECTRUM AT (-5,0)

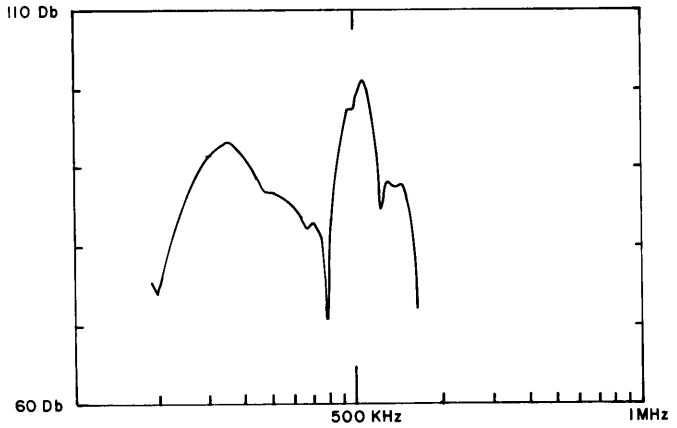


AMPLITUDE SPECTRUM AT (-3,0)

# DRY CRACK MODEL

Figure 4.2

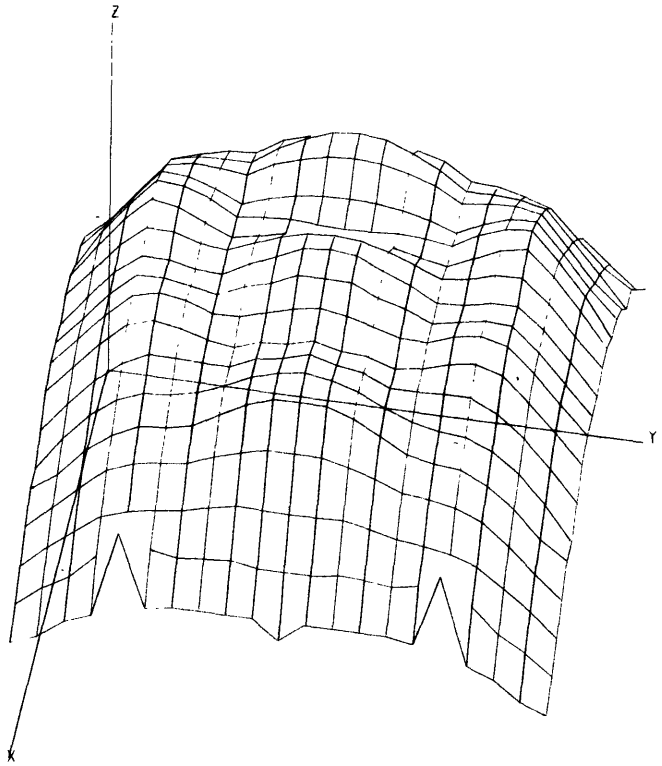


AMPLITUDE

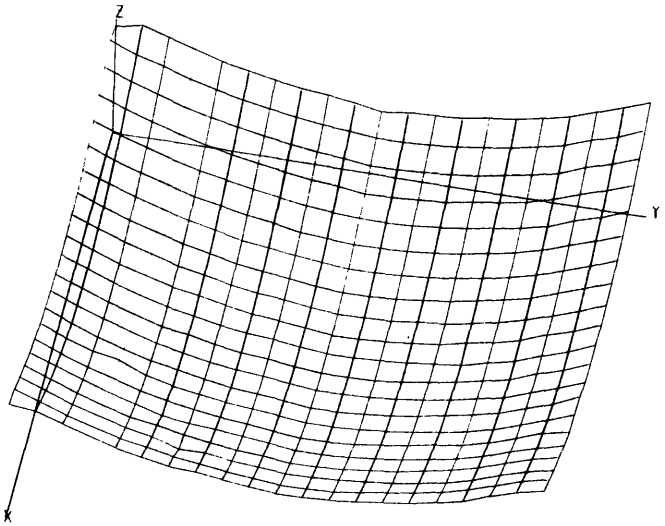


TRAVEL TIME

Figure 4.3

SURFACE DATA FOR WET CRACK

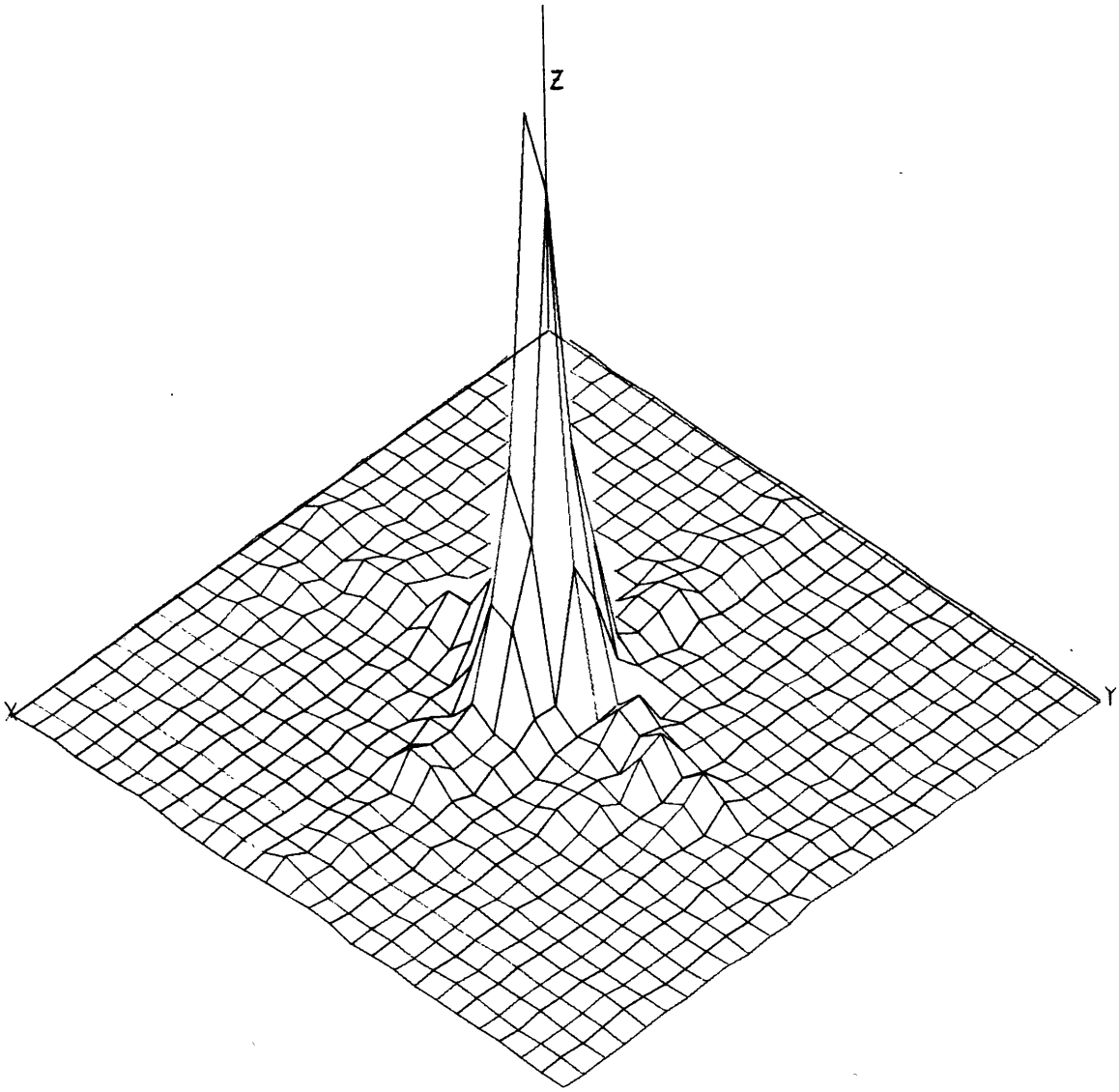


Figure 4.4

**Moiré Effect from rectangular sampling of radially symmetric phase**

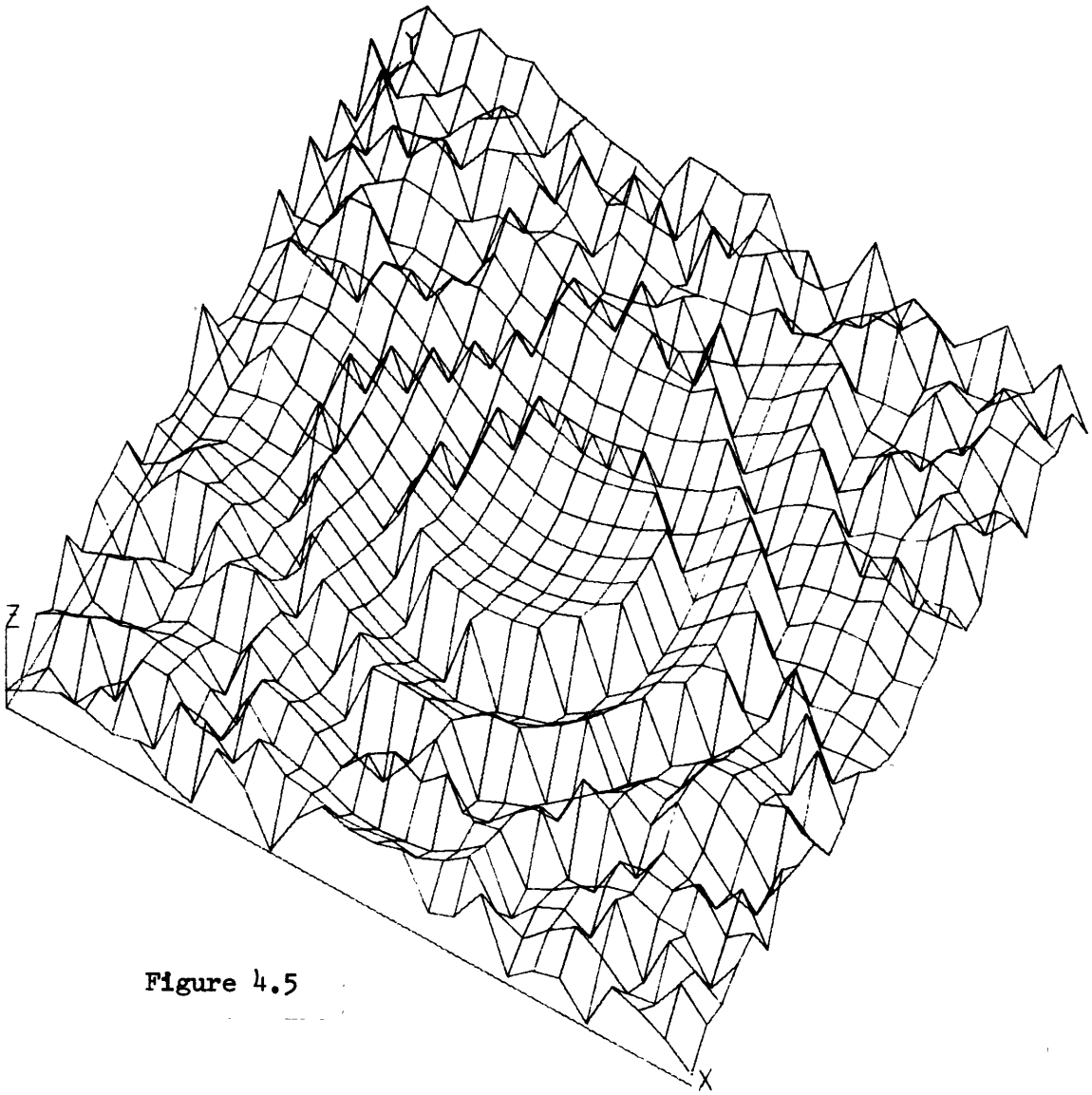


Figure 4.5

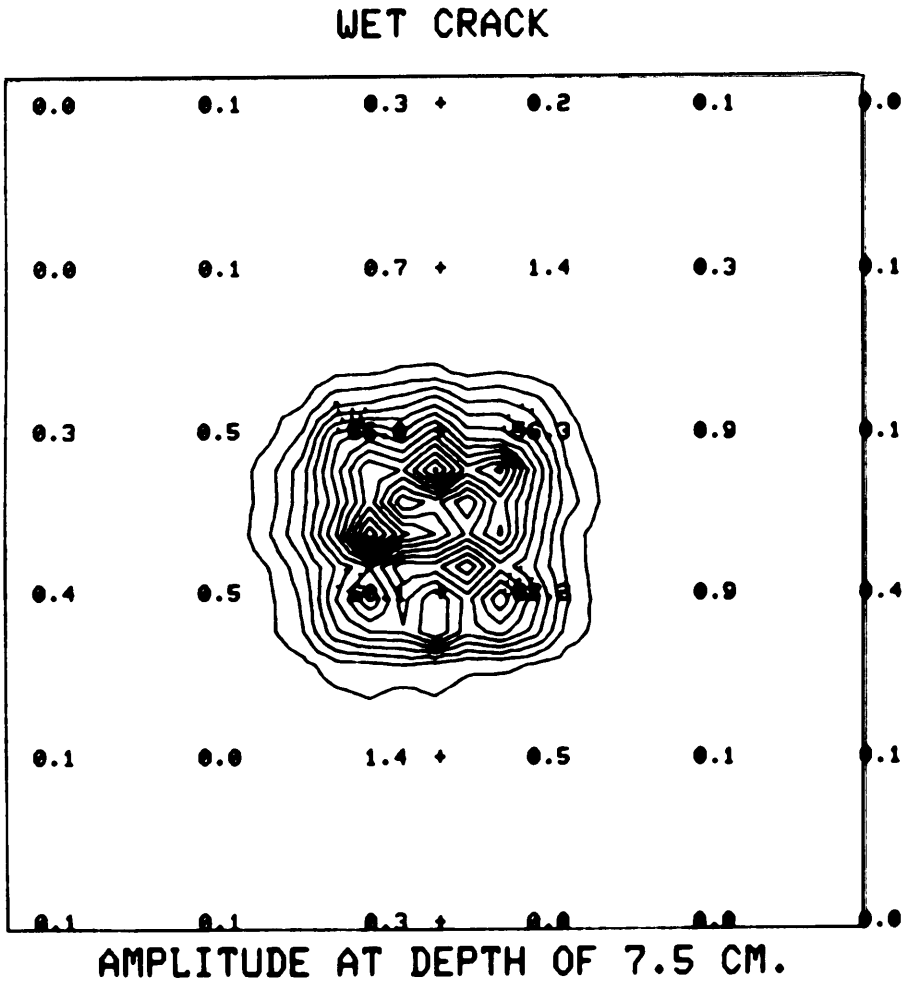
WET CRACK
0.0
0.1
0.3
0.2
0.1
0.0
0.1
0.7
1.4
0.3
0.1
0.3
0.5
0.9
0.1
0.4
0.5
0.9
0.4
0.1
0.0
1.4
0.5
0.1
0.1
AMPLITUDE AT DEPTH OF 7.5 CM.

Figure 4.6

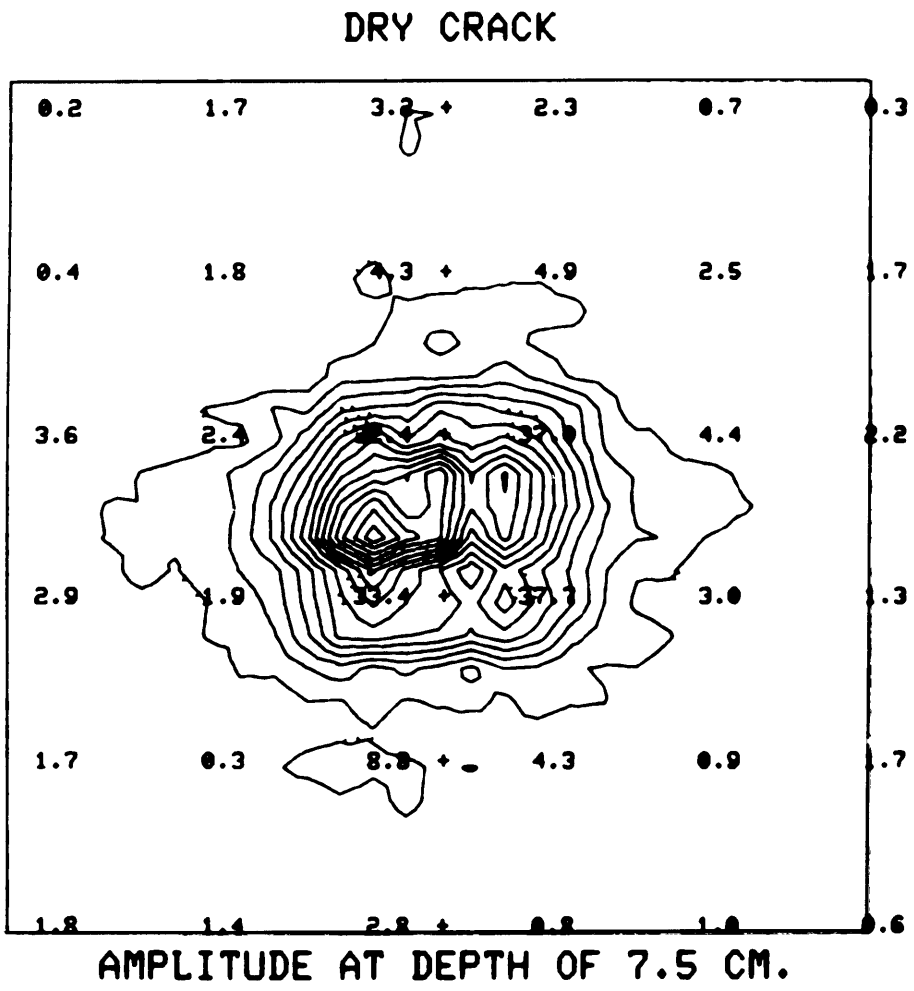
DRY CRACK
0.2
1.7
2.3
0.7
0.4
1.8
4.9
2.5
3.6
4.4
2.9
3.0
1.7
0.3
4.3
0.9
AMPLITUDE AT DEPTH OF 7.5 CM.

Figure 4.7

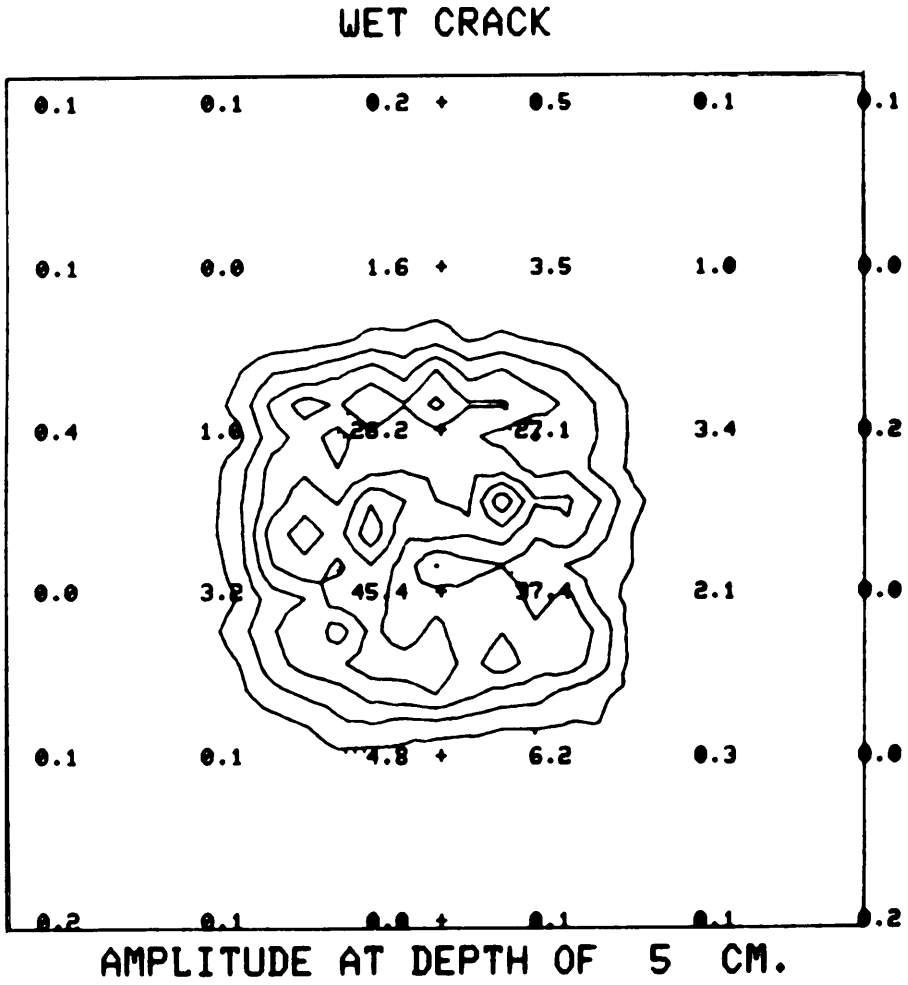
WET CRACK
0.1 0.1 0.2 0.5 0.1 0.1
0.1 0.0 1.6 3.5 1.0 0.0
0.4 1.0 28.2 27.1 3.4 0.2
0.0 3.2 45.4 37.4 2.1 0.0
0.1 0.1 4.8 6.2 0.3 0.0
0.2 0.1 0.0 0.1 0.1 0.2
AMPLITUDE AT DEPTH OF 5 CM.

Figure 4.8

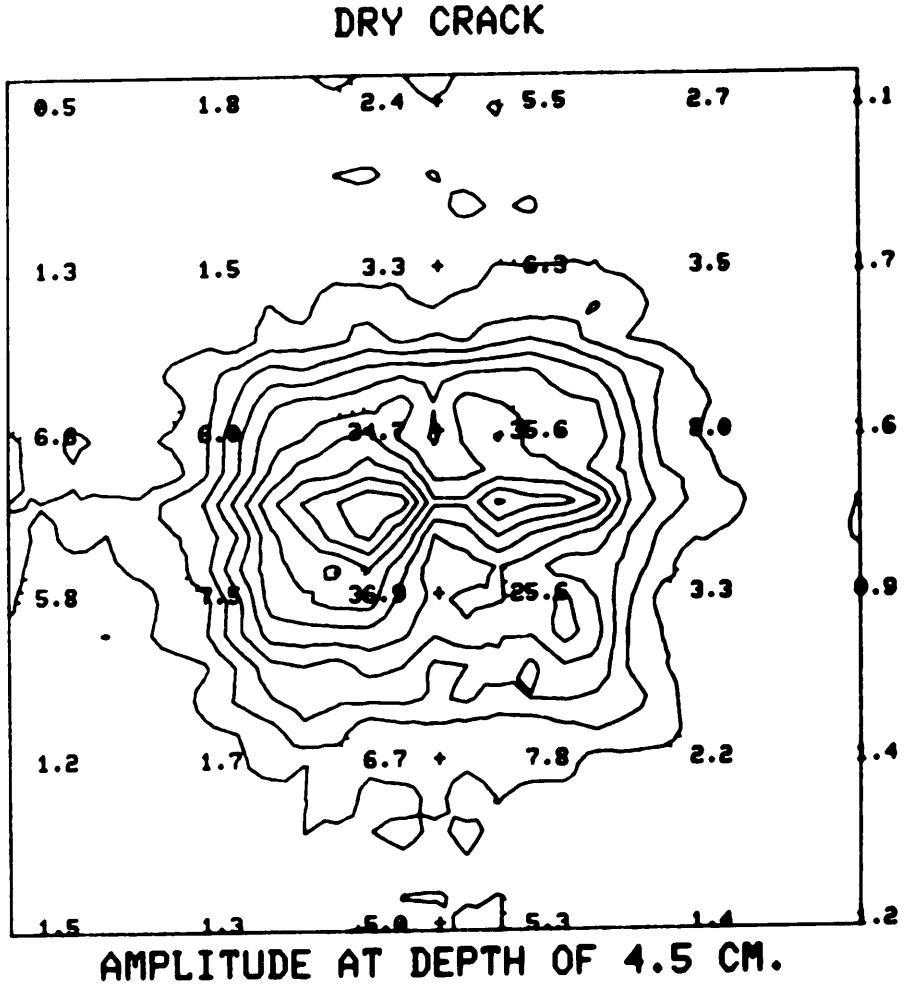
DRY CRACK
0.5
1.8
2.4
5.5
2.7
1.3
1.5
3.3
3.5
5.8
3.3
1.2
1.7
6.7
7.8
2.2
AMPLITUDE AT DEPTH OF 4.5 CM.

Figure 4.9

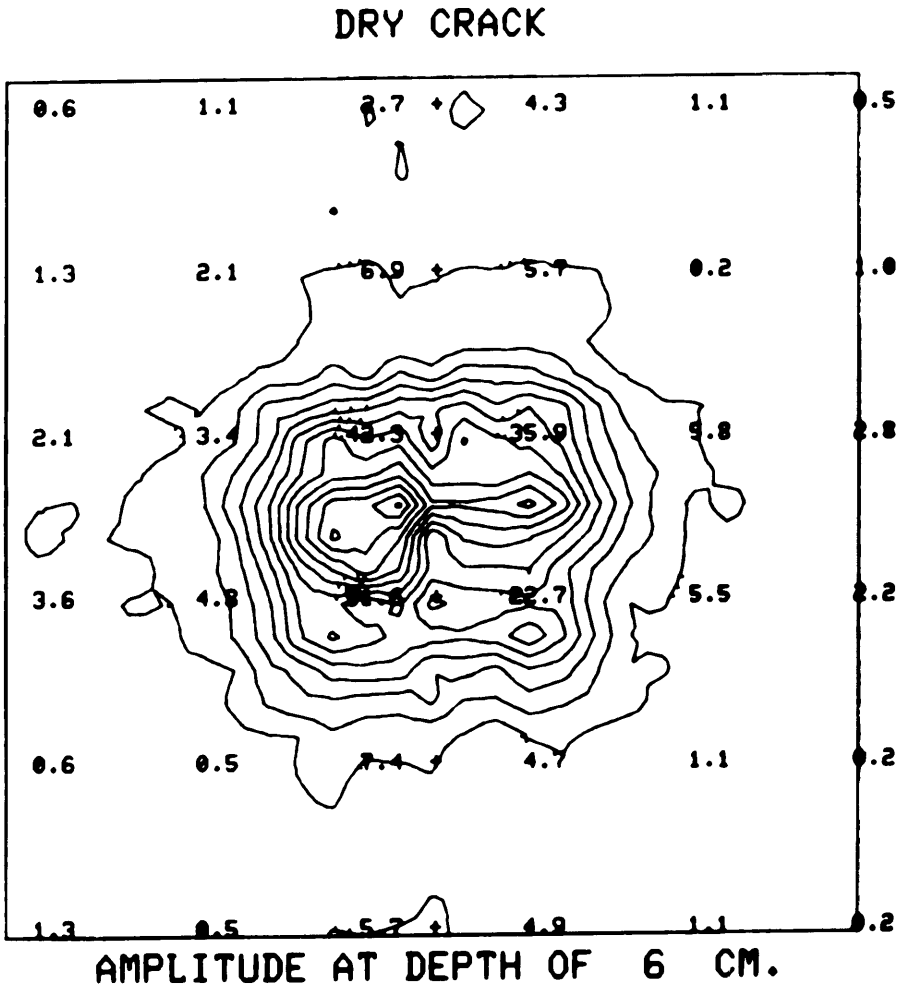
DRY CRACK
0.6
1.1
4.3
1.1
1.3
2.1
0.2
2.1
3.6
4.8
5.5
0.6
0.5
4.7
1.1
AMPLITUDE AT DEPTH OF 6 CM.

Figure 4.10

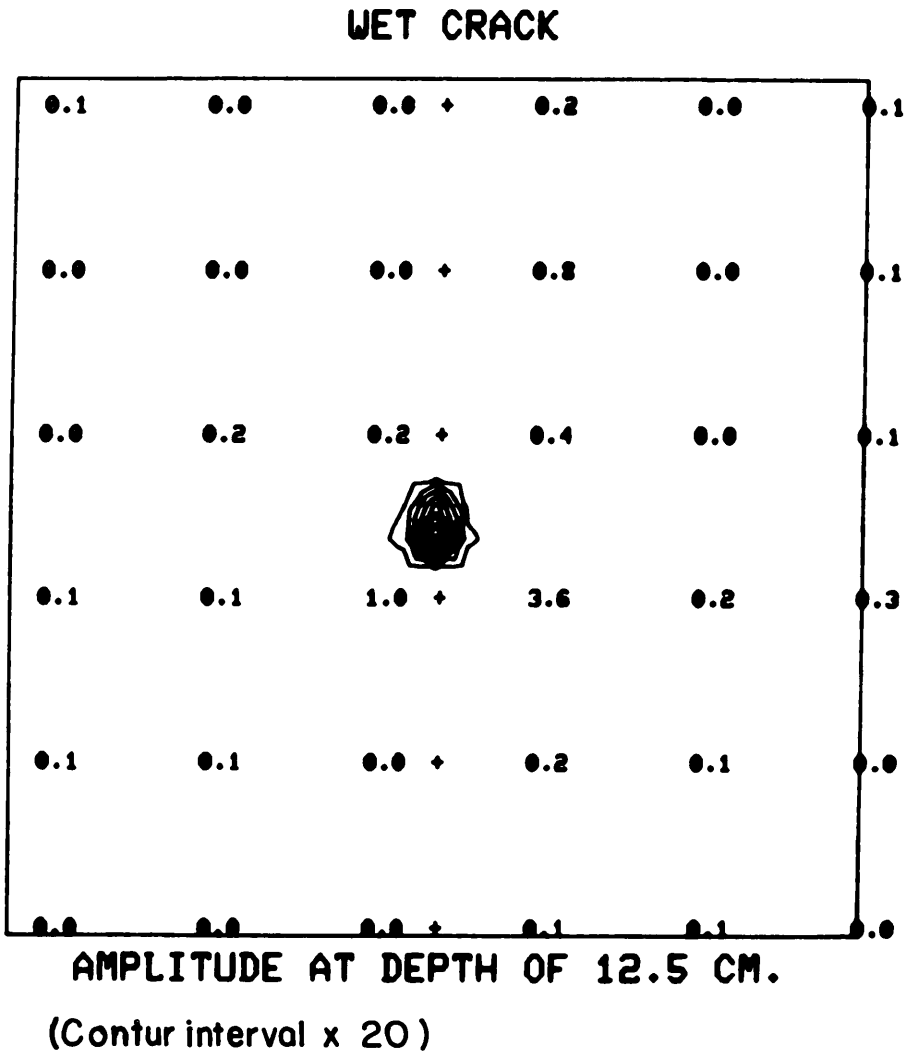
WET CRACK
0.1 0.0 0.0 0.2 0.0 0.1
0.0 0.0 0.0 0.8 0.0 0.1
0.0 0.2 0.2 0.4 0.0 0.1
0.1 0.1 1.0 3.6 0.2 0.3
0.1 0.1 0.0 0.2 0.1 0.0
0.0 0.0 0.0 0.1 0.1 0.0
AMPLITUDE AT DEPTH OF 12.5 CM.
(Contur interval x 20)

Figure 4.11

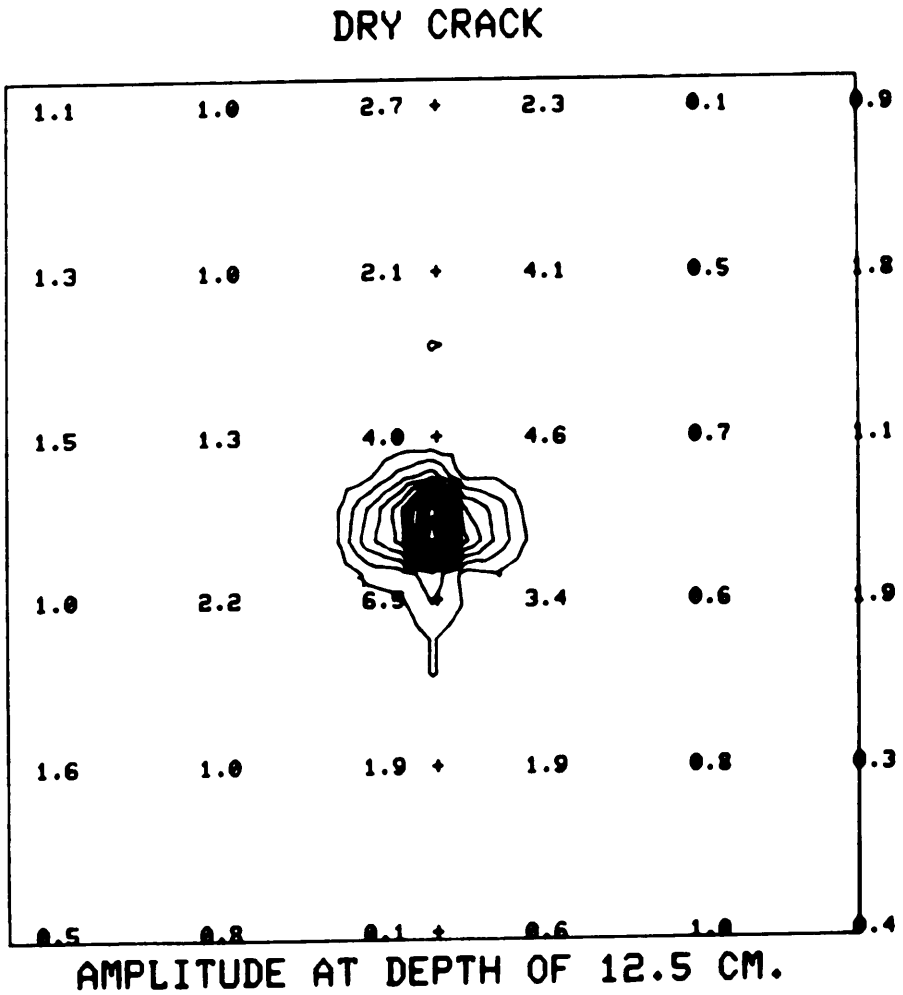
DRY CRACK
1.1
1.0
2.7
2.3
0.1
.9
1.3
1.0
2.1
4.1
0.5
.8
1.5
1.3
4.0
4.6
0.7
.1
1.0
2.2
6.5
3.4
0.6
.9
1.6
1.0
1.9
1.9
0.8
.3
0.5
0.8
0.1
0.6
1.0
.4
AMPLITUDE AT DEPTH OF 12.5 CM.

Figure 4.12

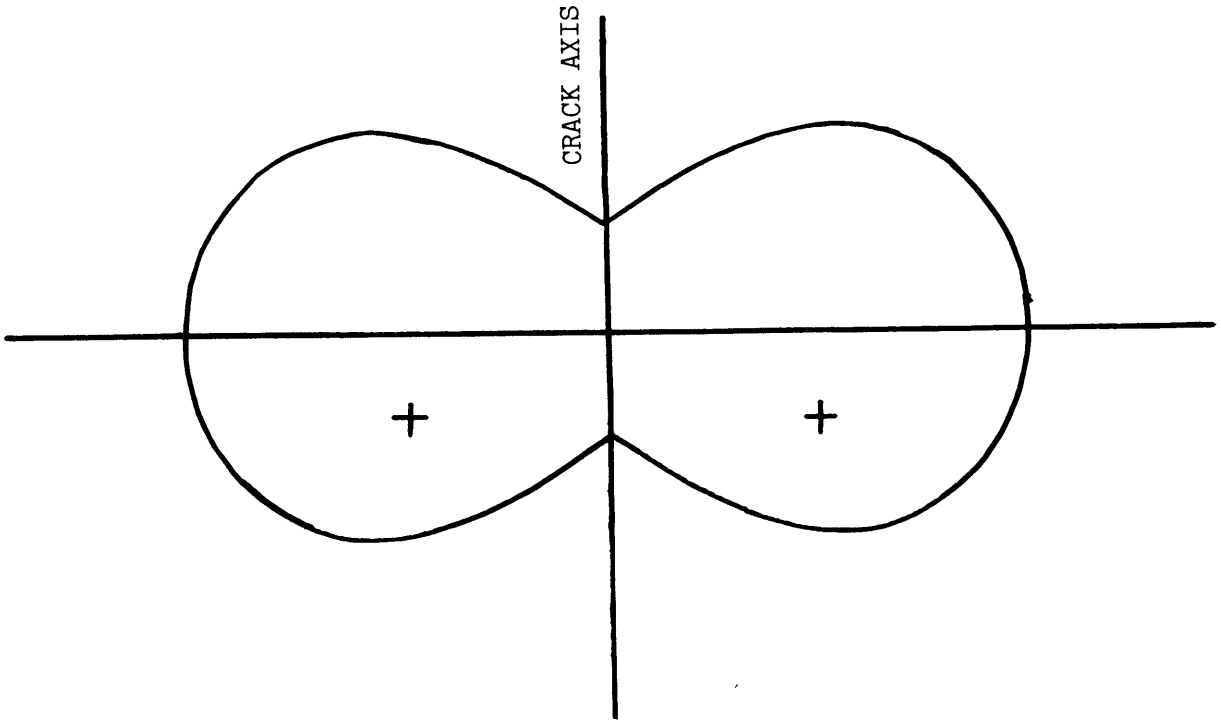


P-WAVE RADIATION PATTERN

FOR A TENSILE CRACK

Figure 4.13

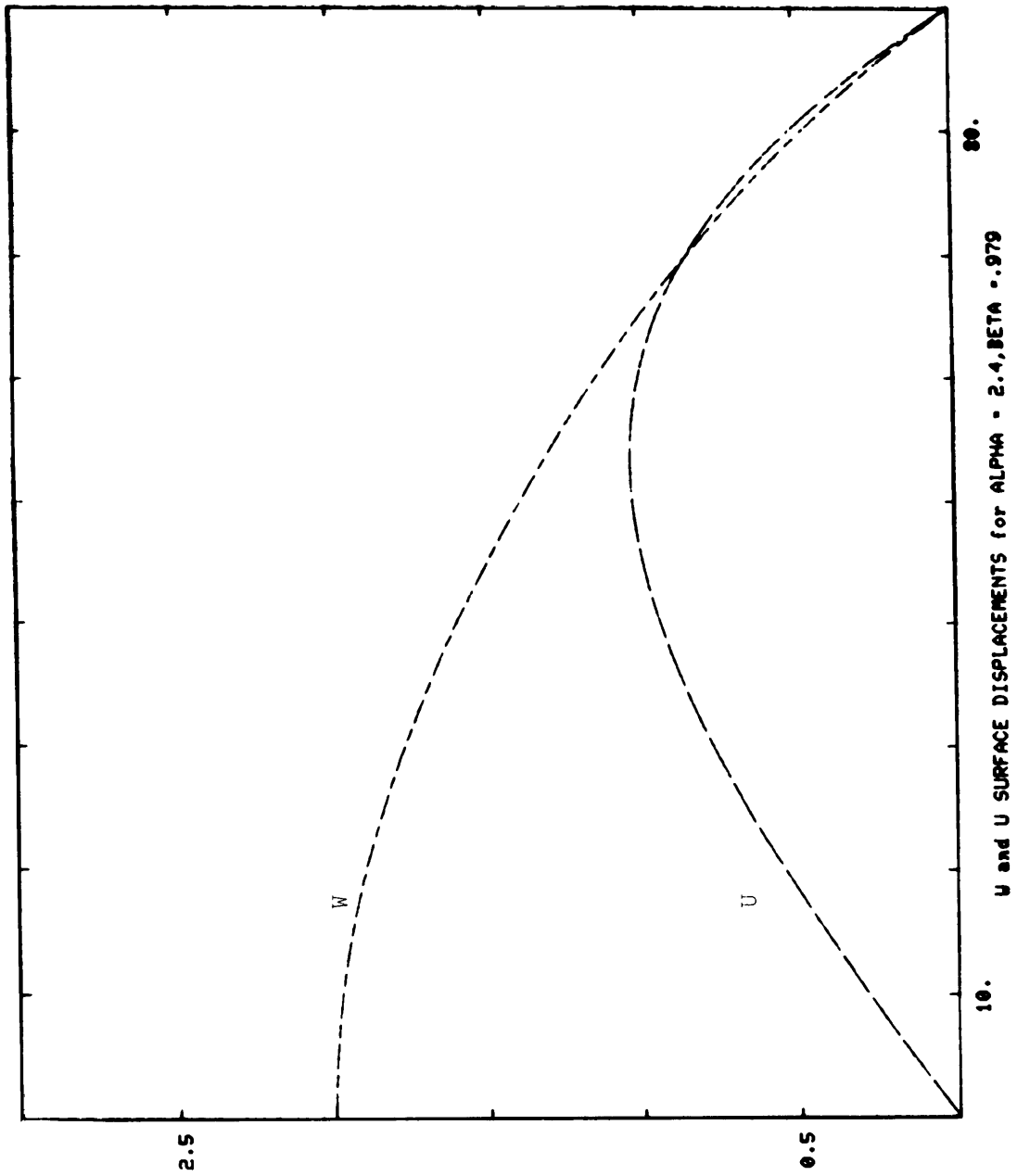
W and U SURFACE DISPLACEMENTS for ALPHA = 2.4, BETA = .979
W
U
2.5
0.5
10.
80.

Figure 4.14

# 5. CONCLUSIONS

In the beginning of this thesis we set out to examine three mildly disparate, but related problems. The main problem, of course, was to examine the feasibility of applying seismic methods to the study of scattering by a penny-shaped crack. The second problem was to see if the technique of wavefront reconstruction could provide information about earth structure that might not be obtainable with more traditional seismic methods. In evaluating these problems, we were faced with the need to determine if model seismology had once again become a viable research tool, which became our third problem. In discussing our findings we will attack these questions in reverse order.

As we outlined in Chapter 2, model seismology has been out of vogue in the United States for about the last decade. The success we had in using models to collect the data for our problem indicates that this disinterest should be re-examined. Perhaps the major complaint against model seismology in the 1960's was that it didn't supply data in a form compatible with field data. More precisely, digital data could not be easily obtained from model experiments. The use of an x-y scanner to record paper records moved model seismology into the early 70's; bypassing the paper copy to digitiser interface and digitising the records directly could move model seismology in the postion of being up to date with contemporary seismic data collection techniques. While we did not make use of them, commercial analog to digital converters are commonly available which can digitise at a rate of one microsecond per sam-

ple. Since the signals of interest in our experiment were 500 kHz., this sampling rate would have been adequate. So, the technolgy exist to remonve the most significant historical complaint against model seismology.

Even without using a fully digital system, we found that model studies provided us with data that would have likely been unobtainable in any other fashion. It is difficult to think of a field experiment or data set that could have been more useful in analysing this scattering problem than our model proved to be. We were able to collect data specifically tailored to each of our analysis techniques at a minimal cost. We also had the added advantage of flexibility that model studies provide. When we found that the difference between the waveforms produced by the wet and dry cracks was not easily resolved, we were able to quickly design and implement an alternative experiment which extracted the information we needed.

Against these advantages of model seismology we must weigh the difficulties we encountered in our work. Two major problems surfaced, the first of which was a lack of published information on the solution of problems specific to model seismology such as those we discussed in Chapter 2. Two fields which share a number of experimental techniques with model seismology are experimental rock mechanics and non-destructive acoustic testing of solids. While some useful information can be gleaned from the literature of these fields, model seismology has sufficient problems unique to itself that it could certainly benefit from its own literature on experi-

mental techniques.

The other problem we encountered was that our experiments were excessively time consuming. The need to manually position the probe for each data point and make a paper copy of the record or write down the arrival time and amplitude resulted in experiments that required days of constant attention. This limited the number of experiments we could undertake in a resonable amount of time. Fortunately, it is easy to envision an automated data collection system which would solve this problem handily. The mechanical stage and probe assembly we devised needs only the addition of a servo motor to each of the positioning micrometers and to the probe-lowering assembly to allow unattended operation under the control of a micro-processor. The addition of digital data collection and recording to such a system would remove the last obstacle to what we might term a renaissance of model seismology. The only pitfall would be the temptation to collect more data than could be easily processed. We can only conclude that model seismology deserves serious reconsideration as a research tool.

With regard to the wavefront reconstruction technique, our conclusions are somewhat less forceful. In using this technique we found an almost equal balance in assets and liabilities of the method. For example, while we were able to very precisely image the orientation and location of the crack on a given plane, we could not determine the size or depth of the crack with this technique. Further, while the data needed for reconstructions is only the amplitude and arrival time at each recording location ( as

opposed to requiring the entire waveform), the number of recording locations must be very great for reasonable reconstructions. In light of the conflicting attributes of this technique, we conclude that it is indeed useful, and is deserving of further study, if only to overcome some of the shortcomings.

Having dispensed with the ancillary problems raised by our experiments, we can now address ourselves to the primary problem. We have seen, for our particular model, how we can apply various seismic techniques to the study of scattering by a penny-shaped crack, depending on the form of data available. The wavefront reconstruction technique, as we have just noted, is tailored to the interpretation of travel time and amplitude measurements. From the results of our reconstructions we were able to verify a very important result. Namely, that the radiation pattern associated with the energy scattered from the dry crack is consistant with that due to the opening of a tensile crack. This observation does much ( in addition to the arguments cited in Chapter 2.) to enhance the believability of our scattering model.

One of the most interesting observations we can make using this same data set, is that the amplitude information is at least as important as the travel times. For the refraction experiments, we were unable to resolve any significant alteration in travel time due to the presence of the crack. Without the amplitude information, we would have been hard-pressed to estimate the depth of the source without resorting to a reflection shooting geometry.

Admittedly, our situation was highly idealised, and we were able to collect data for only one geometry, nonetheless, our results show how kinematic source modeling techniques might be applied to scattering by a penny-shaped crack under a variety of circumstances. The differential seismogram technique is particularly persuasive in support of this proposition. The fact that the waveform of the scattered signal is identical to the input waveform is telling evidence in support of modeling the incident wave as a forcing function of the crack face. The use of a simple ramp time function is, of course quite simplistic, but, as we have mentioned before, it is not a good idea to over-design one part of a model. Further experiments should naturally be run for a variety of crack size to wavelength ratios, and for a variety of source-receiver geometries. But, for the present, we have shown how one might use earthquake source modeling techniques to estimate the size of such a crack.

REFERENCES

Aamodt, R. L., 1977, Hydraulic fracture experiments in GT-1 and GT-2, Tech. Rpt. LA-6712, Los Alamos Sci. Lab., Los Alamos, NM.

Achenbach, J. D. and A. K. Gaufesen, 1977, Geometrical theory of diffraction for three-D elastodynamics, J. Acoust. Soc. Am., 61, 2, 413-421.

Agarwal, R. G., 1968, Ph.D. Thesis, University of Alberta, Edmonton.

Ang, D. D., 1958, Some radiation problems in elastodynamics, Dissertation, California Institute of Technology, Pasadena, CA.

Ang, D. C., and L. Knopoff, 1964a, Diffraction of scalar elastic waves by a clamped finite strip, Proc. Natl. Acad. Sci., 51, 593-598.

Ang, D. D., and L. Knopoff, 1964b, Diffraction of scalar elastic waves by a finite crack, Proc. Natl. Acad. Sci., 51, 593-598.

Baker, B. R., 1962, Dynamic stresses created by a moving crack, J. Appl. Mech., 29, 3, 449.

Berlincourt, D. A., D. R. Curran, and H. Jaffe, 1964, Piezoelectric and Piezomagnetic materials and their function in transducers, in Physical Acoustics, vol. 1, part A., ed. W. P. Mason, Academic Press, New York, 169-270.

Boyer, A. E., 1971, Formation of images using 5 mHz ultrasound and a computer, Ph.D. Thesis, Rice University, Houston, TX.

Bracewell, R., 1965, The Fourier Transform and its Applications, McGraw-Hill, New York.

Bullen, K. E., 1965, An Introduction to the Theory of Seismology, Cambridge University Press, Cambridge, UK.

Burridge, R., 1969, The numerical solution of certain integral equations with non-integrable kernals arising in the theory of crack propagation and elastic wave propagation, Geophys. J. R. Astr. Soc., 265, A, 1163, 353-381.

Chen, E. P., and G. C. Sih, 1977a, Transient response of cracks to impact loads, in Mechanics of Fracture, vol. 4, ed. G. C. Sih, Noordhof International Publishing, Leyden, Netherlands.

Chen, E. P., and G. C. Sih, 1977b, Scattering waves about stationary and moving cracks, in Mechanics of Fracture, vol. 4, ed. G. C. Sih, Noordhof International Publishing, Leyden, Netherlands.

Chouet, B., 1978, Statistical synthesis of source-mechanism of seismic events in the cooling lava lake on Kilauea Iki, Hawaii, submitted to J. Geophys. Res..

Das, S. and K. Aki, 1977, Fault plane with barriers; a versatile earthquake model, J. Geophys. Res., 82, 36, 5658-5670.

El Sum, H. M. A., 1968, Acoustical Holography, vol. 1, 1-26, Plenum Press, New York.

Fehler, M. and K. Aki, 1978, Numerical study of diffraction of plane elastic waves by a finite crack with application to location of a magma lens, Bull. Seism. Soc. Amer., 68, 3, 573-578.

Fitzpatrick, G. L., H. R. Nicholls, R. D. Munson, 1977, An experiment in seismic holography, Bureau of Mines Report of Investigation/1972, No. 7607, United States Department of Interior.

Gladwin, M. T., and F. D. Stacey, 1974, Anelastic degradation of acoustic pulses in rock, Phys. Earth Planet. Int., 8, 332-336.

Goodman, J. W. and A. M. Silvestri, 1971, Some effects of Fourier-domain phase quantization, IBM J. Res. and Dev., 14, 478-484.

Haskell, N. A., 1964, Total energy and energy spectral density of elastic wave radiation from propagating faults, Bull. Seism. Soc. Amer., 54, 1811-1841.

Haskell, N. A., 1966, Part II, A statistical source model, Bull. Seism. Soc. Amer., 56, 125-140.

Haskell, N. A., 1969, Elastic displacements in the near-field of a propagating fault, Bull. Seism. Soc. Amer., 59, 865-908.

Haskell, N. A., and K. C. Thomson, 1972, Elastodynamic near-field of a propagating tensile fault, Bull. Seism. Soc. Amer., 62, 675-697.

Hilterman, F. J., 1970, Three-dimensional seismic modeling, Geophysics, 35, 6, 1020-1037.

Hilterman, F. J., 1975, Amplitudes of seismic waves, a quick look, Geophysics, 40, 5, 745-762.

Jain, D. L. and R. P. Kanwal, 1972, Diffraction of elastic waves by two coplanar Griffith cracks in an infinite plastic medium, Int. J. Solids Structures, 8, 961-975.

Kaufman, S. and W. L. Roever, 1951, Laboratory studies of transient elastic waves, Proc. 3rd World Petrol. Cong., Sect. 1, 537-545, Brill, Leiden.

Kjartansson, E., 1978, Constant-Q wave propagation and attenuation, submitted to J. Geophys. Res.

Lalor, E., 1968a, Inverse wave propagator, J. Math. Phys., 9, 2001-2006.

Lalor, E., 1968b, Conditions for the validity of the angular spectrum of plane waves, J. Optical Soc. Amer., 58, 1235-1237.

Lancaster, D., 1977, The TTL Cookbook, Howard W. Sams Inc., Indianapolis, Ind., pp. 89-90, 180-182.

Larson, D. E. and F. J. Hilterman, 1976, Diffractions: Their generation and interpretation use, Paper presented at 29th Annual Midwestern Exploration Meeting, S.E.G., March 7-9, 1976, Dallas, TX.

Lavergne, M. and J. Chauveau, 1961, Fonctions de Transfert D'emetteurs de Capteurs Piezoelectriques Pour Modelles Sismiques, Acustica, 11, 121-126.

Madariaga, R., 1976, Dynamics of an expanding circular fault, Bull. Seismol. Soc. Amer., 66, 639-666.

Mason, W. P., 1948, Electromechanical Transducers and Wave Filters, 2nd Edition, Van Nostrand, New York.

Maue, A. W., 1954, Die Enstpannungswelle bei plotzlichen Einschnitt eines gespannten elastichen korpers, Z. Angew. Math. Mech., 34, 112.

Mersereau, R. M., 1975, Two-dimensional digital filtering, Proc. IEEE, 63, 4, 610-623.

O'Brien, P. N. S., and M. P. Symes, 1975, Model seismology, Rept. Prog. Phys., 34, 697-764.

Oster, G., 1967, Holography as a Moire phenomenon, Proc. of the Symposium on Modern Optics, Polytechnic Press, Brooklyn, NY.

Redwood, M., 1961, Transient performance of a Piezoelectric trasducer, J. Acoust. Soc. Am., 33, 527-536.

Redwood, M., 1962, Determination of the parameters of a Piezoelectric transducer from the decay of resonant vibrations, J. Acoust. Soc. Am., 34, 895-902.

Redwood, M., 1964, Experiments with the electrical analog of a Piezo-electric transducer, J. Acoust. Soc. Am., 36, 1872-1880.

Rieber, F., 1936, Visual representation of elastic wave patterns under various structural conditions, Geophysics, 1, 196-218.

Rieber, T., 1937, Complex reflection patterns and their geologic sources, Geophysics, 3, 2, 132-160.

Riznichenko, Y. V., B. N. Ivakian, and V. R. Bugrov, 1951, Izv. Akad. Nauk. S.S.S.R. Ser. Geofiz., 1-30.

Schmidt, O., 1939, Uber Kopfwellen in der Seismik, Z. Geophys. 15, 141-148.

Schwab, F. and R. Burridge, 1968, The interface problem in model seismology (welded contact), Geophysics, 33, 3, 473-480.

Sherman, G. C., 1967, Integral transform formulation of diffraction theory, J. Optical Soc. Amer., 57, 1490-1498.

Sherman, G. C., 1968, Diffracted wavefields expressible by plane wave expansions containing only homogeneous waves, Phys. Rev. Lett., 21, 761-764.

Sherman, G. C., 1969, Diffracted wave fields expressible by plane-wave Expansions containing only homogeneous waves, J. Optical Soc. Amer., 59, 697-711.

Shewell, J. R. and E. Wolf, 19, Inverse diffraction and a new reciprocity theorem, J. Optical Soc. Amer., 58, 12, 1596-1603.

Sih, G. C., 1968, Some elastodynamic problems of cracks, Int. J. Fracture Mech., 4, 51.

Sih, G. C., I. F. Loeber, 1969, Normal compression and radial shear waves scattering at a penny-shaped crack in an elastic solid, J. Acoust. Soc. Am., 46, 3, 711-721.

Sneddon, I. N., 1944, The stress distribution due to a force in the interior of a semi-infinite elastic solid, Proc. Camb. Soc., 40, 229.

Sneddon, I. N., 1946, The stress distribution in the neighborhood of a crack in an elastic solid, Proc. Roy. Soc. A, 187, 229.

Sneddon, I. N., 1965, A note on the problem of the penny-shaped crack, Proc. Camb. Phil. Soc., 61, 609.

Sneddon, I. N. and M. Lowengrub, 1969, Crack Problems in the Classical Theory of Elasticity, John Wiley and Sons, New York.

Sneddon, I. N. and R. P. Srivastav, 1965, The stress in the vicinity of an infinite row of colliner cracks in an elastic body, Proc. Roy. Soc. Edinburg A, 67, 1, 39-49.

Sommerfeld, A., 1954, Optics, Academic Press, New York.

Terada, T., and Ch. Tsuboi, 1927, Experimental studies on elastic waves, Bull. Earthq. Res. Inst., Tokyo Univ., 3, 55-65.

Thau, S. A., and T. H. Lu, 1970, Diffraction of transient horizontal shear waves by a finite crack and a rigid ribbon, Int. J. Engng. Sci., 8, 857-874.

Thau, S. A. and T. H. Lu, 1971, Transient stress intensity factors for a finite crack in an elastic solid caused by a dilatational wave, Intl. J. of Solids and Struct., 7, 731-750.

Thomson, K. C., and R. Doherty, A correction to "Elastodynamic near-field of a finite propagating tensile fault" by Haskell and Thomson, Bull. Seism. Soc. Amer., 67, 1215-1217.

Toksoz, M. N. and F. Schwab, 1964, Bonding of layers in two-dimensional seismic modeling, Geophysics, 24, 3, 405-413.

Van Rooy, D. L., 1971, Digital ultrasonic wavefront reconstruction in the near field, Ph.D. Thesis, Rice University, Houston, TX.

Vinogradov, S. D., A. V. Nikolaev, P. A. Troitskii, and J. F. Scheimer, 1976, Investigation of the possibility of applying seismic holography to large seismic arrays, in Report on Joint Soviet-American Work on Earthquake Prediction, vol. 1, no. 2.

White, J. E., 1965, Seismic Waves, Radiation Transmission and Attenuation, McGraw-Hill Book Company, New York, NY.

Wolf, E., and J. R. Shewell, 1967, The inverse wave propagator, Phys. Letts., 25A, 417-418.

Zoback, M. D., J. H. Healy, and J. C. Roller, 1977, Preliminary stress measurements in central California using the hydraulic fracturing technique, Pure Appl. Geophys., 115, 135-152.

# APPENDIX

In order to provide complete information about the physical properties of the epoxy used in our model, we conducted a number of tests after completing the experimental work. Three small samples were cut from the model block: a cube .5 inches on a side, a rod 6 inches long by .25 inches in diameter, and a cylinder 2.5 inches long by .5 inch in diameter. The dimensions of the samples were measured with a machinist's micrometer and then each sample was weighed on a laboratory balance. The average density derived from these measurements was 1.22 $gm/cm.^{-3}$ $\pm .02$ $gm./cm.^{-3}$.

## Q - MEASUREMENT

The long rod was used to measure the quality factor "Q", of the material using the resonant bar method. {White,1970} When a bar is driven at one end at its lowest resonant frequencies, longitudinal waves propagate along its length at a velocity $C_y$ governed by the Young's modulus:

$$C_y = \sqrt{\frac{E}{\rho}} \qquad \text{EQ A.1}$$

If the attenuation of such waves is expressed in the form $e^{-a_y x}$, it can be shown {White,1970} that the Q of the material can be expressed in terms of the velocity and attenuation of the Young's modulus waves, to wit,

$$\frac{1}{Q} = \frac{a_y C_y}{f} = \frac{2\Delta f}{f_n}$$

EQ A.2

P tranducers were cemented to each end of the rod with Duco cement, and the rod was supported only at its center. One of the transducers was driven by a variable frequency source, and the resonance points of the combined rod/transducer system were measured. Results from this experiment are summarised in Table A.1. The corrected Q of 21 is constant over the range of frequencies used. The correction refers to the removal of effects due to the presence of the transducers on the end of the rod.

TABLE A.1

RESULTS FROM RESONANT BAR EXPERIMENT

| Mode(M) | $F_M$(kHz.) | +3Db. | -3Db. | $Q_M$ | $Q_{Corr.}$ |
|---|---|---|---|---|---|
| 1 | 10.438 | 10.647 | 10.229 | 25.0 | 20.6 |
| 2 | 22.586 | 23.038 | 22.135 | 25.0 | 20.6 |
| 3 | 35.054 | 35.754 | 34.353 | 25.0 | 20.6 |
| 4 | 47.560 | 48.510 | 46.610 | 25.0 | 20.6 |
| 5 | 60.080 | 61.281 | 58.880 | 25.0 | 20.6 |

Young's Modulus Velocity= 3.366 km/sec.

Another check of Q is provided by the constant Q model of Kjartansson (1978). Kjartansson's work is a theoretical derivation of of a constant defined in earlier experimental studies by Gladwin and Stacy (1974). If the rise time of an arrival is defined as the ratio of the maximum amplitude of the arrival to the maximum slope, Gladwin and Stacy found that $t$ could be expressed by:

$$t = t_o + C\frac{T}{Q} \qquad \text{EQ A.3}$$

Where:

$t_o$ is the rise time of the source,

T is the total travel time of the arrival,

and, C is the experimentally determined constant.

Kjartansson's theoretically derived values for C agree well with published experimental measurements. For Q > 20 Kjartanssons gives C= .485 for displacement records, and .298 for velocity records. Applying this latter value to wet records in a region $\pm$2.54 cm. from the origin gives Q = 26 $\pm$ 2, which is certainly in the same neighborhood as the measurements from resonant bar method.

COMPRESSIBILITY MEASUREMENT

The final sample (.5 inch by 2.5 inch cylinder) was used to measure the compressibility of the material. Besides the intrinsic value in making such a measurement to help complete our description of the model material, we can use it to determine which of the two possible S-wave velocities mentioned in Chapter 2 is more nearly correct. Two BLH SR-4.FAE-50-12-56 strain gauges were glued to the sample which was then placed in a pressure vessel capable of producing over 2 kBars of hydrostatic compression. Plotting the linear strain as a function of applied pressure results in a very nearly straight line. The beginning of the curve shows a very slight tendency to taper-off, indicating stiffening, however, in a very short time, the curve becomes virtually straight.

The compressibility and bulk modulus calculated from the slope of this line are:

$k = .057$ Mbar

$\beta = 17.55 \ \text{Mbar}^{-1}$

We can express the compressibility in terms of the P-wave velocity ( $V_P$ ), the S-wave velocity ( $V_S$ ), and the density ( $\rho$), as;

$$\frac{V_P^2 \rho}{100} - \frac{4}{3}\left(\frac{V_S^2 \rho}{100}\right) = k \qquad \text{EQ A.4}$$

Using a P-wave velocity of 2.35 km/sec, and S-wave velocity of .97 km/sec, we get k=.055 Mbar. If we use the higher value for the S-velocity of 1.1 km/sec, we get k=.045 Mbar. So, we can say that the slower S-wave velocity is consistant with the measured compressibility.

COMPARABLE MATERIALS

For those who might wish to reproduce experiments such as these, a number of materials are available in the United States with similar properties. An epoxy with very similar characteristics one might investigate is Hy-Sol Epoxi-Patch. A polyester casting resin which has similar properites is Crystal Clear Casting Resin, made by the Fibre-Glass Evercoat Company, which has the added advantage of being water-clear, allowing easy visual inspection of embedded inhomogeneities. As a guide to the type of materials which enjoy the advantages of easy bonding at interfaces we summarise in Table A.2 physical properties of our material and published properties of Poly-Vinyl Chloride and Lucite.

TABLE A.2

COMPARISON OF MATERIAL PROPERTIES

| QUANTITY | LUCITE | PVC(rigid) | EPOXY |
|---|---|---|---|
| Density(gm/cc) | 1.2 | 0.9 | 1.2 |
| P-Velocity(km/sec) | 2.7 | 2.3 | 2.3 |
| S-Velocity(km/sec) | 1.2 | .975 | 1.0 |
| Poisson's Ratio | 0.33 | 0.37 | 0.37 |